Two and Three Dimensional Graphene Devices for Electronics, Sensing and Biotechnology

BY

Shideh Kabiri Ameri Abootorabi

A dissertation submitted in partial fulfillment

of the requirements for the degree of

Doctor of Philosophy

in

Electrical Engineering

at

TUFTS UNVERSITY

August 2015

ADVISER:

Professor Sameer R. Sonkusale

To my Father, Mother and my Family

ABSTRACT

Graphene is an atomically thin zero band gap semiconductor or semimetal, with a strong ambipolar electric field effect, remarkably high carrier mobility at room temperature, high carrier density and high saturation velocity. Due to extraordinary electrical properties of graphene, it has been suggested as a possible candidate for beyond-CMOS field effect transistor (FET) with applications mainly in RF and analog domain. Graphene is also mechanically strong and has good biocompatibility, is electrochemically stable, shows excellent broadband optical transparency and can be made very sensitive to the surrounding media, making it a promising candidate for sensing and bioelectronics applications. Although two dimensional graphene has shown remarkable electrical, physical and chemical properties, extending it in three dimensional form may enhance the functionality and performance of devices and enable new functions currently not possible. In this dissertation, the application of two and three dimensional graphene in electronics, sensing and bioelectronics is presented.

A transparent graphene based microfluidic chip for dielectrophoretic cell trapping and lysis with graphene as electrode is introduced and it is has been shown that graphene behaves as an electrochemically stable electrode in the presence of high DC electric field in biological medium. Using graphene minimizes the Faradic reaction which would otherwise harm living cells and change the chemical and physical properties of

electrolytes and electrodes.

Next for the first time a three dimensional graphene field effect transistor is introduced and studied. The channel of this transistor is made of three dimensional graphene foam, which is gated using ionic liquid and ionogel to realize both liquid and semisolid state versions. Liquid and gel at the interface with the graphene forms a double layer capacitance (EDLs) of extremely large capacitance per unit surface area which provides an all-around electrostatic control of the transistor channel and leads to a lower operating voltages. Due to higher surface area of the foam, the transistors show up to 26.72 times higher current capacity than the equivalent conventional two dimensional graphene transistors.

The network structure of the foam expanded in three dimensions leads to higher mechanical stability and results in mechanical fault-tolerance. Higher surface area of the foam and high mechanical strength of three dimensional graphene transistor make it interesting for sensing applications. In this dissertation, mechanical, chemical and biological sensors are realized based on a mono to double layer and few layers of the graphene foam. For chemical sensing, we demonstrate its application in pH sensing directly in biological fluids. For mechanical sensing, we present its application in sensing strain and for biological sensing, we show its ability to capture electrically activity from electrogenic cells.

The pH sensor consists of a thin layer of HfO_2 as a sensing surface was grown all-around of the three dimensional graphene foam serving as a transistor channel. The three dimensional graphene transistor shows higher pH sensitivity (79 mV/pH) than conventional two dimensional graphene based sensor even in high ionic strength medium

and in body fluids. We attribute the high sensitivity and ability of sensing pH at high ionic strength media to the three dimensional structure of the channel and existence of sensing surface all-around the graphene channel.

A strain sensor is based on few layers of the graphene foam. Due to the three dimensional network structure of the graphene foam, this sensor shows mechanical fault-tolerance and robustness, and also demonstrates high dynamic range compared to the two dimensional graphene based sensors.

Graphene foam based device is also used as a scaffold for growing different types of cells and recording electrical signal from electrogenic cells. It is shown that graphene shows good biocompatibility and it can be used as an ideal electrode for recording the electrical activity of the cells.

These applications indicate the promise of three dimensional graphene transistor as an all-in-one multimodal multifunctional transistor for smart biological interfaces.

ACKNOWLEDGEMENTS

I would like to thank my PhD advisor, Professor Sameer Sonkusale, for his continued support during last four years. His intellectual guidance, unconditional support and giving me freedom for pursuing new ideas helped me to perform high quality and innovative research. He was always inspiring me with creative ideas and was guiding me patiently during my PhD. In addition, humanity and professional attitudes are his extremely valuable characteristics.

I would like to thank Professor Qiaobing Xu (Biomedical Engineering, Tufts University), Professor Swastik Kar (Physics, Northeastern University) and Professor Mohammad Afsar (Electrical Engineering, Tufts University) for taking the time to serve as my PhD committee members. I want to thank Professor Qiaobing Xu for his advice and support on dielectrophoretic cell trapping and cell lysis project.

I would like to thank Dr. Pramod Singh for his valuable help and many technical discussions during his postdoctoral years at NanoLab, Tufts University. I also like to thank former and present lab managers of NanoLab, Dr. Sam MacNaughton and Robbie D'Angelo for their technical support and help. I want to thank present NanoLab members, Yu Chen, Guoqing Fu, Meera Punjiya, Kyoungchul Park and Saroj Rout because of their support and all the fun discussions in general. I would also like to thank Professor Ali Khademhosseini and Professor Mehmet Dokmeci (Harvard-MIT Division of Health Sciences and Technology) for their help and advices on the dielectrophoretic cell trapping

and cell lysis project, Professor Matthew J. Panzer (Chemical and Biological Engineering, Tufts University) for his valuable discussion and support in ionogel three dimensional graphene transistor project and Anthony D'Angelo, Kyle Alberti for their collaboration and help. I would also thank Dr. James Vlahakis lab manager of Tufts Micro and Nanofacility and staff of the Center of Nano Scale (CNS) at Harvard University for their technical support in clean room and microfabrication process during my PhD.

I am thankful from Tufts Electrical Engineering faculty and staff, international center staff and all other members of Tufts University, whose support enabled me to have an amazing experience during my study at Tufts University.

Finally my deepest gratitude to my father, mother and my family, for their endless support and scarifying during my PhD and all years of my education. I dedicate this dissertation to them.

TABLE OF CONTENTS

LIST OF FIGURES

CHAPTER 1

Introduction

1.1Dissertation motivation

Graphene is an atomically thin zero band gap semiconductor or semimetal, with a strong ambipolar electric field effect, remarkably high carrier mobility at room temperature, high carrier density and high saturation velocity. Due to extraordinary electrical properties of graphene, it has been suggested as a possible candidate for beyond-CMOS field effect transistor (FET) with applications mainly in RF and analog domain. For example implementation of an integrated RF receiver which can perform amplification, filtering and down conversion mixing has been reported in 2014 by IBM. This circuit can perform wireless communication at 4.3 GHz [1].

Besides having extraordinary electrical properties, graphene has many other interesting properties. It is mechanically strong and has good biocompatibility, it is electrochemically stable, shows excellent broadband optical transparency and can be made very sensitive to the surrounding media, making it a promising candidate for sensing and bioelectronics applications. Moreover it is easy to derive other forms of

graphene with different physical and chemical properties such as graphene oxide (GO) and reduced graphene oxide (RGO). The possibility of transferring graphene and its derivatives to various types of substrates make it an ideal candidate for flexible bioelectronics with applications in medical diagnostics and healthcare. Some specific bioelectronics applications are mass spectroscopy, field effect transistor based biosensors, gene and drug delivery, cell growth control and stem cells differentiation [2-6].

In this dissertation, application of graphene as electrodes in biology and life sciences is investigated. One of the important considerations for electrodes in biological environment is their biocompatibility and electrochemical stability. In biological background and in the presence of DC electric field, most of metal and other conventional electrodes, undergo faradic reaction. This can cause serious harm to the living cells by increasing the temperature of their surrounding and releasing stressor and toxic chemicals generated as undesirable byproduct of electrochemical redox reactions. Due to carbonaceous form of graphene, it is naturally biocompatible and non-toxic. Graphene is also inert material and fairly electrochemical stable. These make it an ideal conducting material for electronic interfaces with the biological world. In this dissertation, we use graphene electrodes for high throughput electrical trapping and lysis of cells for biotechnology applications.

Since graphene is atomically thin, its carrier transport is very sensitive to the environmental changes, and given that it has less intrinsic electrical noise, make it an excellent material as a sensor-transducer for many chemical sensing applications (e.g. gas, heavy metal etc.) [7,80,81].

Although two-dimensional crystalline structure of graphene makes it interesting for

many applications, it leads to some drawbacks. First; because of the atomic thickness of graphene, its carrier transport is very sensitive to the trapped charges on the substrate. These trapped charges affect the carrier mobility and functionality of the graphene based devices. Second; although graphene has high carrier density, due to its atomic thickness, transistors made of 2D single layer graphene show low current capacity. Graphene generally needs to be transferred to the desired substrate after growth. Difficulty of transferring graphene and cleaning the residue of the photoresist remained behind from the transferring process which affects the mobility and noise performance of devices are other drawbacks.

Expanding two dimensional graphene to three dimensions can add many interesting properties to the graphene and also addresses some of the issues mentioned earlier. The higher surface area of three dimensional graphene makes it more attractive for sensing applications. It increases the sensitivity and volumetric coverage of a sensor. It also increases the current capacity of the graphene FET. Although we have not studied the effect of the substrate on the carrier transport in the 3D graphene, we believe that in a three dimensional form of graphene, layers can be suspended and as a result the undesirable effects of the substrate will be suppressed. The simplicity and photoresist free process of transferring to any desired substrate are other advantages of using the three dimensional form of graphene studied in this dissertation.

We have studied the design, fabrication and realization of a three dimensional graphene transistor made of 3D graphene foam and show its extensive electrical characterization. The channel of this transistor is gated with ionic liquid and ionogel to form all around gate and double layer capacitance. Formation of a large double layer

capacitance results in high electrostatic control of the gate and low operating voltage. Due to high surface area of graphene foam, liquid gated transistor has great potential for different sensing applications and because of its all carbonaceous form, it can lead the way for real electronic interfaces with the biological world. Furthermore, since graphene foam consists of 3D network of graphene strips, it is fault tolerant and mechanically robust. The network structure of the graphene provides many possible pathways for carriers through the graphene foam even in presences of cracks, defects or impurities. These properties of graphene foam make it a suitable candidate for many physical sensing applications.

1.1.1 Biological needs and applications

In this dissertation, we have introduced three dimensional graphene transistors and proposed its application in physical, chemical, biological sensing and biotechnology applications. Our proposed transistor device has potential to be operated as a multi-functional all-in-one construct with many possibilities. While many applications can be envisioned for such a device, our work is motivated strongly by application in biology and biotechnology. Precise control and monitoring of the tissue during growth and healing is highly desirable in medical diagnostics and in fundamental biological studies. Platforms that can provide multiple functions in parallel are not yet fully developed in the literature, conventionally, performing multiple functions would require multiple sensors and actuators each targeted for individual function. Moreover such sensors would then be connected to external electronic instrumentation making it truly incompatible for either wearable or implantable applications. Especially when they need to be implanted in the body, one needs to consider many issues such as flexibility, biocompatibility and

immunity from foreign body immune reaction and also mechanical robustness for long term use. Since this device is made all of carbon, it is expected to be highly biocompatible. Graphene is one of the few materials that along with its biocompatiblity, it is also mechanically robust, electrochemically stable, optically transparent and has extraordinarily electronics properties. While planar two-dimensional graphene has shown a lot of promises, we would like to explore added functions and possibilities by moving to a three dimensional structure of graphene. In following chapters, we present two versions of three dimensional graphene transistor which are liquid and ionogel gated. The graphene foam used for fabrication of these transistors consists of mono to double layers and few layers of graphene grown on copper foam using CVD method. Beyond purely electronic function, we also propose its use as a chemical pH sensor, physical strain sensor and investigate the use of this device as a scaffold for electrogenic cells such as neuronal and cardiac cells. We have used proposed device to record the electrical signal from electrogenic cells grown on 3D graphene as a scaffold. Considering the functionality of this device for different applications, we believe that this device has potential to be used as a multifunctional device.

1.2 Dissertation contributions

In this dissertation we present some of the applications of two and three dimensional graphene in bioelectronics, sensing, electronics and biotechnology. The main contributions of this dissertation are as follow.

- We have shown that the two-dimensional graphene can be used as an electrochemically stable electrode in biological environment. We validate the idea with the implementation of graphene electrode in a microfluidic device for

dielectrophoretic (DEP) trapping of mammalian cells and lysing them which is an important biotechnological function in biology and life sciences.

- We have proposed a liquid gated three dimensional graphene transistor and validated its functionality experimentally. The channel of this device is made of a mono to double layer of graphene grown on the copper foam using CVD. To keep the consistency between transistors, we fabricated devices with long channel (600 to 1200 µm) size comparable with the average size of the pores in the graphene foam (360 µm). Transistor shows ambipolar behavior with a Dirac point located at -0.4 V. For the device with the channel length of 600 µm, we have found the on/off ratio of 5. The current capacity of this device is about ~5 mA at 0.7 V drain to source voltage and it increases with further decrease of the channel length.
- We have also designed and fabricated a flexible ionogel-gated three dimensional graphene foam based transistor on a thin Parylene film demonstrating high current capacity and low operating voltages. The substrate was merely 28±2 µm thick for high flexibility. The channel of this transistor is made of few layers of graphene foam. The use of gel like dielectric provides inherent mechanical stability. For the device with the channel length of 600 µm this device shows the drain to source current of ~90 mA at 2 V drain to source voltage. Our results show that the current capacity of this device is ~26.72 times more than equivalent two dimensional graphene transistor.
- Sensing pH using the liquid gated graphene transistor in high ionic strength medium (higher than 100 mM) is challenging. We have introduced a high sensitivity pH sensor based on the presented three dimensional transistor device. By adding a 20

nm of HfO_2 all-around the 3D graphene using atomic layer deposition system (ALD) we provide an ion-sensitive gate surface. The pH sensitivity of 79 mV/pH even in high ionic strength medium (150 mM) and blood serum (between 270 to 297.4 mM) is achieved. We attribute the high sensitivity and beyond Debye length sensitivity of this device to the special three dimensional structure of the graphene which provides high sensing surface area and existence of chemical binding sites on the oxide coating of the transistor channel.

- We have implemented a strain sensor based on three-dimensional graphene foam. It is found that this device shows a stable response to the strain in the range of 0.5% to 30% with the gauge factor of 1.5 to 71.3 for different percentages of strain. We believe that the higher dynamic range and sensitivity in this device is due to the networked structure of the foam which provides many possible pathways for carriers even in the presence of defects and cracks during high strain.
- Multilayer free standing graphene foam and mono to double layer of graphene foam were used as non-planar and three dimensional scaffold for growing PC-12, Schawnn and HL-1 cell lines. Our results show that cells maintain their viability on the graphene foam. The HL-1 cells are myocyte cells which contract continuously. We have grown them on the mono to double layer 3D graphene foam and recorded their signal using the same scaffold.

1.3 Dissertation organization

In chapter 2 of this dissertation a brief overview on the graphene chemistry and physics is given. Different methods of the producing graphene are discussed and finally some of the applications of graphene in electronics, sensing and biology are presented. In

chapter 3, the utilization of graphene electrode in transparent micro-well arrays for high throughput cell trapping and lysis is discussed. We have shown that graphene electrode can be a very good replacement of the conventional indium tin oxide (ITO) and metal electrodes in electrolytic environment. In the first part of the chapter 4, the ionic liquid gated three dimensional graphene based transistor is introduced and electrical characterization is presented. In the second part of chapter 4, a high current capacity ionogel gated graphene transistor, its functionality and electrical characterization are discussed. A high sensitivity pH sensor based three dimensional graphene transistor is introduced in chapter 5. The results of pH sensing using this device at high ionic strength medium and blood serum are presented. Chapter 6 showcases the work of using graphene foam with multiple layers of graphene as a strain gauge sensor. The speed and cyclic measurements are presented. The interaction of the different mammalian cell lines with free standing graphene foam and mono to double layer graphene foam is discussed in chapter 7 and it is shown that the cells viability is not dependent on the number of the graphene layers in foam (multilayer free standing foam grown on nickel foam and mono to double layer graphene foam grown on copper foam using CVD method). The results of recording the electrical signal from the cells using the graphene foam is also presented in this chapter. Chapter 8 concludes this dissertation with a brief discussion over possible further improvement on the device fabrication, modeling and other possible applications.

CHAPTER 2

Background

Graphene is one of the crystalline allotropes of carbon, consisting of two dimensional carbon network, arranged in honeycomb lattice structure, common to all forms of carbon materials. It can be wrapped up to make zero dimension Bucky ball structures such as buckminsterfullerene, rolled to make one dimensional carbon nanotubes and stacked layer by layer to form three dimensional graphite. The band structure of graphene has been studied theoretically since 1947 but the existence of the independent monolayer of carbon was not proven experimentally until the isolation of carbon monolayer from the graphite in 2004. The Novoselov's group in Manchester separated a monolayer of carbon for the first time, with a mechanical exfoliation method using scotch tape [8,9].

Graphene is a zero band gap semiconductor or a semimetal. It has linear dispersion equation and a two dimensional gas of massless chiral Dirac fermions that gives rise to its exciting electrical and magnetic properties such as high conductivity, high Fermi velocity and anomalous integer quantum hall effect. Graphene has also many other interesting properties such as optical transparency, electrochemical stability, remarkable mechanical

strength, biocompatibility and high sensitivity to the surrounding environment [10,11].

In this chapter we discuss the electronic properties of graphene and introduce some of the main applications of graphene in various fields of science and technology.

2.1 Graphene electronic properties

Before starting the study of the electronic properties of graphene, a brief study of the graphene chemical structure is beneficial. Graphene is a honeycomb lattice structure of carbon atoms with $1s^2\ 2s^2\ 2p^2$ configuration and 4 valence electrons. The 2p valence sell hybridizes with the 2s sub-shell in graphene and forms sp, sp^2 or sp^3 hybrid orbitals. As a result there are three valence electrons in the sp^2 orbitals and one in unhybridized $2p_z$ orbital in graphene, as it is shown in figure 1(a). The sp^2 hybrid orbitals in graphene form covalent bonds with the angle of 120 ° apart from each other and lie in xy plane. The chemical bonds between sp^2 orbitals known as σ bonds are very strong and directional and result in the mechanical strength and 2D planar structure of graphene. The $2p_z$

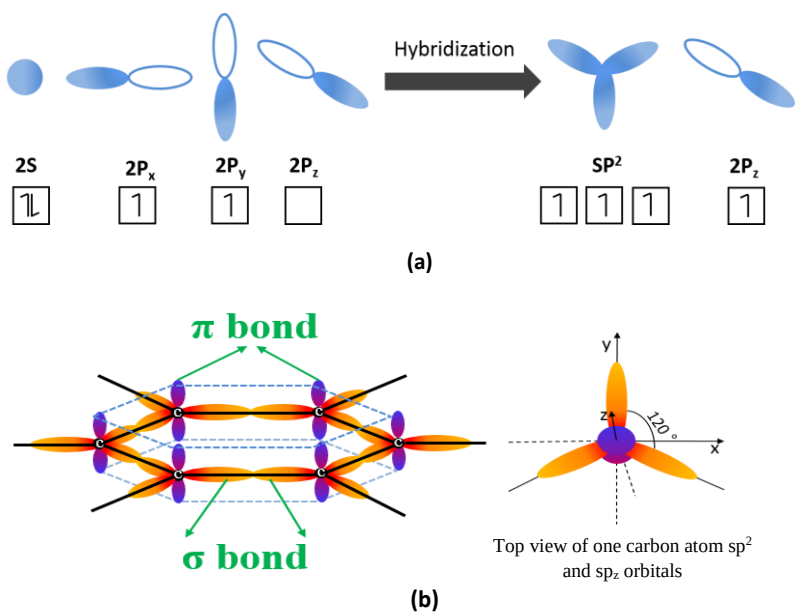

Figure 2.1. Graphene chemical structure. (a) Hybridization and forming sp^2 and $2p_z$ orbitals in graphene. (b) Graphene π and σ bounds.

orbitals are perpendicular to the sp^2 orbitals and participate in forming π and π^* bonds in graphene, lead to the interesting electronic and optical properties of graphene [10]. Figure 2.1 (b) shows the schematic of σ and π bonds in graphene.

The band structure of graphene was studied by P. R. Wallace in 1947 for the first time. This band structure was used for study of graphite electronic properties for several years. There have been several modifications on the theory of the band structure of graphene in following years [11]. The honey comb lattice of graphene and its Brillouin zone has been shown in figure 2.2(a). The unit cell in graphene consists of two carbon atoms. The lattice vectors and reciprocal-lattice vectors of graphene can be written as:

$$a_1 = \frac{a}{2}\left(3, \sqrt{3}\right), \qquad a_2 = \frac{a}{2}\left(3, -\sqrt{3}\right) \tag{2.1}$$

$$b_1 = \frac{2\pi}{3a}\left(1, \sqrt{3}\right), \qquad b_2 = \frac{2\pi}{3a}\left(1, -\sqrt{3}\right) \tag{2.2}$$

Where a_1 and a_2 are lattice vectors, b_1 and b_2 are reciprocal-lattice vectors and a is lattice constant which is the distance between the two nearest carbon atoms (1.42 A°). Tight-binding Hamiltonian in graphene is given as

$$H = -t \sum_{\langle i,j\rangle,\sigma} \left(a^{\dagger}_{\sigma,i}\, b_{\sigma,j} + h.c.\right) - t' \sum_{\langle\langle i,j\rangle\rangle,\sigma} \left(a^{\dagger}_{\sigma,i}\, a_{\sigma,j} + b^{\dagger}_{\sigma,i} b_{\sigma,j} + h.c.\right) \tag{2.3}$$

Where $a_{i,\sigma}$ and $(a^{+}_{i,\sigma})$ are annihilation and creation operator. The t is the hopping energy of the nearest neighbor (2.7 eV) and t', is the hopping energy of the next nearest neighbor. This equation describes the hopping of unbonded $2p_z$ electrons and formation of π and π^* bonds in valence and conduction bands respectively. This Hamiltonian results in the following energy band

$$E_{\pm}(K) = \pm t\sqrt{3 + f(K)} - t' f(K) \tag{2.4}$$

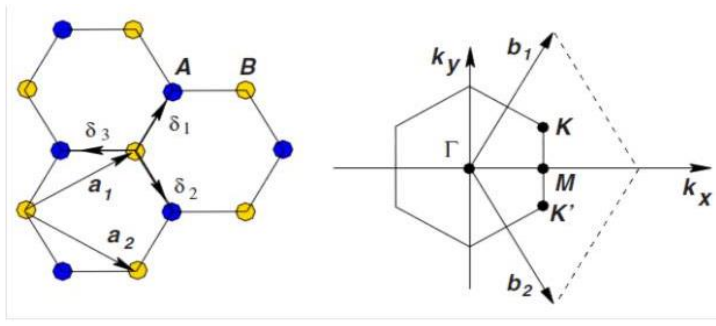

(a)

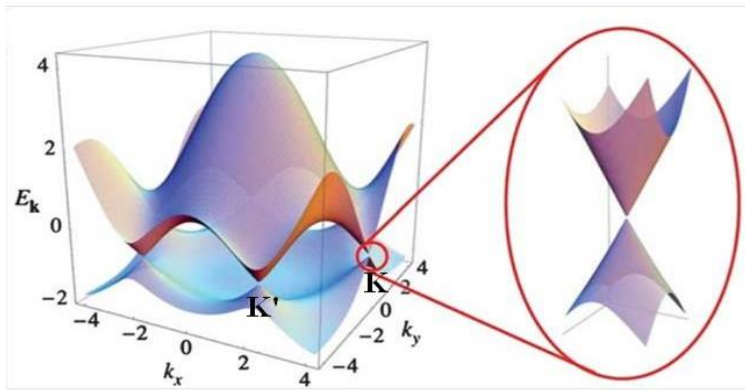

(b)

Figure 2.2. Graphene lattice structure and band structure. (a) Honeycomb lattice of graphene at right side and its Brillouin zone at left side. Vectors a_1 and a_2 represent the lattice unit vectors. Brillouin zone of graphene and Dirac cones, located at the *K* and *K'* points have been shown at the left side [12]. (b) Left: the band structure of graphene in the honeycomb lattice. Right: zoom-in of the energy bands close to one of the Dirac points [13].

$$f(K) = 2cos\left(\sqrt{3}\, k_y a\right) + 4\cos\left(\frac{\sqrt{3}}{2} k_y a\right) cos\left(\frac{3}{2} k_x a\right) \qquad (2.5)$$

Where the *K* is wave vector. Here the plus sign applies to π^* bond and the minus sign to π bond. Figure 2.2(b) shows the band structure of graphene and a zoomed in of the band structure at Dirac point (*K* and *K'*). Dirac point is located at the edge of band structure of the graphene where the valence and conduction band touch each other. This is why graphene has zero band gap [12]. By expanding the band structure at $k=K+q$ where $|q| \ll |K|$ the following equation is derived

$$E_{\pm}(q) \approx \pm v_F |q| + O[(q/K)^2] \qquad (2.6)$$

Where v_F is Fermi velocity and is ~10^6 m/s. Equation (2.6) is called the dispersion relation of graphene. The low energy dispersion energy close to the neutrality point, resembles massless fermions where electrons in graphene, behave as the ultra-relativistic particle, such as photon. The massless chiral Dirac fermions of graphene, in the presence of magnetic field, show anomalous integer quantum hall effect at room temperature because of high Dirac velocity and high cyclotron energy of the electron in graphene [9,13]. Dirac fermions can penetrate through high and wide potential barriers which make them insensitive to external electrostatic potential. This phenomenon is called Klein paradox [14]. The immediate result of the Klein paradox is very long mean free path and ballistic transport in graphene. Electrons in graphene can travel over micron length without scattering, the mean free pass of 0.4 µm for carriers in graphene has been reported [9].

The density of state in graphene can be derived using equation (2.4). For *t'* equal to zero, density of states of the unit cell of graphene is given by

$$\rho(E) = \frac{4}{\pi^2}\frac{|E|}{t^2}\frac{1}{\sqrt{Z_0}}F\left(\frac{\pi}{2}, \sqrt{\frac{Z_1}{Z_0}}\right) \qquad (2.7)$$

$$Z_0 = \begin{cases} \left(1 + \left|\frac{E}{t}\right|\right)^2 - \frac{\left[\left(\frac{E}{t}\right)^2 - 1\right]^2}{4}, -t \le E \le t \\ 4\left|\frac{E}{t}\right|, -3t \le E \le -t \vee t \le E \le 3t \end{cases}$$

$$Z_1 = \begin{cases} 4\left|\frac{E}{t}\right|, & -t \le E \le t \\ \left(1 + \left|\frac{E}{t}\right|\right)^2 - \frac{\left[\left(\frac{E}{t}\right)^2 - 1\right]^2}{4}, & -3t \le E \le -t \vee t \le E \le 3t \end{cases}$$

Where $F\left(\frac{\pi}{2}, \sqrt{\frac{Z_1}{Z_0}}\right)$ is a complete elliptic integral of the first kind. Close to the Dirac point, the density of state is given by

$$\rho(E) = \frac{2A_c}{\pi v_F^2}|E| \qquad (2.8)$$

Where

$$A_c = \frac{3\sqrt{3}a^2}{2} \qquad (2.9)$$

A plot density of the stats per unite cell given by energy dispersion relation in equation (2.3), has been shown in figure 2.3

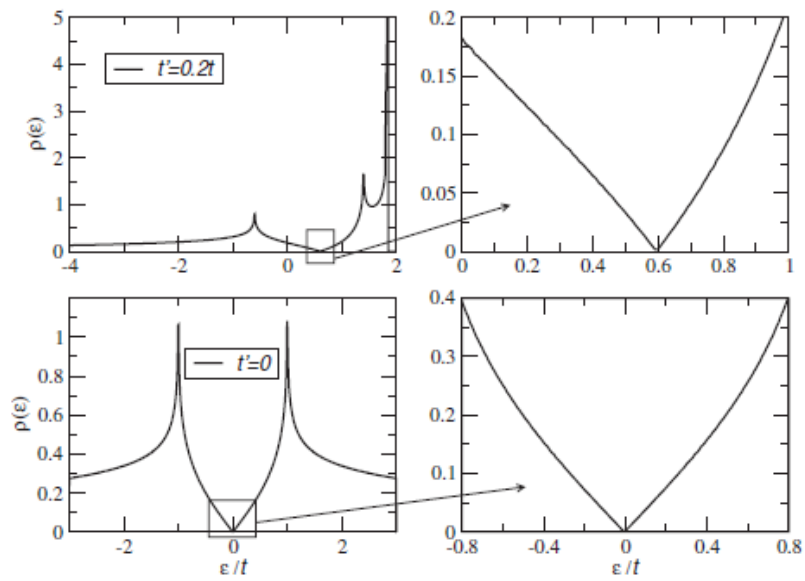

Figure 2.3. Density of states per unit cell versus energy in graphene (in the units of t), t'=0.2t on the top and t'=0 at the bottom [11].

2.2 Graphene production

There had been many efforts to produce graphene for several decades before the successful exfoliation of the monolayer graphene from graphite in 2004 by Novoselov's group. In fact the oldest report for isolation of mechanically exfoliated graphene

containing 15 layers of carbon was reported by Fernandez-Moran at 1960. Many other researchers has reported the production of multilayer graphene using various methods before 2004 [15-18]. Today graphene is mass produced on different substrates like as glass, polymers, SiC, Si, etc., using variety of methods such as chemical vapor deposition (CVD), mechanical exfoliation and wet chemical methods.

Among various techniques for producing graphene layers, the exfoliated graphene using scotch tape still is one of the highest quality of graphene with the lowest number of defects after it is transferred to the desired substrate. Mechanical exfoliation is feasible for production of graphene, because layers of carbon in graphite are stacked with weak van der Waals interaction. The inter layer van der Waals energy in graphite is only about 2 $eV.nm^{-2}$ therefore, for exfoliation of graphene one needs to apply just about 300 $nN/\mu m^2$ force which can be easily achieved using an adhesive tape [19]. This method requires successive sticking and peeling process to thin the graphite flake to the monolayer graphene flake. After confirming the presence of a smooth flake on the tape using optical microscope, it is transferred to an appropriate substrate which is silicon coated with 300nm or 90 nm of the SiO_2 film. The color of graphene on such substrates will be different depending on the number of carbon layers (i.e. different thickness) due to additional light pathway through the silicon oxide layer (Fabry-Perot multilayer cavity) [20,21]. As depicted in figure 2.4, graphene with more number of layers appears yellow and turns to purple as the number of layers decreases. Mechanical exfoliation of graphene using scotch tape is simple and efficient and graphene produced using this method carries excellent electrical properties. However, it has disadvantages that it leaves a residue of glue and size of graphene is small. Large scale production of graphene using this method

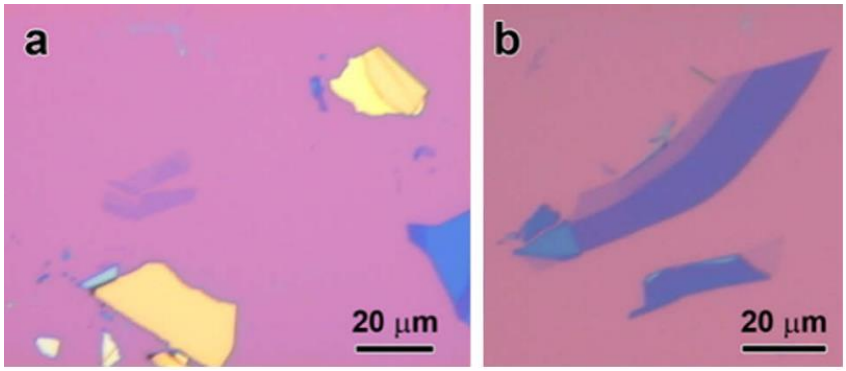

Figure 2.4. Photo of the mechanically exfoliated graphene on 300 nm SiO_2 film, captured with optical microscope. (a) Graphite seems yellowish. (b) Few-layer graphene and single-layer graphene appear in purple and blue color [20].

is not impossible but it is very challenging.

Graphene can be also produced by wet chemical methods. The principle of this method is penetrating an intercalating solution between graphene layers in graphite and loosening the van der Walls bonds. The intercalated stacks then separate easily with an applied force due to vapor pressure of solution or ultrasonication. Although the wet chemical methods are inexpensive and high throughput but there are several drawbacks associated with those. The final products of these methods are a mixture of mono and few layers of graphene flakes and the size of flakes is not adjustable. Existence of the defects and poor quality of graphene produced with wet chemical methods are also big drawbacks of this method [22-24].

Another technique of producing graphene is growing it on supportive substrates with two mechanisms, decomposition of carbides at high temperature and epitaxial growth of graphene. Growth of the graphene layers on carbides had been reported in 1956 for the first time [25]. Recently, the growth of an ultrathin graphite (2.5 and 3 monolayer of graphene) in a wafer scale with the precise control on the growth factors has been

reported and attracted a lot of interests due to the compatibility of SiC substrate with current semiconductor technology [26,27].

Silicon carbide crystal structure can be defined as a repetition of bilayers of SiC. One face of SiC is silicon terminated and the other face is carbon terminated. Growing graphene on the Si face leads in the formation of graphene with n-type conduction and the lower mobility of carriers than a graphene grown on C face with p-type conducting characteristics. The surface treatment of supportive substrate has certain effect on the quality of the grown graphene [28]. To grow graphene on SiC, silicon carbide is prepared by hydrogen etching at $\geq 1000\ ^{\circ}C$ in ultra-high vacuum to remove oxides from its surface. In the next step the sample is heated at the temperature range of 1250 °C to 1460 °C to form graphene. At high temperature Si atoms sublime from the surface and carbon atoms remain behind and form graphene. Growth of a monolayer graphene on SiC at the range of temperature between 1500 to 1550 °C with the mobility of 4400 and 2000 $cm^2/V.s$ has been reported for hole and electron respectively. Time and temperature play critical roles in controlling the number of graphene layers [29].

Graphene is also grown on various metallic substrates like as Cu, Ni, Pd, Co, Pt, Ru and Ir using chemical vapor deposition (CVD) [30-34]. In this method carbon is combined with metal and then is dissociated to form graphene.

Growth of graphene on nickel results in formation of multilayer of graphene. This is because large amount of carbon can be absorbed in nickel and results in formation of graphite. To minimize the formation of graphite, the use of crystalline Ni film deposited on silicon/SiO_2 using e-beam evaporator with the thickness of 300 nm, instead of bulk Ni substrate has been demonstrated. In this method, sample is heated at 1000 °C in argon

atmosphere, following with insertion of mixture of methane, hydrogen and argon gasses with appropriate ratio to the chamber. Since the segregation of carbon from the metal carbide is very fast, it leads to forming multilayer graphene within the Ni grains and at its grain boundaries during cooling down of sample. The key point here is to cool down the sample very fast (~10 °Cs^{-1}) to prevent the forming multi layers of graphene. The electron mobility of 3700 $cm^2/V.s$ and sheet resistance of ~280 $\Omega.m^{-2}$ has been reported for the graphene grown by this method [30]. Although growth of graphene on Ni film followed with fast cooling decreases the ratio of the multilayer to few layers of graphene in the final product but still the final product is the combination of monolayer and multilayer islands of graphene over a large area.

Formation of semiconductor monolayer graphene islands with the size of 20nm to 200nm, grown on Pd (111) with 0.3±0.1 eV band gap, has been reported [33]. Figure 2.5 shows the monolayer graphene islands grown on Pd. It is also demonstrated that high structural quality of monolayer graphene can be grown at low pressure using CVD of ethylene on Ir (111) [31].

Copper foil is widely used to grow monolayer of graphene. Graphene is grown on copper foil at temperature about 1000°C using CVD in the presence of the methane and hydrogen mixture by surface catalyzed method. Growth of graphene by this method yields production of large area of monolayer graphene and few percentages of multilayer graphene flakes. Growth of centimeter size of graphene with more than 94 % of single layer graphene, less than 5% of two and three layers flakes and less than 1% of few-layer (<10) of graphene and with the carrier mobility and carrier concentration of ~4050 $cm^2V^{-1}s^{-1}$, 3.2×10^{11} cm^{-2} on copper foil has been reported.

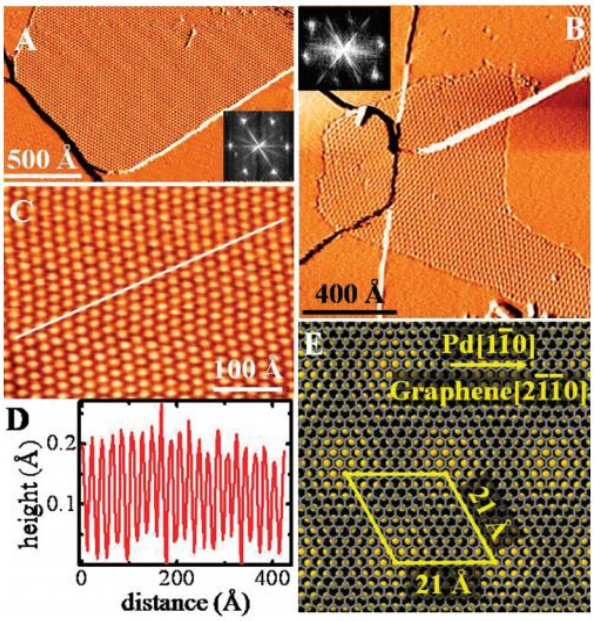

Figure 2.5. STM images of graphene grown on Pd(111). (a and b) Derivative filled-state STM images of graphene islands in, (a) I_T = 0.13 nA (b) I_T = 0.22. (c) High-resolution filled-state STM image of the graphene island at 968 K. (d) Surface height profile along the white line shown in panel C. (e) Atomic model of graphene aligned with the Pd atoms [33].

Figure 2.6 shows the scanning electron microscopy image of graphene grown on copper foil with 25 µm thickness. The presence of flakes of two and three layers of graphene, wrinkles and steps is visible. The photos of transferred graphene layer onto the SiO_2/Si and glass substrates have been shown in figure 2.6(c) and 2.6(d) [32]. Graphene can also be grown on copper film deposited on silicon, which is compatible with the standard process of silicon technology.

Oxidization of copper surface before growing graphene, improves the quality of the grown graphene. In a study performed recently has been shown that presence of oxygen on the copper surface before graphene growth, either segregated out from copper in oxygen rich copper substrate or adsorbed from ambient during exposing copper substrate to the oxygen, passivates the active sites on the copper surface and prevents binding and accumulation of hydrocarbons which decreases the graphene nucleation density and lead

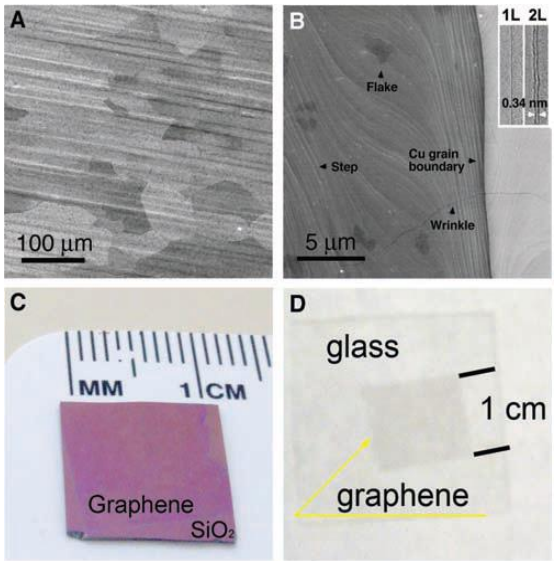

Figure2.6. Photos of the graphene grown on copper foil and transferred on SiO_2 and glass (a) Scanning electron microscopy image of graphene grown on a copper foil. (b) SEM images of wrinkles and grain boundary in graphene flakes. Inset in (b) shows TEM images of folded graphene edges. (c) Graphene transferred onto a SiO_2/Si. (d) Graphene transferred onto glass substrate [32].

to the growth of centimeter scale single crystal graphene domains. Figure 2.7 shows the SEM and optical images of graphene grown on the coper foil passivated for 2 min and 5 min with oxygen prior to the graphene growth. Produced graphene on modified copper surface shows the comparable electrical quality with the graphene produced by mechanical exfoliation, with the carrier mobility between 40,000 to 65,000 $cm^2V^{-1}s^{-1}$

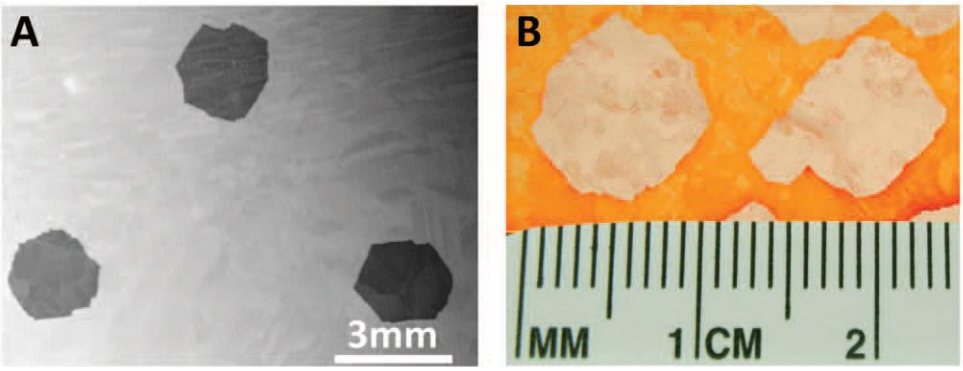

Figure 2.7. SEM image and optical photos of large single crystal graphene domain on oxygen rich copper (a) SEM image of single crystal graphene domains on oxygen rich copper sample which is also exposed to oxygen. (b) Optical image of the large scale single crystal graphene domain on oxygen rich copper sample which is exposed to oxygen prior to the growth of graphene [35].

at 1.7 K and between 15,000 to 30,000 $cm^2V^{-1}s^{-1}$ at room temperature [35].

2.3 Disorders in graphene

Existence of disorders in graphene affects the electronic properties of the graphene effectively. Although existence of the strong σ bands in graphene makes it difficult for entry of alien atoms into its crystalline structure, however ripples and wrinkles, topological defects, impurities on the graphene surface or on the substrate, vacancies, cracks and edge effects can effectively change the carrier transport in graphene and introduces sites for chemical interaction with environment. Below some of the most common defects in graphene and their effects on the graphene electronic properties will be discussed.

2.3.1 Ripples and wrinkles

Graphene is similar to a soft membrane and once it is placed on a surface, its topology changes to almost the same topology of a supportive substrate. It has been shown that graphene grown on metal substrate contains ripples due to the difference in the thermal expansion between metal and graphene during growth process. Theoretical study of a free standing graphene predicts the existence of intrinsic ripples in graphene. More importantly during the transfer of graphene from one substrate to another, wrinkles with varieties of width, length and high are formed. Figure 2.8 shows three major classes of wrinkles which are typically formed in graphene grown on metallic substrates, ripple, standing collapsed wrinkles and folded wrinkles [36]. Presence of wrinkles affects carrier density and mobility of graphene. In the case of a simple ripple shown in figure 2.8 (a) the change in the carrier density can be estimated with considering it as a perturbation feature. To do that one can define the height profile of a ripple as follow

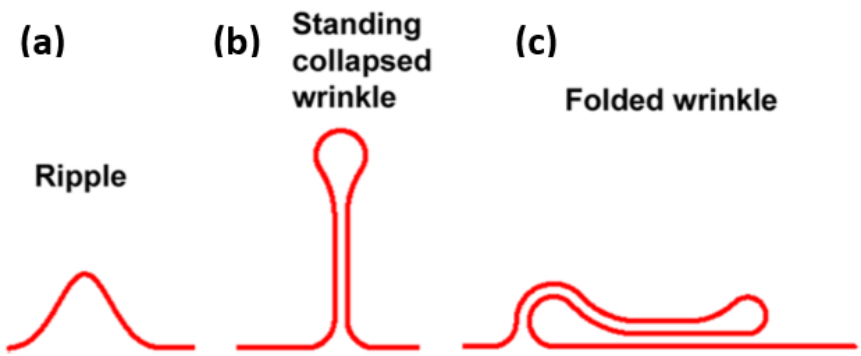

Figure 2.8. Schematic of different types of wrinkles in graphene. (a) Ripple. (b) Standing collapsed wrinkles. (c) Folded wrinkle [36].

$$z = Ae^{\left(-\frac{r^2}{b^2}\right)} \tag{2.10}$$

Where the ratio of *A*, height, to *h*, mean width of Gaussian, gives the bumps magnitude and shape which is the perturbative parameter. The variation between 1% to 10% in the local density of states of the graphene with the change in the ratio of *A/b* between 0.1 to 0.3 is reported. The ripple decreases the Fermi velocity and produces effective magnetic field perpendicular to the graphene sheet [37]. Ripples cause a potential in graphene that is proportional to the square of the curvature and ripples

$$\Phi = -\propto \frac{3a^2}{4}(\nabla^2 z)^2 \tag{2.11}$$

Where $\propto$ is equal to 9.23 eV, *z* is the height profile and *a* is the distance between carbon atoms [38]. Standing and folded wrinkles in the graphene can be formed in variety of sizes. Wide wrinkles, wider than 20nm, mostly have about 1nm height, while narrow wrinkles can be in different range of height between 2 to 6nm as it is shown in figure 2.9. Neglecting hybridization between layers, a folded wrinkle can be considered as a trilayer of graphene. It has been shown that if a folded wrinkle forms along the length of the

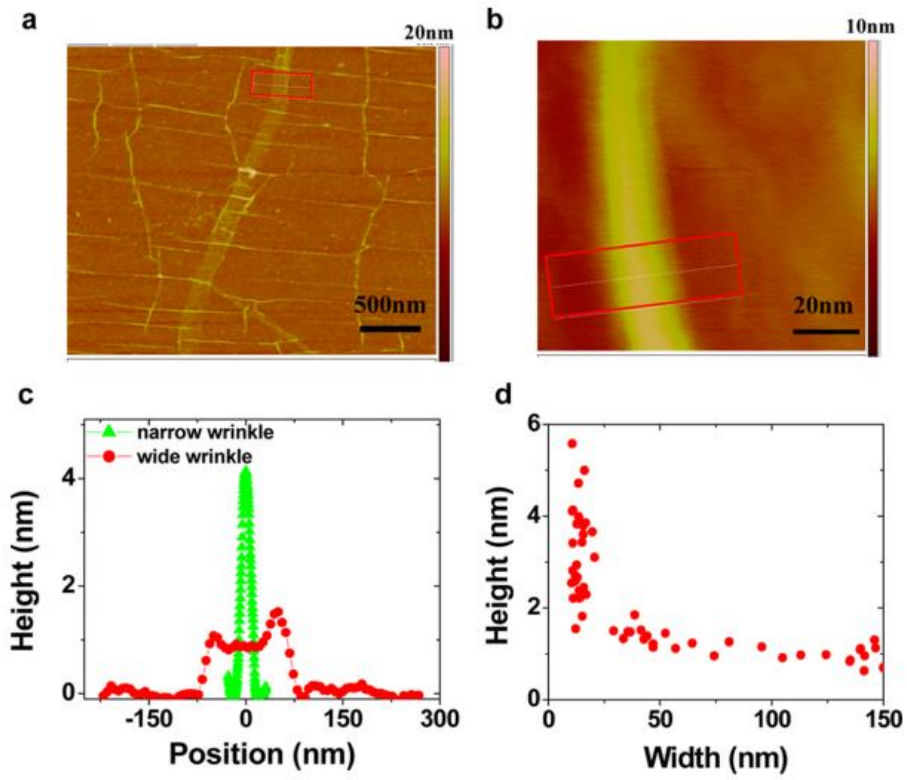

Figure 2.9. The topographies of wrinkles in graphene. (a) AFM image of graphene transferred on SiO_2/Si substrate. (b) AFM image of a narrow wrinkle. (c) The height profile of a narrow and wide wrinkles. (d) The statistical distribution of the wrinkles versus their width in a transferred graphene piece [36].

channel in a field effect device, at large gate voltages, almost all of the carriers remain at the bottom layer of trilayer of graphene, while close to the Dirac point, carriers distribute almost equally between layers which is due to nonlinear charge screening in the folded wrinkle. But this is not the case when wrinkle forms across the channel of the device. Considering the added channel length due to the width of wrinkle, the channel resistance across a folded wrinkle should be an order greater than observed experimental results. This difference can be explained by considering tunneling of carriers through trilayer of graphene which results in decreasing the resistivity. The effect of wrinkle on graphene resistivity is different when the resistance is measured between two points along with wrinkle and across of it as it is shown in figure 2.10.

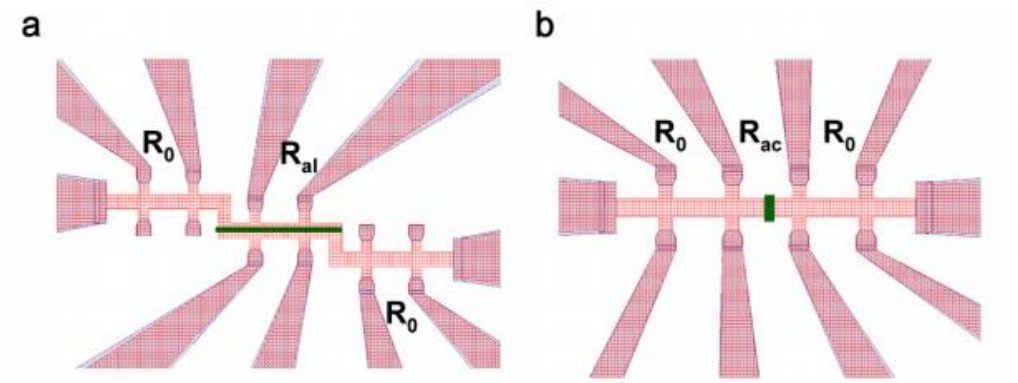

Figure 2.10. Two different configurations for measuring the carrier transport through a wrinkle. (a) Along the wrinkle. (b) Across the wrinkle [36].

The resistivity of graphene close to the neutrality point, decreases when wrinkle is along with channel length but it remains almost the same when resistivity measured across the wrinkle. It has been reported that trapped impurities inside the folded wrinkles do not have significant impact on the conductivity of the graphene [36].

2.3.2 Impurities and vacancies

Presence of impurities and vacancies in graphene has significant effect on the functionality and performance of graphene based electronics devices. Impurities, such as absorbed atoms on the surface or on the edges of graphene, can nucleate the electronic states, change the carrier concentration and act as the scattering centers in the graphene. In the presence of impurities, density of states decreases with decreasing the distance from the center of them. Impurities cause the resonance in the density of states known as virtual bound states which is strongly dependent to the number of impurity atoms [39,40]. They change the carrier concentration and as a result shift the Fermi energy, $E_{f\approx} v_f \sqrt{n_{im}}$ and decrease the elastic mean free pass, $d_{elas} \approx \frac{a}{\sqrt{n_{im}}}$ (n_{im} is impurities per carbon atoms). Impurity atoms create localized and semilocalized states in graphene with the

wave function which decays with distance from the impurity atom, r, as 1/r [11]. Vacancies in the graphene also lead to formation of localized state. These states do resonance in the vicinity of the Fermi level when electron and hole symmetry is disturbed. More detail can be found in publications [41].

2.3.3 Localized states closed to the edges and cracks

At the edge of the graphene, localized states can be defined. Edge of graphene has active sites which absorb impurity atoms and deform the edges. Uncompensated atoms at the edge of graphene form mid-gap states. The number of these states is dependent to the difference between the numbers of sites between two sublattices (See graphene sublattices in appendix A). Localized states also can be formed as the result of existence of cracks and vacancies [11].

2.3.4 Coupling to magnetic impurities

The immediate consequence of magnetic impurities existence in graphene is Kondo resonance between impurity atoms and electrons in graphene. Kondo effect is the phenomenon that the electron scattering increases with deceasing the temperature in the presence of magnetic impurities [42]. Most of the time magnetic impurities are induced chemically, by deposition and intercalation. Some reports suggest the Kondo resonance can be tuned by changing the chemical potential using external gate in the case of weak exchange coupling. But it is important to point that if the scalar potential of impurity comes in to the count, even close to Dirac energy, Kondo resonance still exists. [11,43-46].

2.4 Graphene applications

2.4.1 Graphene based field effect transistor (GFET) potential applications in analog/RF circuit and digital logic

Graphene based field effect transistor has attracted a lot of attention due to interesting electronics properties of graphene such as high carrier density and high carrier mobility at room temperature. The functionality of the field effect transistor strongly depends on the electronic properties of the channel which is usually a semiconductor material connected to two ohmic contacts, source and drain. On the top of the channel there is a metallic gate separated by a dielectric from it. The carrier concentration of the channel can be controlled by applying electric field on the gate. Carriers in the channel conduct current by applying voltage between drain and source. For analog and RF applications the speed of the transistor is key parameter which depends on the several fundamental factors. Some of these factors such as mobility of the carrier are related to the intrinsic material properties of the channel and some are related to the design and fabrication parameters such as gate length. To achieve high cut off frequency, defined as a frequency which the small signal current gain drop to unity, high carrier mobility, long mean free path and shortening of the gate length should be achieved. By shortening the gate length some fundamental issues rise. The functionality of the short gate length transistors suffers from short channel effect and series resistance (channel resistance, channel-source and channel-drain resistance). Short channel effect occurs when the channel length is comparable with the width of the source and drain depletion region. The edge effect increases the off-state leakage current and causes V_T roll-off and drain-induced barrier lowering (DIBL). The short channel effect can be suppressed by decreasing the dielectric gate thickness and thinning the gate controlled region. Since graphene consists of

monolayer of carbon atoms, it can be an ideal replacement of conventional semiconductors in the short channel transistors. Furthermore high carrier mobility at room temperature and very high mean free path in graphene make it suitable for RF applications. But there is a drawback for using graphene for high speed transistor applications. To reach the maximum speed of transistor, it should saturate for drain current but this usually does not happen in a graphene transistor. However, recently some graphene based circuits have been demonstrated for RF and analog applications. Figure 2.11 shows the schematic and optical photo of an IC circuit consisted of three stage graphene receiver made by IBM. The DC performances of three transistors in this circuit are shown. This IC can perform amplification, filtering and down conversion mixing and it can accomplish wireless communication at 4.3 GHz [1].

FETs in digital logic circuits are mostly used as a switch. To make more and more compact and advance digital circuit, the channel length and the overall size of transistor should be decreased. Currently 22nm technology mode is commercialized and 14 nm gate length transistor is going to be in mass production soon. Since the silicon based electronics is touching the limit of scaling, graphene could be a viable candidate for replacement of conventional semiconductors for short channel transistors.

For a switch in digital logic circuit, high on/off ratio of 10^4 to 10^7 and symmetrical threshold voltage for conducting in n and p type are required. Semiconductors with a bandgap of about 0.4 eV and higher can satisfy these requirements. Graphene can be very promising for making transistor with short channel due to its atomic thickness but nonexistence of the bandgap makes it difficult to switch off the graphene transistors [47]. Therefore opening bandgap in graphene is very desirable for digital logic

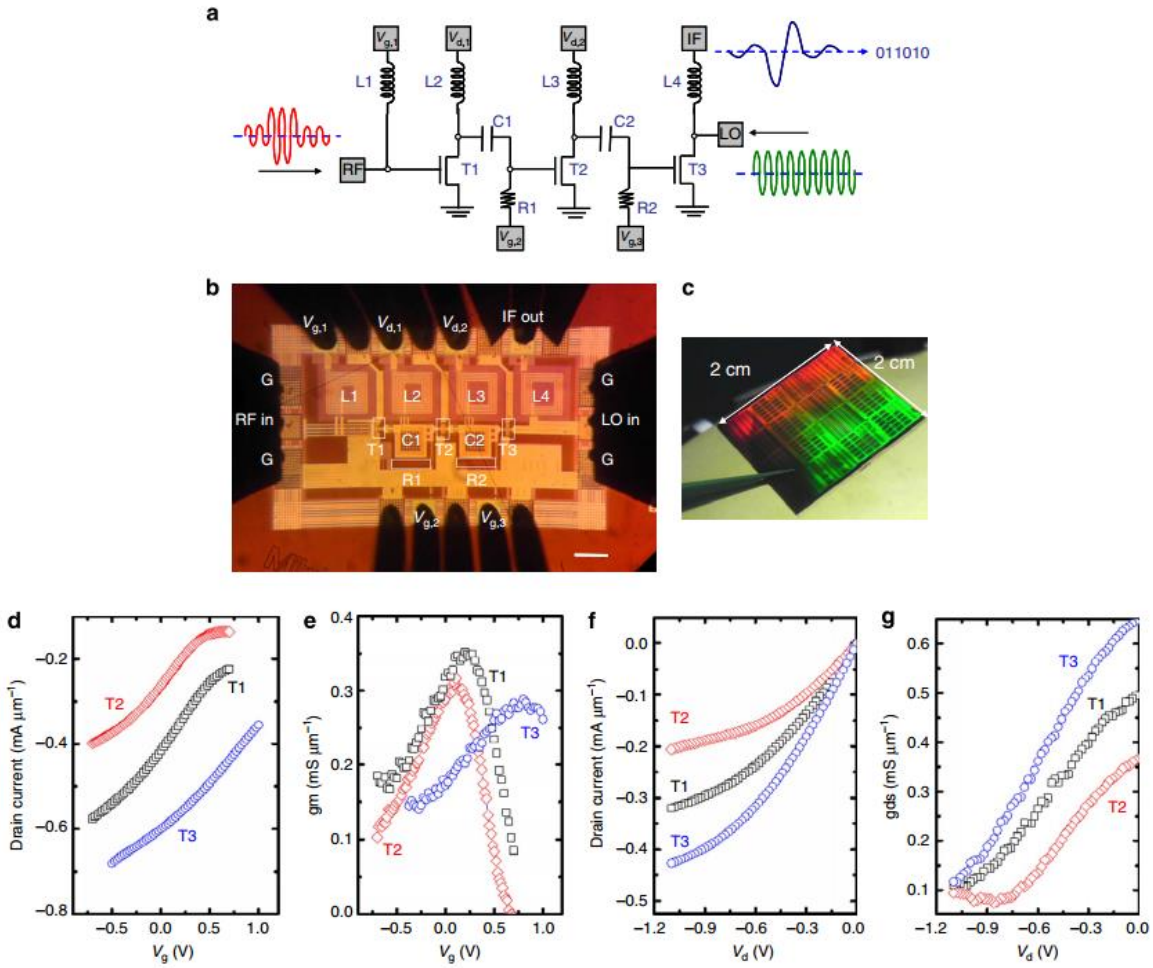

Figure 2.11. The three-stage graphene receiver circuit. (b) Optical micrograph of an IC. The circuit dimension is 1,020x600 mm^2. Scale bar is 100 mm. (c) Photo of a graphene IC chip. (d) to (g) DC performances of three transistors in this circuit [1].

applications and many researchers are actively working on finding an applicable approach to make this happen. Although opening band gap for graphene using different methods has been reported but it has been shown that it affects the electronic properties of graphene, especially the carrier mobility. In the following section, some of these methods and their effects on the mobility of carriers in graphene is discussed.

2.4.1.1 Band gap in graphene

One of the biggest drawbacks of graphene is the nonexistence of bandgap which is characterized by the absence of an off-state, and therefore prohibits its application for

digital logic. Opening the band gap for graphene has been reported using different methods such as inducing lattice mismatch, patterning adsorbed molecules in graphene, making nanoribbons and applying perpendicular electric field to the bilayer of graphene [48-53].

One of the approaches for opening bandgap in graphene is using the interaction of the graphene and some substrates such as h-BN and SiC that induces sublattice symmetry-breaking potential in graphene. The bandgap of 30 to 53 meV is reported in different literatures for graphene supported by h-BN but induced bandgap for graphene on SiC substrate has been debated widely [51,54-56]. It has been shown experimentally that patterned adsorption of hydrogen atoms onto the Moire superlattice of graphene grown on Ir (111) substrate can induce the bandgap of 40 meV [52]. One of the most proven approaches for opening the bandgap in the graphene is making nanoribbon. The bandgap energy of nanoribbons is strongly dependent on their widths. The bandgap energy between 0.5 eV to 3 eV has been predicted for nanoribbon with the width of 2.4 nm to 0.4 nm respectively [57]. However, edge disorders in nanoribbons has strong effect on the electronics properties of nanoribbons. The edges of graphene have uncompensated atoms between two sublattices which results in absorption of other molecules and adding impurities which affects the bandgap. Experimental results show the bandgap of about 0.4 eV for the ultra-smooth edge nanoribbon (prepended chemically) with the width of sub 10nm. Figure 2.12 shows the dependence of the bandgap and I_{on}/I_{off} ratios of graphene nanoribbon FET to the width of nanoribbon [58].

However, by opening the bandgap, the edge of conduction and valence band bends convert to the parabolic shape, therefore; dispersion equation of graphene is not linear

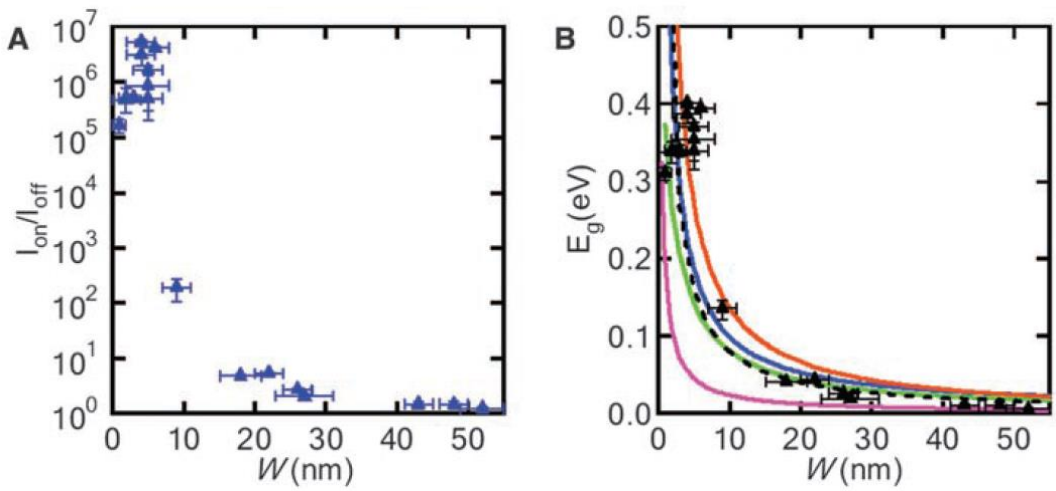

Figure 2.12. Dependence of bandgap of nanoribbon and on/off ratio of the graphene nanoribbon FET to the width of nanoribbon. (a) I_{on}/I_{off} ratios of graphene nanoribbon FET versus width of nanoribbon. (b) Measured bandgap for different width of nanoribbon. The green line is the predicted bandgap based on calculation for the zigzag nanoribbon and purple, blue, and orange lines are predicted bandgap based on calculation calculations for three types of armchair nanoribbon [58].

anymore. The immediate result of the parabolic edge of conduction and valence band is increasing the effective mass and as a result decreasing the mobility of carriers [47]. The bigger bandgap opening results in the lower mobility of carriers in graphene nanoribbon.

Applying perpendicular electric field to bilayer graphene is another method of opening bandgap which is experimentally proved. Bilayer graphene has a parabolic band structure and it has been observed that in the presence of perpendicular high electric field the Mexican hat shape bandgap of 0.2 eV or more is achievable. Figure 2.13 shows the schematic of band diagram of graphene before and after opening bandgap in mono layer of graphene by making nanoribbon and in bilayer of graphene by applying high perpendicular electric field of 1×10^7 to 3×10^7 V.cm^{-1} [59].

2.4.1.2 Carrier mobility in graphene

As mentioned earlier briefly, the mobility of carrier in graphene is dependent on many factors such as the method of production, supportive substrate, trapped ions and

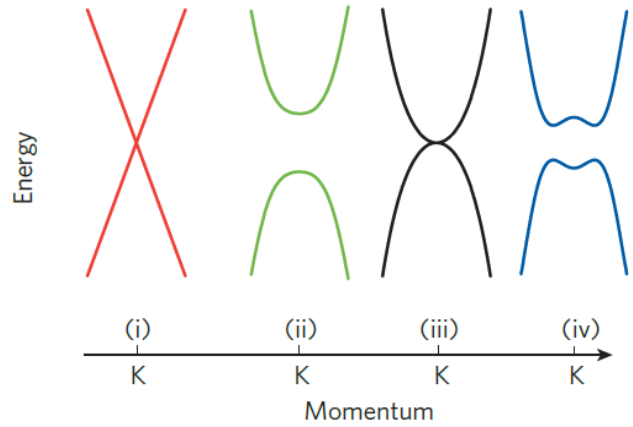

Figure 2.13. Band structure of graphene before and after opening bandgap in mono layer and bilayer graphene, (i) mono layer graphene, (ii) nanoribbons, (iii) bilayer graphene, and (iv) bilayer graphene after applying perpendicular electric field [47].

impurities in the supportive substrate, structural defects and impurities, ripples and cracks. The carrier mobility of 200,000 $cm^2\ V^{-1}.s^{-1}$ and higher at different carrier density between 2×10^{11} to 5×10^{11} has been reported for suspended graphene [60,61]. Mobility of carrier in graphene produced with mechanical exfoliation is measured to be about 10000 $cm^2\ V^{-1}.s^{-1}$ [62]. Carriers in high quality graphene grown on copper foil have shown the mobility of 4050 $V^{-1}.s^{-1}$ and it is reported that with oxygen treatment of the copper surface, growing millimeter and centimeter scale of single crystals of graphene with the mobility of the 15,000 to 30,000 $cm^2V^{-1}.s^{-1}$ at room temperature can be achieved [32,35]. Although reported values for carrier motilities in graphene are impressive but one should notice that these values are mostly reachable in the absence of bandgap and high electric field in short channel FETs. In short channel transistor presence of high electric field affects the mobility of the carriers effectively specially in conventional semiconductors such as GaAs and InGaAs. It is important to note that in presence of high electric field, carrier mobility in graphene drops but still remains above the mobility of other conventional semiconductor. The high field saturation velocity of 3.6×10^7 $cm.s^{-1}$ for

suspended graphene has been reported which is still four times of saturation velocity in the silicon and two times of GaAs in the similar field intensity [63,64].

2.4.2 Graphene for physical sensing

Graphene has found a lot of applications as physical sensors such as photo detectors, strain and temperature sensors. Since graphene has broad response to electromagnetic wave spectrum from terahertz to visible, zero bandgap and high carrier mobility at room temperature, it has attracted a lot of attention for photodetector applications during recent years. Graphene absorbs 2.293% of light in visible-to-infrared spectral per layer. The interaction of graphene increases with moving to lower frequencies and reaches to more than 25% in terahertz region [65,66]. The drawback of the graphene for photodetector application is weak absorption of light which leads to low responsivity of the graphene based photodetectors. Ultrafast graphene based photodetector has been tested experimentally using zero bandgap graphene, but responsivity of the device is just between 0.1 to 0.5 mAW^{-1} which is not enough for many practical applications [67]. However, it has been reported that graphene/Si hetrojunction which works in both photocurrent and photovoltage modes can be used for ultrasensitive photodetection, with phovoltage responsivity of 10^7 V W^{-1} and photocurrent responsivity of 435 mAW^{-1}. This photodetector can detect an object with 99.95% transparency in a 0.5 s integration time. Figure 2.14 shows the schematic, photograph and I-V curve of the device [68].

The photo-responsivity of photodetector can be improved significantly by opening bandgap in graphene and introducing electron trapping centers in it (up to 8.61AW^{-1}) [69]. Many other approaches have been introduced during recent years to improve the photo responsivity of graphene based photodetectors. One of these approaches is using

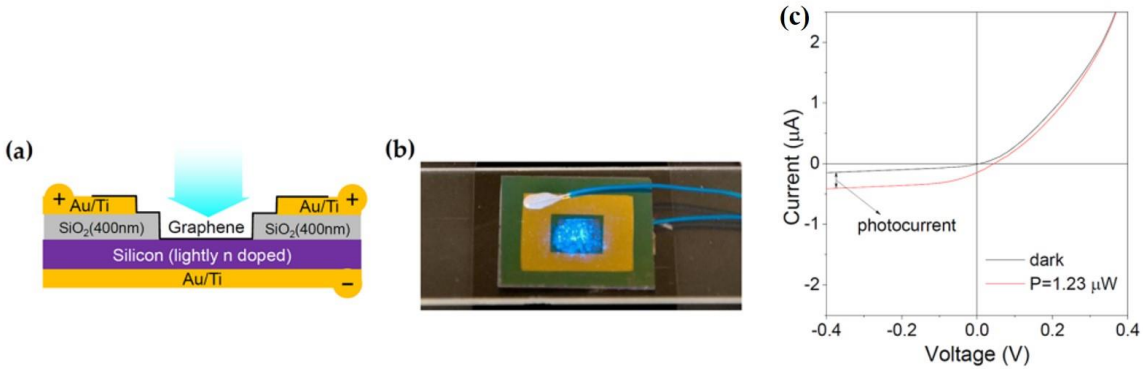

Figure 2.14. Photodetector based on graphene/Si hetrojunction. (a) The schematic of the photodetector. (B) The photo of photodetector. (c) The I-V curve of the device at 123 μW [68].

hybrid materials such as graphene–PbS quantum dot or using reduced graphene oxide (RGO) with few layers [70,71].

Graphene has also been used for sensing strain with wide range of sensing from less than 1% strain, to 50% strain with stress failure over 95%, when stretched [72-75]. Graphene based strain sensors will be discussed in detail in the chapter 6.

Thermal sensing using reduced graphene oxide as a gate of FET has been reported. Sensing temperature using RGO is based on the change of its carrier mobility with temperature variation which can be measured electrically. The schematic and the transfer characteristics of the FET at different temperature has been shown in figure 2.15. The infrared (IR) and thermal radiation generate charge carriers in the RGO network sheet and affect the transport in it [76].

2.4.3 Graphene applications in chemical sensing

Graphene has also been demonstrated for many chemical sensing applications including but not limited to gas, metallic ions and pH sensing.

It has been shown that graphene's carrier transport is sensitive to the exposed gases. Graphene based gas sensors for detecting ppm to ppb of different gasses such as NO_2, H_2,

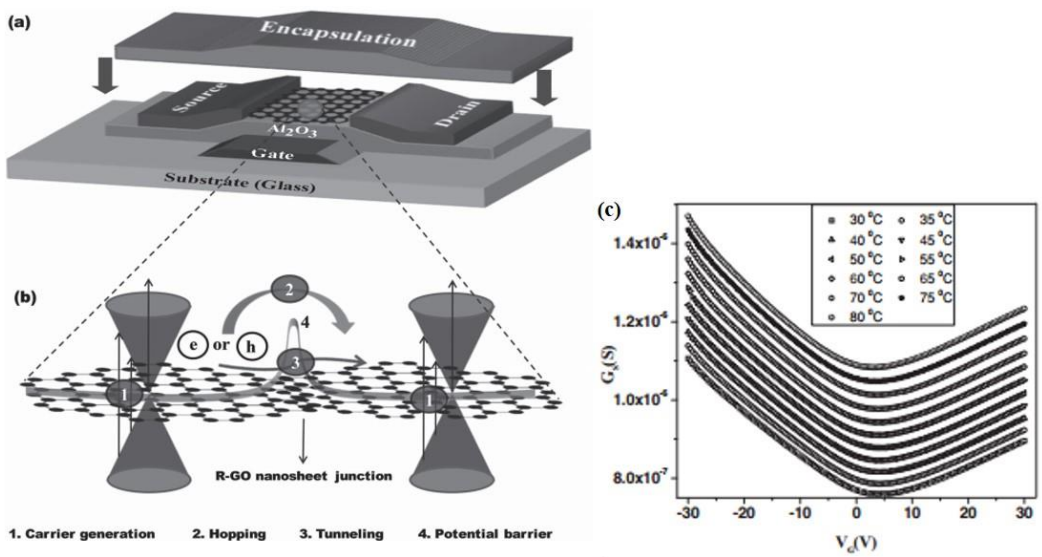

Figure 2.15. The RGO based temperature sensor. (a) The schematic of the temperature sensor based on RGO. (b) The working principle of the device. (C) The transfer characteristics of the device at different temperature [76].

CO, NO, NH_3 etc. have been reported [77,78]. A micrometer size graphene based device has been used to sense the single molecule of gas successfully. The low intrinsic noise in graphene makes it promising candidate for gas sensing at very low concentration in the surrounding medium. The result of gas sensing using such device is presented in figure 2.16 [79]. Although graphene based gas sensors can sense very low concentration

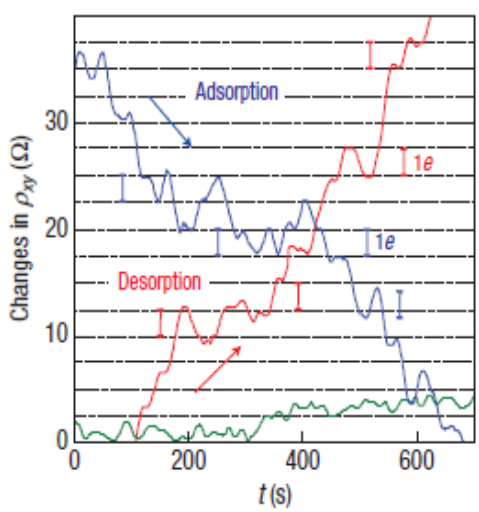

Figure 2.16. Sensing 1ppm of NO_2 using graphene. The Hall resistivity changes near the Dirac point by exposing the device to the diluted NO_2 [79].

of different gases but they are not selective. To create selectivity for graphene based gas sensors, one can functionalize the graphene surface [80,81].

Detecting various metallic ions such as Pb^{2+}, Hg^{2+}, Na^{+1}, K^{+1} using graphene based sensors have been reported. Figure 2.17 shows a schematic of a graphene based lead ion sensor using gold nanoparticles and DNAzyme-functionalized. In this graphene is decorated with gold nanoparticles. A Pb^{2+}-dependent DNAzyme, which is a double-stranded DNA is attached to gold nanoparticles. By binding Pb^{2+} ion, the enzymatic strand cleaves and the enzymatic strand and the un-thiolated portion separate and leave the thiolated fragment of the strand on AuNP. This results in the change in the electrical coupling between graphene and the charged DNAzyme complex [82].

Graphene decorated with gold nanoparticles has been used for high sensitive detection of Hg^{2+}. Gold nanoparticles provide channel for electrons to transfer to the graphene and improve the sensitivity of the device up to 6 ppm [83].

The pH sensing based on graphene has been investigated and will be discussed in

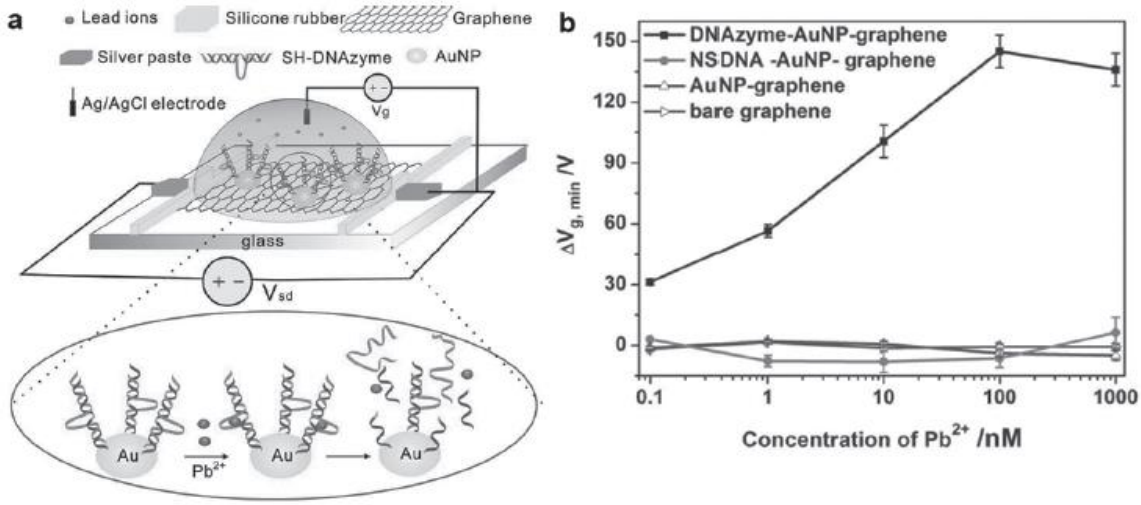

Figure 2.17. Graphene based lead sensor. (a) Schematic of Pb^{2+} sensor based on graphene transistor decorated with AuNPs and DNAzyme molecules. (b) Changes of V_{gmin} right shift versus Pb^{2+} concentrations for four different decorated devices versus [82].

detail in chapter 4.

2.4.4 Graphene applications in biology and bio-sensing

Due to interesting electrical properties of graphene discussed earlier, inherent biocompatibility, excellent mechanical properties, stretchability, flexibility and possibility of transferring graphene to many flexible substrates, it has found a lot of applications in biology life sciences and medicine (e.g. biosensors). Using graphene for sensing various proteins, deoxyribonucleic acid (DNA) and glucose has been reported [84-88]. Figure 2.18 shows the structure and fabrication process of an electrochemical immunosensor for detecting prostate cancer (PSA). In this sensor, a nanocomposite film of graphene sheets–methylene blue–chitosan (GS-MB-CS) has been used as an electrode. Nanocomposite in this sensor immobilizes the antibody of PSA. The detection limit of 13 pg mL^{-1} for PSA has been reported using this device [87]. In another work, a graphene transistor has been fabricated on Polyethylene terephthalate (PET) as a flexible substrate and has been used for sensing glucose. To sense glucose graphene was functionalized

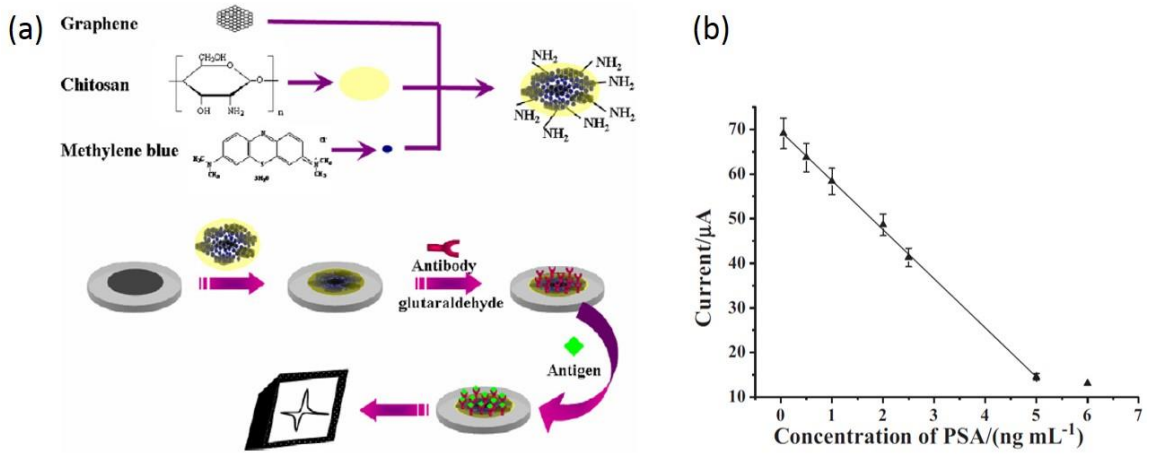

Figure 2.18. PSA electrochemical immunosensor. (a) Fabrication flow of the immunosensor. (b) Plot of change in the current of the immunosensor versus changes in the concentrations of PSA [87].

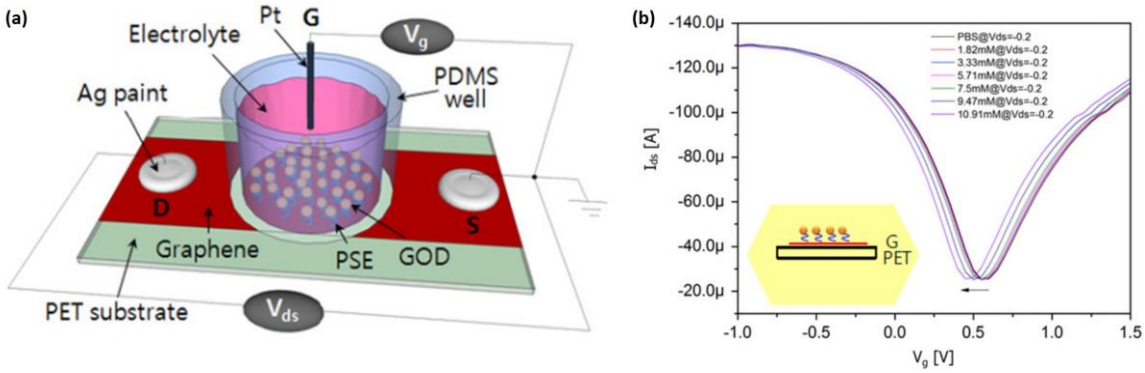

Figure 2.19. Graphene transistor based glucose sensor. (a) Schematic of the graphene transistor based glucose sensor. (b) Shift in the Dirac point toward the lower V_G by increasing the concentration of glucose [88].

with linker molecules to immobilize catalytic enzyme. The sensitivity of 3.3–10.9 mM has been reported for this sensor (see figure 2.19) [88]. Graphene also has been used as a conductive scaffold for neuron cell growth and stimulation, stem cells differentiation and electrical recording of various type of cells [89-91].

CHAPTER 3

Utilization of graphene electrode in transparent micro-well arrays for high throughput cell trapping and lysis

Cell trapping and lysis play important role in fundamental biological study of cells and biosensing from the analysis of cell lysates. Due to high ionic strength of biological media performing stable and reliable electrical experiment in the presence of electrochemically reactive electrodes is challenging. Electrochemical reaction changes the physical and chemical properties of the biological environment and damages surrounding cells and organs. In this chapter utilization of the graphene electrode as an electrochemically stable electrode for dielectrophoretic cell trapping and lysis is discussed. To prove the concept, cell trapping and lysis using a micro-well array sandwiched between two electrodes, one graphene electrode and the other, ITO are performed.

In this chapter, first the motivation behind of this work is presented and theoretical background of dielectrophoretic cell trapping is discussed. Then the device fabrication

process is explained and the result of electrochemical stability study of the graphene electrode is discussed. Finally the proof of concept by stable functioning of combination of the graphene and ITO electrodes in a microfluidic device for trapping cells using DEP and lysis the cells under high DC electric field is presented.

3.1 Motivation and background

Cell trapping and lysis play an important role in fundamental biological study of cells, through chemical cytometry and in the area of biosensing by analyzing cell lysates [92,93]. Many different methods have been used for trapping of cells based on physical, magnetic, optical and electrical approaches [94-98]. Of all these methods, using electric fields has particular advantages due to its simplicity, selectivity and the prospect of miniaturization into a small device [99-101]. For cell lysis which is a process to rupture cell membrane and release its cellular contents, there are similarly plenty of methods based on chemical, thermal and mechanical approaches, but they are unable to perform cell lysis in a selective manner where only certain cell-types can be targeted [102-104]. Moreover, existing devices lack the portability that is afforded by miniaturization. Using electric field for cell lysis is beneficial due to the simplicity of the apparatus, high controllability from selective trapping of cells, and the possibility of integration on a single miniature chip [98]. Even though the concept of cell trapping and lysis, using electric fields has already been very well established, there are still many aspects of such a platform that needs further investigation. One of these aspects is the study of the electrode material used. An ideal electrode must have the features of high conductivity to minimize resistive temperature increase that can damage the cells, biocompatibility, electrochemical inertness to avoid unwanted faradaic reaction, compatibility with

standard microfabrication process and preferably transparency to allow optical monitoring. Gold, platinum and tungsten are popular choices for the electrodes because of their good conductivity and compatibility with standard fabrication process, but they tend to sacrifice either the optical transparency or the electrochemical stability of the device [100,105,106]. Some others have used indium tin oxide (ITO) as the transparent and conductive electrode to facilitate optical monitoring during experiment [107]. But ITO is toxic and is not chemically inert as it undergoes electrochemical reduction in the most cell mediums [108,109]. Moreover, the reduction at ITO electrode results in large faradaic current that consequently changes the physical and chemical properties of the cell medium [110]. In addition, the process also severely degrades the electrical and optical properties of the electrode. Here we investigate the potential application of the graphene as the electrode in electrochemical reactive biological environment as an electrochemically stable electrode. Graphene is known to be fairly electrochemically inert with good overall optical transparency [111,112]. While graphene would have been a good choice for both electrodes in our device, it is however sufficient to replace a cathode ITO electrode and ITO can still serve as the other electrode, as long as positive voltage is applied to that with respect to the graphene electrode during electrical lysis. We implemented our microfluidic device with both graphene and ITO electrodes in order to confirm this phenomenon; for practical device realization one could switch to an all-graphene electrode configuration.

The choice of graphene is clear because it is among the most conductive known materials at room temperature, it is also mechanically strong, biocompatible and exhibits excellent optical transparency in the visible spectrum [113]. These characteristics plus the

compatibility with standard microfabrication process makes it a promising candidate for bioelectronics applications.

Here first a microfluidic device consisting of microwell arrays inside a cavity, sandwiched between two ITO electrodes for cell trapping using DEP and lysing trapped cells by applying DC field is introduced. The impedance monitoring was performed in the range of frequencies between 100 Hz to 10 KHz at to count the number of the filled wells with the cells using this device as it has been shown in figure 3.1. But we observed that in this device due to electrochemical reaction which occurs gradually during cell lysis at high DC electric field, after few uses one of the electrodes oxidizes and the other one reduces and turns to brownish or blackish.

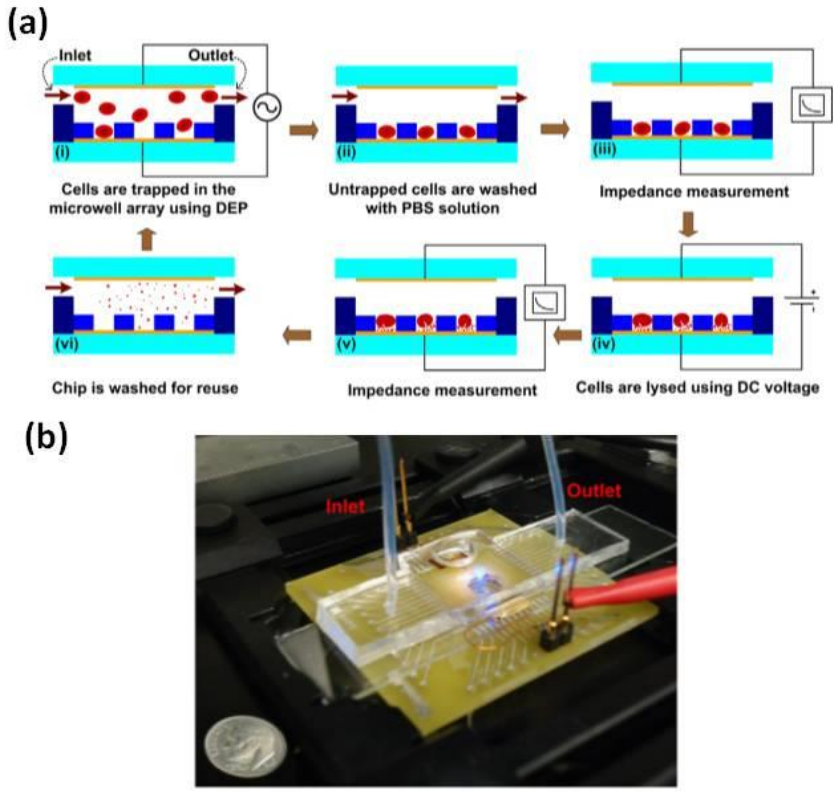

Figure 3.1. (a) All ITO electrode experimental steps for cell trapping, lysis and impedance measurements. (b) Photo of the chip consisting of the microwell array, inlet, outlet and electronic connections; device placed next to a dime (10 cent) US coin.

To overcome this drawback, in a similar device one of the electrodes is replaced with graphene to minimize the electrochemical reaction at the cell-electrode interface at high DC electric field. Human red blood cells (RBC) were used for this experiments for proof of concept. They were introduced into the device through an inlet, and then an alternative current voltage (AC) signal at 2.5V and 120 KHz frequency was applied between top and bottom electrode to trap the cells inside the micro-wells. After trapping, excess cells were washed out by flowing the Dulbecco's phosphate buffer saline (DPBS) solution. The trapped cells were then subjected to a 3 V direct current (DC) voltage between the top and the bottom electrode to perform electrically cell lysis (see figure 3.2). Our result shows high efficiency of cell trapping and lysis, discussed in details in continue. After lysis, the device is cleaned by flowing deionized (DI) water. No change in the

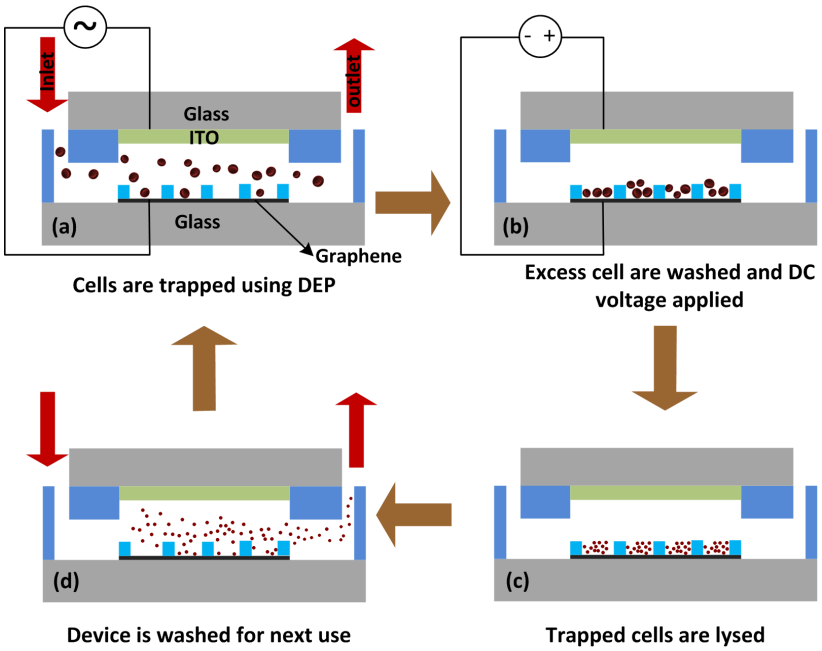

Figure 3.2. Experimental process flow for cell trapping and lysis. (a) Cells are introduced in the microfluidic device and AC voltage is applied between top and bottom electrodes; (b) After washing untrapped cells, DC voltage is applied between electrodes; (c) Cells are lysed and contents are released inside of each micro-well; (d) Finally device is washed and cleaned for next use. Red blood cells were used for this experiment.

transparency of the electrodes was observed enabling re-use of the device for next run. This is in contrast to the behavior when both electrodes are made from ITO and the optical transparency decreases considerably with each use.

The principle for cell trapping reported in this work is based on dielectrophoresis (DEP) which is the movement of dielectric particles in a non-uniform electric field (Pohl, 1951). Solid spherical particles in dielectric medium and in the presence of non-uniform electric field experience a force, F_{DEP}, which can be calculated as follows [107]:

$$F_{DEP} = 2\pi\varepsilon_m a^3 Re[K(2\pi f)]\nabla E^2 \quad (3.1)$$

Where ε_m is the electrical permittivity of the external medium, a is the particle radius, f is the frequency of the electric field and E is the electric field. The $K(2\pi f)$ is known as Clausius-Mossotti factor and is defined as

$$K(2\pi f) = \frac{\varepsilon_p^* - \varepsilon_m^*}{\varepsilon_p^* + 2\varepsilon_m^*} \quad (3.2)$$

Where ε_p^* is the complex electrical permittivity of particle and ε_m^* is the complex electrical permittivity of the dielectric medium. Since the electrical permittivity depends on the frequency, the Clausius-Mossotti factor is also frequency dependent. When the real part of $K(2\pi f)$ is greater than zero, the particle moves towards the maximum of the electric field in a process known as positive dielectrophoresis, and when the real part of $K(2\pi f)$is less than zero, particle moves towards the minimum of the electric field in a process known as negative dielectrophoresis. The frequency at which the DEP force switches between positive DEP and negative DEP is called a cross-over frequency. Cells could not be simply considered as spherical solid particles due to their membrane which creates a double layer capacitance [98]. This results in the existence of two crossover

frequencies for the cells, the values of which depend on the electrical and physical properties of the cells and their medium. Due to dependency on the conductivity and electrical permittivity of the cell membrane, internal cell media (cytoplasm) and external media, different cells and even cells of the same type but in different medium having different electrical properties, exhibit different crossover frequencies [112].

3.2 Experimental Approach

3.2.1 Device fabrication

The fabrication process flow of microfluidic device for cell trapping and lysis is shown in Fig. 3.3. To fabricate all ITO electrode based microfluidic device for single cell trapping and lysis, ITO film with 200 nm thickness was deposited on a 3” glass substrate using DC magnetron sputtering (NSC 3000) which serves as transparent electrodes. The thickness of ITO thin film was measured by a surface profilometer (Veeco Dektak 6M Stylus). Using standard lithography with positive photoresist (Rohm & Haas SPR220 series) and wet etching (HCl: H_2O: HNO_3 = 4:2:1), bottom and top electrodes were patterned. Electrodes were then annealed in nitrogen ambient at 300 ºC for one hour to improve their electrical and optical properties. After annealing, the optical transparency of the ITO electrodes in the visible region increased considerably. The resistivity of ITO films was measured using a four point probe (Miller FPP-5000) and was found to be about 6.3×10^{-3} Ω.cm. The negative photoresist (SU8 2005, MicroChem Co.) was then spin coated onto the bottom electrode to form a 7 μm thick layer. The SU8 photoresist was soft baked and exposed to UV light through photo-mask to form the microwells. After developing the photoresist, microwells that were 9 μm × 9 μm in area and 7 μm in depth were formed. The size of the wells was designed to be close to the diameter of the

red blood cells to ensure that only a single cell would fit inside each well. To create the microfluidic channel and the cavity, first a SU8 master mold (100 µm in thickness) was prepared on a silicon wafer and then covered with a PDMS, base already was mixed with a curing agent in ratio at 10:1. The entire assembly then placed in a vacuum chamber to remove bubbles and cured at 80 ºC for 2 hours. After curing, the PDMS was separated from the master SU8 mold and placed in a reactive ion etcher (CS1701F RIE) for oxygen plasma treatment at 40 W of power for 30 seconds. The oxygen plasma treatment generates a hydrophilic surface on PDMS enables it to bond to the glass substrate. As the final step in device fabrication, the top electrode, bottom electrode and PDMS were aligned and bonded together. The total distance between bottom and top electrodes was 100 µm and the width of the inlet/outlet micro-channels was 200 µm.

To fabricate graphene based microfluidic device for cell trapping and lysis, CVD grown graphene on nickel (Graphene Supermarket Inc.) with three to ten layers of graphene was transferred on a standard glass substrate. To transfer graphene, PMMA (Poly methyl methacrylate) was spin coated on the graphene and then placed in a nickel etchant (Ferric chloride $FeCl_3$ 0.06 molar) to etch away the nickel substrate and release graphene on PMMA. In the next step, graphene on PMMA is transferred on the glass and placed in the solvent to remove the PMMA. Finally, transferred graphene is rinsed with DI water and blow-air dried. To make electrical connections to graphene, titanium and gold with 10 nm and 200 nm thicknesses respectively were deposited using DC magnetron sputtering (NSC 3000). Titanium and gold were patterned using standard photolithography and wet etching to form connections. The process of fabricating the microwells in this device is the same as mentioned earlier. Here the microwells were

realized with 20 μm × 20 μm area and 7 μm depth. The same fabrication process of microfluidic explained earlier, was followed to realize a microfluidic channels in this device.

The morphology and roughness of the graphene was studied using a Zeiss EVO scanning electron microscopy and Asylum Research MFP-3D-Bio Atomic Force Microscope. The Raman shift was investigated with Raman spectrometer (Jasco NRS-3100) with a 785 nm laser excitation.

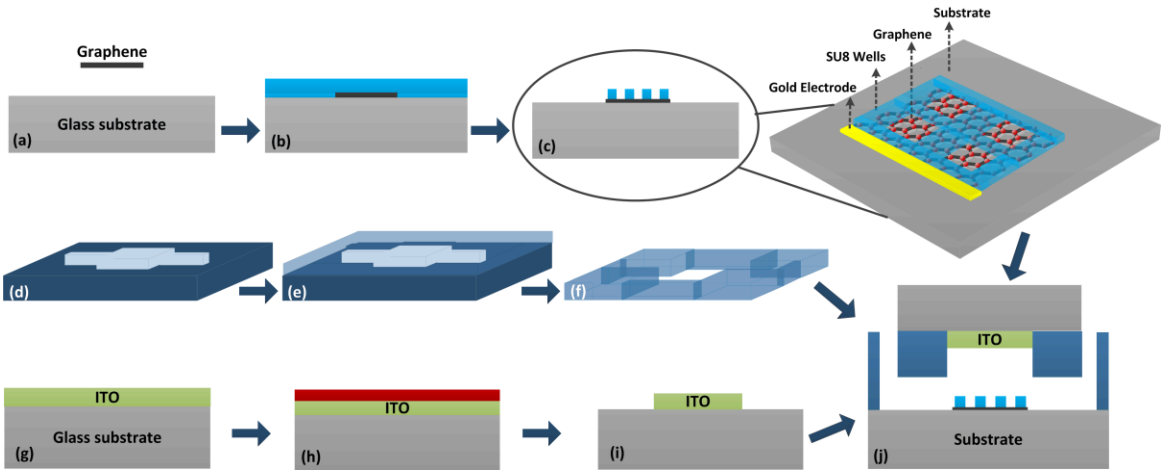

Figure 3.3. Fabrication process flow of the microfluidic device. (a) Graphene is transferred on the glass substrate and Ti/Au contact is made; (b) SU8 is spin coated on the graphene; (c) SU8 is patterned using standard photolithography process and micro-well arrays are formed on the top of the graphene; (d) To make the microfluidic channel and cavity, SU8 mold is fabricated; (e) PDMS is poured on the mold; (f) PDMS is cured and separated from mold; (g) ITO is deposited on the glass substrate; (h) SPR photoresist is spin coated at the top of the ITO film; (i) ITO electrode is patterned using standard lithography and Ti/Au contact is made; (j) Top electrode, bottom electrode and PDMS are bonded together.

3.2.2 Blood sample preparation

Live human red blood cells were extracted from whole blood (Bioreclamation LLC, NY, USA). To separate red blood cells, blood was centrifuged with 1500 rpm for 3 min and cells were separated from blood plasma. Next, cells were washed with Dulbecco's

phosphate-buffered saline, DPBS, (Potassium Chloride (KCl) 0.2 gL^{-1}, Potassium Phosphate monobasic (KH_2PO_4) 0.2 gL^{-1}, Sodium Chloride (NaCl) 8 gL^{-1}, Sodium Phosphate dibasic (Na_2HPO_4-$7H_2O$) 2.16 gL^{-1}, water)(Dulbecco and Vogt 1954). To perform the experiment with all ITO based electrode device, cells were suspended in DPBS to achieve the final concentration of 10^7 cells.ml^{-1}. For cell trapping and lysis using graphene based microfluidic device, cells were incubated with Calcein AM fluorescent dye for an hour. Next they were washed with DPBS and suspended in it to achieve the final concentration of 10^6 cells.ml^{-1}. Experiment was monitored using a fluorescent microscope (Zeiss Axiovert 40 CFL) and a standard optical microscope (Micromaster R from Fisher Scientific K0106-0302-001).

3.3 Material characterization

CVD grown graphene on the Ni film with the thickness of 300 nm, transferred on the glass and Si substrate for future characterization. The atomic force microscopy was used to study the thickness and topology of the graphene. Figure 3.4 shows the atomic force microscopy (AFM) image of the transferred multilayer graphene on silicon substrate. The transfer process results in wrinkles, which creates surface roughness between 2 nm to

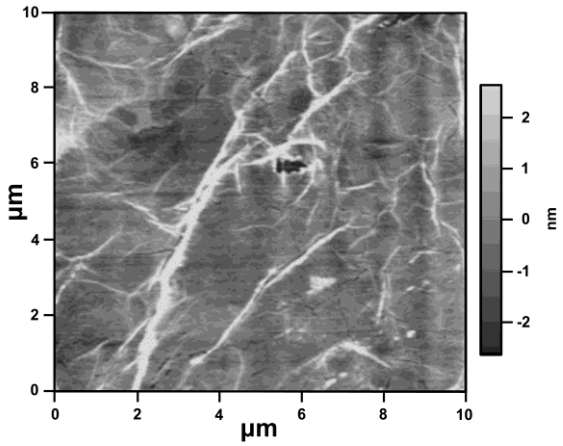

Figure 3.4. AFM image of graphene.

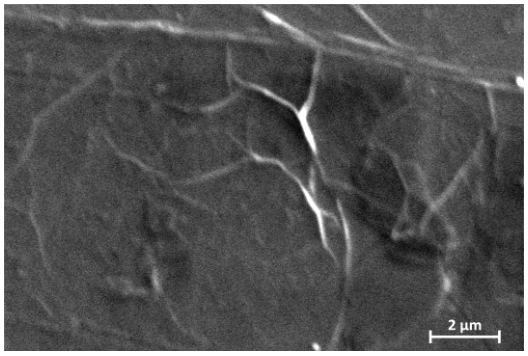

Figure 3.5. Scanning electron microscopy (SEM) image of graphene.

4 nm. Figure 3.5 shows the surface morphology of this multilayer graphene on glass using scanning electron microscopy (SEM). As it shows numbers of folds and wrinkles are visible. To study the number of the carbon layers in graphene electrode, Raman spectroscopy was performed. Result shows the presence of a G peak at 1580 cm^{-1} and a 2D peak at 2600 cm^{-1} (See Figure 3.6 for results). Optical microscopy image of the transferred graphene on the glass substrate reveals numbers of flakes in graphene layer. Spectroscopy of the flakes shows a weaker 2D band and a stronger G band which reveals more number of layers (5-10 layers) in this area, while other part shows almost same intensity of the 2D and G band peaks and therefore fewer layers (3-4 layers) in these

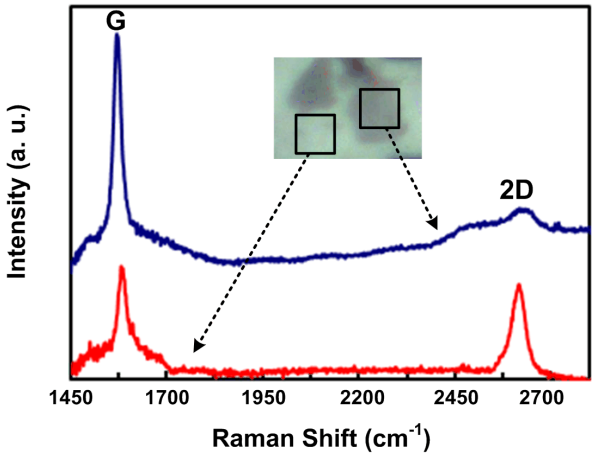

Figure 3.6. Raman shift of the graphene transferred on the glass. The inset is the optical photo of the graphene layer and it shows the existence of the flakes which consist of more than one layers of graphene.

parts.

3.4 Cell trapping, lysis and impedance monitoring using all ITO electrode microfluidic device

Human red blood cells with a final concentration of 10^7 cells.mL^{-1} were introduced into the microfluidic device with 20 μL.min^{-1} flow rate. The conductivity of the external medium was 0.01 S.m^{-1}. To immobilize the cells using DEP, AC voltage of 80 KHz with 1.5 V amplitude was applied between the top and bottom electrodes. The non-uniform electric field distribution between the top and bottom electrodes caused the cells to experience positive dielectrophoresis at 80 KHz frequency. Once a desired percentage of cells were trapped, the untrapped cells are washed with a continuous flow of PBS solution. As a first experiment we applied AC voltage for 23 seconds and observed that 30±2 % of wells remained filled with cells after a PBS wash. Subsequently the impedance was measured at 100 Hz, 1 KHz and 10 KHz using an LCR meter. We observed that the application of AC voltage for 54 and 100 seconds resulted in 60±2 % and 90±2 % of the wells being filled with cells respectively. To induce lysis of the trapped cells, 2V DC voltage was applied for 6 seconds between the top and bottom electrodes and the impedance was monitored at every step before lysis and after it. The optical images of micro-wells after introducing cells to the microfluidic device are shown in Figure 3.7. Figure 3.7 (a) shows the device after introducing cells and before the application of the AC voltage. It shows that even before the application of DEP force some cells were already settled in the microwells as a result of gravity. To understand the contribution of gravitational force, the setup was maintained for 10 minutes before applying the DEP bias.

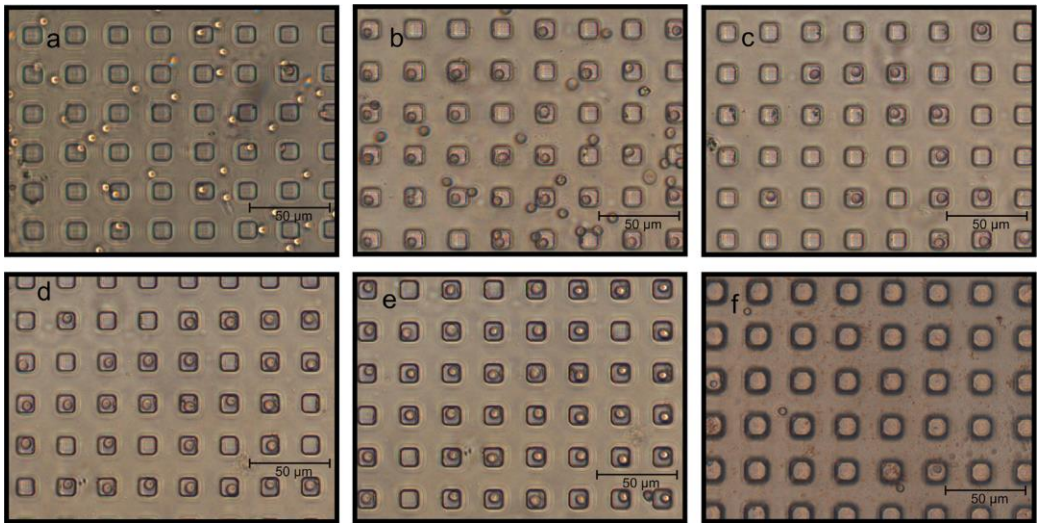

Figure 3.7. Optical microscopy images of microwell arrays after introducing the cells into the microfluidic channel. (a) Before DEP. (b) After DEP, before washing. (c) 30% of wells are filled; (d) 60% of wells are filled. (e) 90% of wells are filled. (f) Microwells after cell lysis.

The untrapped cells were washed by flowing PBS through the channel. About 4% of the microwells were filled with cells due to gravity. Figure 3.7 (b) shows the wells after the DEP capture process, indicating that cells were dispersed both inside and outside the microwells. After this step, the voltage was turned off and cells outside the wells are washed and removed using the PBS solution rinse, before the impedance measurement. Figure 3.7 (c) shows the wells after removing the untrapped cells. In the first step, after applying AC electric field, 30% of the wells were filled with cells. Each well contained a single cell since the size of the wells closely matched the size of cells. Figure 3.7 (d) and 3.7 (e) show the image of the wells when 60% and 90% of the wells were filled with cells by applying AC electric field. The results of impedance measurement from wells that were about 4%, 30%, 60%, 90% occupied with cells at 100 Hz, 1 KHz and 10 KHz are shown in Figure 3.8. The impedance values decreased considerably as the fraction of filled micro-wells increased. To investigate changes in impedance due to presence of cells inside wells, the electric field and AC current distribution were simulated using

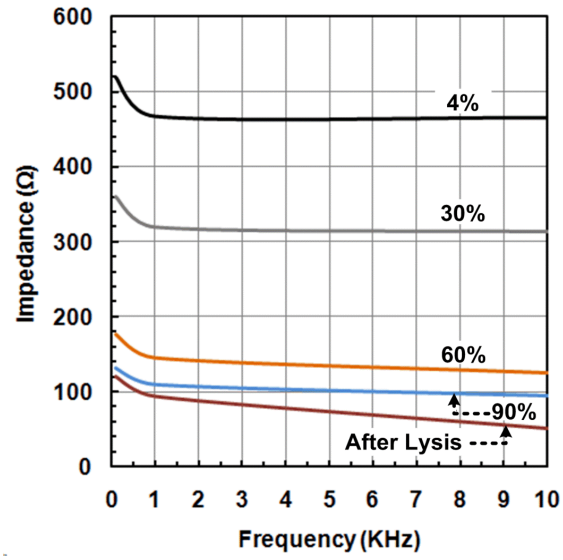

Figure 3.8.A plot of impedance measurements versus frequency for different percentage of filled wells with cells and after lysis.

electromagnetic wave simulation software (CST 2011 microwave studio) at 1 KHz. In this simulation, cavity and some wells were considered filled with cells and others filled with PBS solution. The red blood cells were considered as a multi-shell particle consisting of two shells, with 6.992µm inner shell diameter and 7µm outer shell diameter. The distance between the top and bottom electrodes was set to 100 µm. The simulated electric current is shown in Fig. 3.9 (a). As seen in this figure, when wells were filled with cells the current density was found to increase in the microwells. Increasing current density translates into reduced impedance between the top and bottom electrodes, which is in agreement with experimental observations. Figure 3.9 (b) shows the electric field simulation result. It shows that electric field at the edge of wells are higher which results in trapping of the cells inside of wells. After the DEP process, the trapped cells were lysed by the application of 2V DC voltage between the top and bottom electrodes for 10 seconds. Figure 3.7 (f) shows the optical image of the wells after cell lysis. After the application of DC voltage, 87±3% of the cells were lysed. The bilayer cell membrane

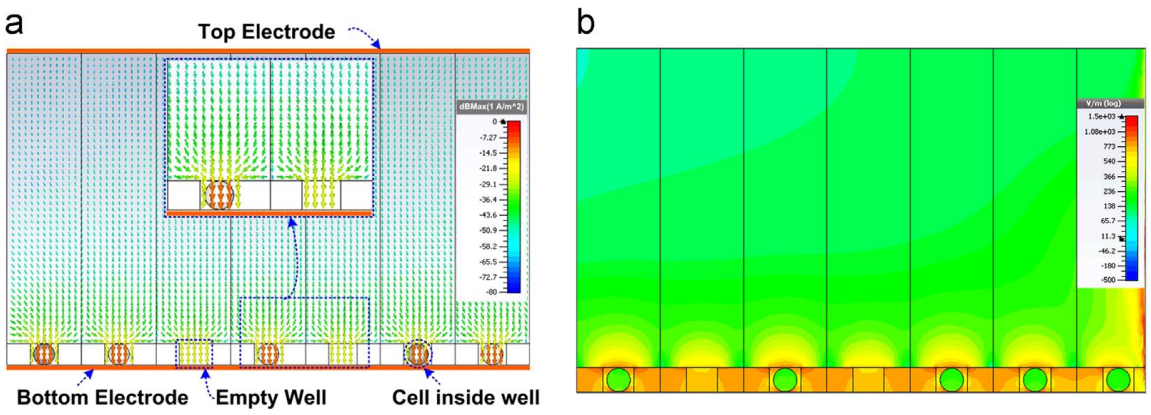

Figure 3.9. (a) Simulated electric current distribution, and (b) electric field distribution at 1 KHz frequency. Simulation was performed considering the presence of PBS in microwells and the cavity. Wells occupied by cells resulted in increase in current density increase compared to empty microwells.

has about -10 mV potential at the rest condition. When an external electric field is applied to the cells it induces additional potential in the cell membrane which makes it permeable to the external medium. This permeability is dependent on the strength and duration of the applied electric field. With the increase in electric field, cell membrane becomes more permeable to the external medium causing cell lysis [124]. After lysis, the impedance was measured between the electrodes and recorded. As indicated in figure 3.8, the measured impedance was significantly decreased after lysis of trapped cells. This decrease ranged between ~ 20% for 100 Hz to 1 KHz frequency to ~ 5% between the range of 1 KHz to 10 KHz. The reason for this variation is that the cell and medium electrical parameters (conductivity and permittivity) are frequency dependent. Figure 3.10 shows the impedance values before lysis versus the percentage of filled wells at three different frequencies, 0.1, 1 and 10 KHz. The impedance values decreased greatly (~ 5.5 ohms per %) for 4% to 60% of filled wells, however it varied slowly (< 0.67 ohms per % of filled well) for 60% to 90% of filled wells.

3.5 Equivalent electrical model

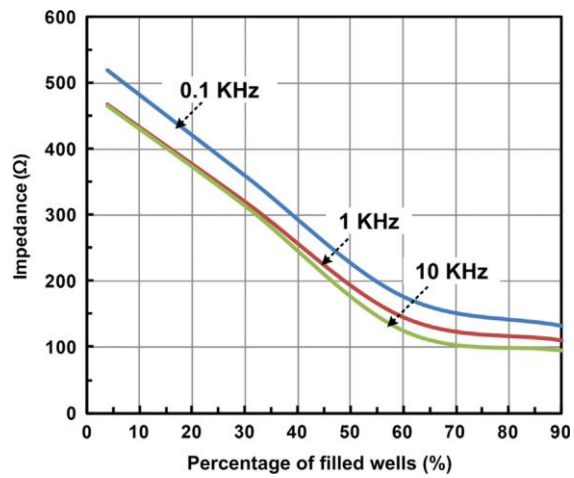

Figure 3.10. Plot of measured impedance versus percentage of filled microwells for three different frequencies.

To understand the behavior of the impedance change with respect to percentage of filled wells, an equivalent electrical circuit model was developed (Fig. 3.11). In this model, a single cell is modeled as a double layer sphere with cell membrane capacitance (C_m) and resistance (R_m) in parallel, and the internal cell media (cytoplasm) resistance (R_i) in series [114-116]. A single microwell filled with PBS is modeled as capacitance (C_w) and resistance (R_w) in parallel. Similarly, microfluidic cavity above the microwell array which is filled with a PBS solution is modeled with parallel capacitance (C_c) and resistance (R_c). The electrode-PBS interface is modeled using the double layer capacitance (C_{p1}, C_{p2}). The red blood cell electrical parameters including cell membrane resistivity and capacitance, internal conductivity of the cells for calculating the values of components in the model are extracted from published articles [113,117-121]. The electrode polarization capacitance is dependent on the electrode and electrolyte materials [122]. The presented table in figure 3.11 (c) shows the final values for the equivalent circuit model. These values are fitted to the model to closely match the experimental data. The impedance variation of the circuit model exhibits a similar trend as in the

experimental data. In both model and measurement, as the percentage of filled wells increases, the impedance decreases. The rate of change of impedance reduces for the case of greater than 60% of filled wells. There are some differences between the model and experimental results mostly at higher percentage of filled wells due to the limitation on defining the exact values for some parameters such as dielectric constant of the materials, cell membrane capacitances or cell conductivity. In addition, the dimension of the cells varies in practices which give rise to observed deviations. In practical applications this model can be used to extract the number of filled wells directly after DEP, from

a

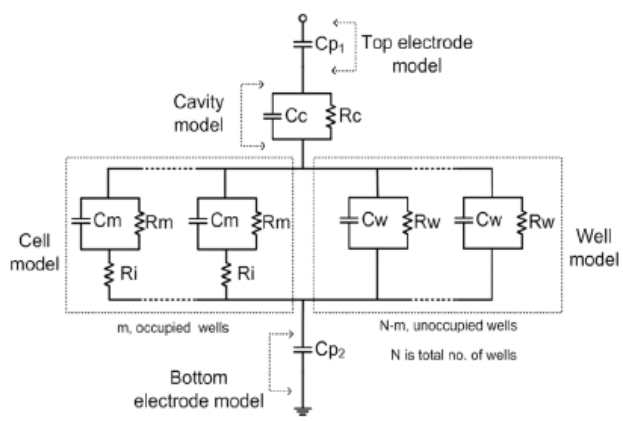

b

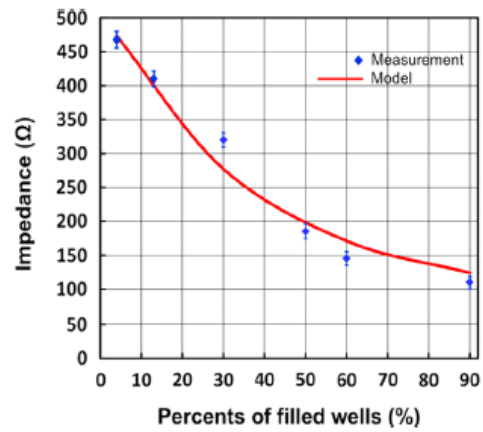

c

Component	Values
C_{P1} (μF)	80
C_C (pF.cm^{-2})	1.96×10^6
R_C (Ω)	1.03×10^3
C_m (pF)	1.2
R_m (Ω)	4×10^5
R_i (Ω)	3×10^5
C_W (pF)	12
R_W (Ω)	1.4×10^7
C_{P2}(μF)	6.6

Figure 3.11. (a) Equivalent electrical circuit model of the platform. The cells are modeled as the spherical double–shell particles with the capacitance of C_m (membrane capacitance). (b) Comparison of impedance for experiment and model at 1 KHz indicating close match. (c) Values of the circuit components used in the model at frequency of 1 KHz.

measured impedance, eliminating the need for optical monitoring.

While this value may deviate from the actual number of cells, it is sufficient where the goal is to maximize trapping (evident by an observed decrease in impedance) before final cell lysis. The impedance measurement could direct the controller to increase the strength or the time of the dielectrophoretic AC field in order to increase the percentage of filled microwells with trapped cells. Once a maximum is reached as will be evident by a minimum in AC impedance, a DC electric field will be used to perform lysis as mentioned. Monitoring lysis using impedance measurement is quite straightforward. Impedance values following lysis are significantly lower (5X) when 90% of the wells are filled (Figure 3.6). Thus, the proposed lab-on-chip is ideal for trapping cells, and extraction of cellular materials using lysis, all using electric fields that can be realized in a compact manner. Moreover, impedance monitoring provides an effective substitute for optical monitoring of cell trapping and lysis. A single AA battery can supply the operational voltage and power requirement of the system. This enables a truly compact and portable solution for diverse applications in medical diagnostics where cell trapping and lysis are essential.

3.6 Electrochemical stability study of the device electrodes

Next, we report on the electrochemical stability of electrodes in this device. As discussed earlier, the device consists of two electrodes and a buffer solution between them, which resembles an electrochemical cell. When electrodes are electrochemically active, as the result of applying DC voltage, a redox reaction can take place. ITO is not electrochemically inert and therefore when it is used as a cathode, it will undergo reduction in PBS solution (a standard isotonic media for suspending cells). This causes

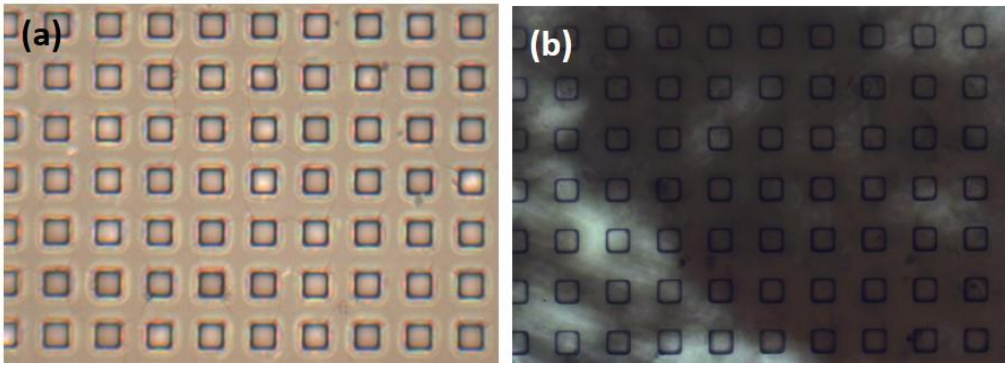

Figure 3.12. Microwell array fabricated on ITO electrodes in all ITO microfluidic device. (a) Right after fabrication and before use. (b) After several times performing cell lysis. Due to reduction of ITO the electrode stoichiometry is change and it turns to black.

a change in stoichiometry of the ITO film, which results in considerable reduction in its optical transparency as it has been shown in figure 3.12 and also a change in its electrical properties. So, we replaced the cathode electrode with graphene to prevent electrochemical electrode degradation.

To investigate the combination of ITO and graphene electrodes electrochemical stability, two sets of devices were designed with two electrodes separated from each other using a 100 µm thick PDMS spacer as it has been shown in figure 3.13. The distance between two electrodes was designed to be the same as the distance between electrodes in microfluidic device for dielectrophoretic cell trapping and lysis. In one device, both electrodes are made of ITO and in another, one electrode is made of ITO and other is made of the multilayer graphene. Cavity between two electrodes is filled with DPBS. Different magnitudes of DC voltages were applied between two electrodes in both devices for various time periods. Then the transparency of the electrode was measured in the visible region to reveal if the redox reaction took place and it caused any change in the transparency of the ITO electrode. Results are shown in Fig. 3.14. When both electrodes are made from ITO, the cathode undergoes electrochemical reduction causing

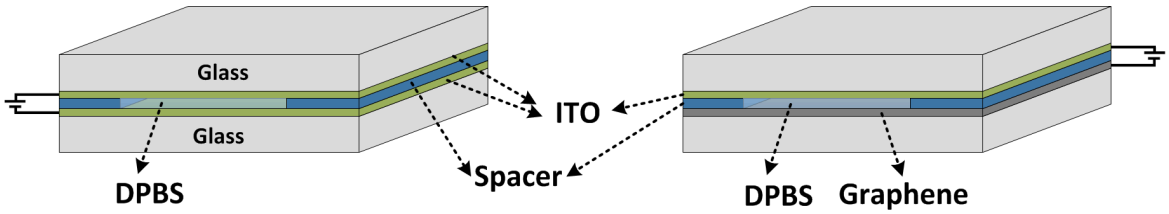

Figure 3.13. Device schematic for the testing of electrochemical stability of the electrodes.

its transparency to change (the color of the ITO film changes to dark brown and further black with time). At the left side is a schematic of the device with two ITO electrodes and at the right hand is the device schematic with a graphene electrode replaced with the ITO cathode. The change in the transparency of the film depends on the magnitude and the duration of the applied voltage. Increasing the magnitude of the applied voltage increases the rate of reaction kinetics, thereby; decreasing the transparency of the electrode for the same period of time as it is shown in figure 3.14. When cathode electrode is replaced with graphene, redox reaction is mostly prevented and no change in the transparency of electrodes is observed after applying voltage for a long period of time, showing that graphene is more stable and inert and can be suitable substitute for ITO to prevent redox reaction. Our results are in the agreement with the electrochemical potential measurement done for the of the pH solution in contact with graphene by Ang et al. which shows the linear relation between the heights of anodic/cathodic peak and the scan rate of the applied potential indicating a non-faradic origin of these peaks. This means electrochemical reaction does not occur between the graphene and electrolyte [123].

3.7 Cell trapping and lysis using graphene based electrode microfluidic device

To investigate the electric field distribution inside the microwell array, the device with graphene and ITO electrodes was simulated using electromagnetic simulation software (CST microwave studio®).

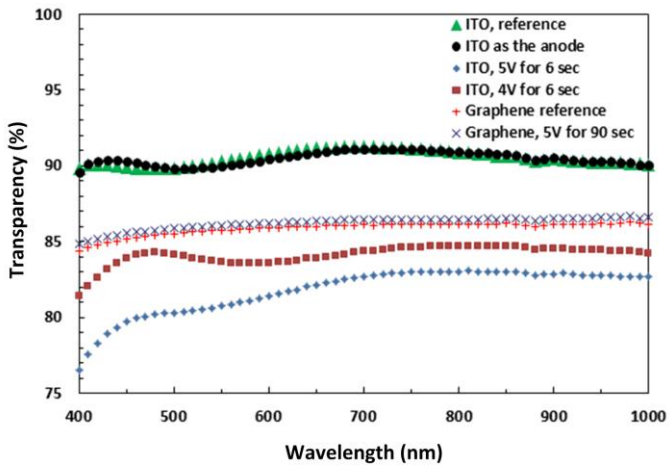

Figure 3.14. Plot of the optical transparency of the electrode after applying deferent voltages between top and bottom electrodes, versus wavelength.

In this simulation, the cavity and wells were considered filled with DPBS solution with electrical conductivity of 0.028 $S.m^{-1}$, wells were modeled made from SU8 of size 20µm × 20µm in area and 7 µm in height. The distance between the electrodes was considered 100 µm. The simulation was performed at 120 KHz frequency. The simulated electric field distribution in one single microwell is shown in Figure 3.15 from the side and the top view. As shown, the electric field is stronger at the edge of the wells and decreases with increasing distance from the well which causes cells to be trapped inside the microwells as a result of positive DEP.

The functionality and efficiency of the proposed microfluidic device for cell trapping and lysis was tested. In the first step, cells with the concentration of 10^6 $cells.ml^{-1}$ were introduced to the microfluidic channel through inlet with flow rate of 20 µL. min^{-1}. Some cells get trapped in the microwells as a result of gravitational force. About 28% of the wells were filled up due to gravitational force in 10 minutes. In the next step, device was washed with DPBS, cells suspension introduced to the device and DEP was performed using AC voltage of 2.5V magnitude and 120 KHz frequency. The selection

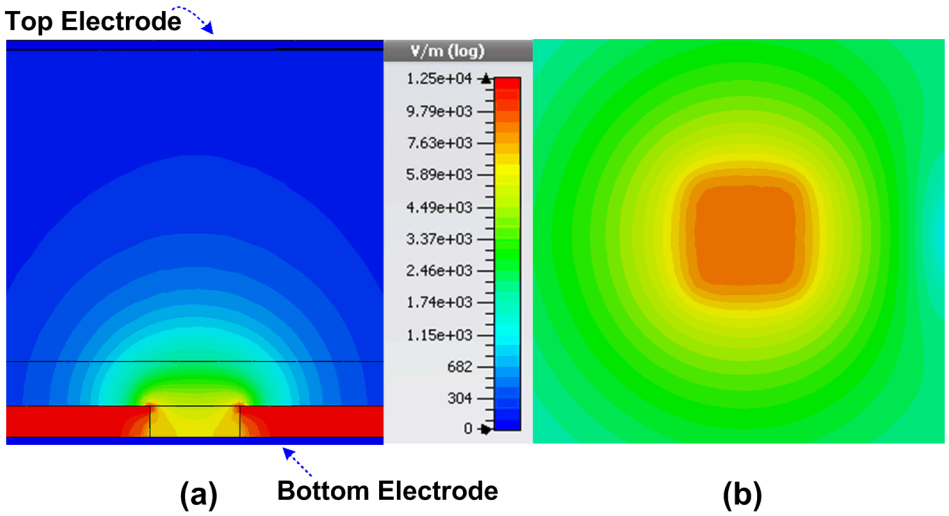

Figure 3.15. Simulated electric field distribution in a single micro-well. (a) Side view. (b) Top view, 15 µm above the bottom of the well.

of the frequency was based on several experimental iterations. Then voltage was turned off and the untrapped cells were washed out with continuous flow of DPBS through the microfluidic channel. Figure 3.16 (a) and 3.16 (b) shows the optical and the fluorescent photo of the RBCs trapped in the microwells, respectively. As it has been shown, the cells were trapped in the micro-wells with very high efficiency. In the next step, direct current voltage (DC) is applied between top and bottom electrode to lyse the cells. In our experiment, we applied a DC signal of magnitude 3 V for 8 seconds to lyse the trapped cells. Figure 3.16 (c) shows after cells were lysed completely; there was no change in the overall optical transparency of the electrodes indicating inherent stability of the electrode for multiple uses. We repeated our experiments four times for different batches of red blood cells and our results showed about 98.4% of wells were filled with cells after trapping, and 100% of the trapped cells were lysed after applying DC voltage. Measurement of cell count was performed through visual inspection of random sections of the optical microscope images and could thus have some measurement

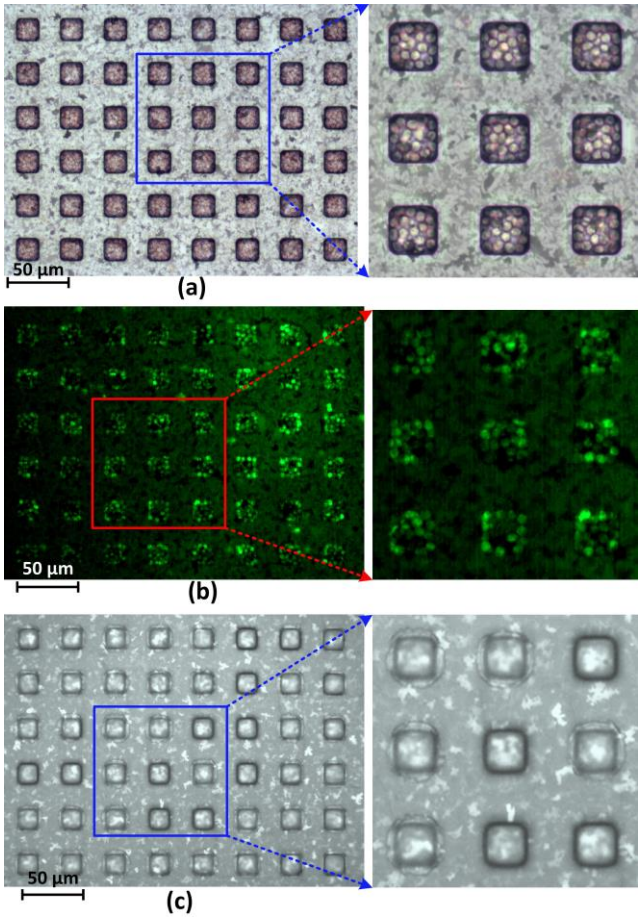

Figure 3.16. Optical and fluorescent photos of the red blood cells after DEP and lysis. (a) Photo of RBCs trapped in microwells (transmission mode). (b) Fluorescent photo of the RBCs trapped in micro-wells. (c) Optical photo of micro-wells after lysis. Bright speckles are graphene flakes (reflection mode).

error of ±0.5% of reported value. This performance is comparable to our prior work with 90% of filled microwells with cells using DEP approach where the device consisted of ITO electrodes [98]. The results are also similar to another work by Hyeon Kim et al. who reported 90% filled wells using dielectrophoretic approach for cell trapping by applying 3.5 Vpp for 3 min between patterned ITO electrodes in the microwells [125]. The efficiency of 95% for DEP cell trapping using device with ITO electrodes has been also reported by another work [107].

3.8 Summary

In conclusion, a transparent microfluidic platform with graphene electrodes for high throughput dielectrophoretic cell trapping and electrical cell lysis using DC electric field was demonstrated. Graphene was shown to be an ideal replacement for ITO, which is commonly used as a transparent conducting electrode in such applications, especially when one needs to apply DC electric fields for lysis where ITO serves as cathode and undergoes electrochemical reduction. This causes large Faradaic currents and changes the physical and chemical properties of the cells molecular components and their surrounding medium. The Faradaic reaction also degrades ITO electrode electrical properties and reduces its optical transparency over time. On the contrary, it was shown that graphene electrode is electrochemically inert and does not lose its optical transparency even when higher DC voltages are applied in contact with buffer solution. While graphene would be a reasonable choice for both the electrodes, these results were acquired with graphene as bottom electrode (as a replacement to ITO cathode) and ITO as top electrode to capture the electrode behavior. The platform showed high efficiency of the cell trapping and lysis with superior electrochemical stability compared to an all ITO based device**.** This work adds to an increasing evidence for choosing graphene as electrode material for application in biology and life sciences.

CHAPTER 4

Three Dimensional Graphene Transistor

In this chapter, a novel three dimensional field effect transistor (FET) is introduced and the results of electrical characterization are discussed. The channel of presented transistor is made of 3D graphene foam, which is a complex three-dimensional network of graphene. To realize a 3D gate, all-around of the graphene foam, ionic liquid and ionogel have been used as the gate. The results of the both configurations is discussed in continue. First, the ionic liquid gated 3D graphene transistor is introduced. In this device, a single to double layer of graphene foam immersed in ionic liquid is implemented as a channel of a transistor. Next the ionogel gated transistor with higher current capacity and semisolid/gel gate is introduced. The channel of this transistor is made of few layers of graphene, immersed in ionogel instead of ionic liquid.

The electrolytic double layer capacitance at the ionic liquid/ionogel and graphene interface provides all-around three-dimensional gating of the transistor. The high surface area of the graphene foam results in providing higher current carrying capacity than a

two-dimensional graphene transistor. Moreover, the nanometer thick electrolytic double layer formed at the high surface area of liquid/gel-graphene interface results in large gate capacitance that allows for low voltage operation.

4.1 Graphene foam, three dimensional form of graphene

Graphene is an atomically thin two-dimensional semi-metal with a strong ambipolar electric field effect, high carrier density, high carrier saturation velocity and remarkably high carrier mobility at room temperature, making it a promising candidate for many electronics devices and sensors [9,126]. Graphene foam is three dimensional form of graphene which preserve the most of two dimensional graphene properties and at the same time adds the advantages of higher surface area and possibility of using the third dimension of space.

4.2 Material characterization

Mono layer and few layer graphene foam used in this work are grown using chemical vapor deposition (CVD) on copper foam (Graphene supermarket). The scanning electron microscopy (SEM) images of the three dimensional graphene were taken using Zeiss EVO before and after etching away the copper (figure 4.1). The SEM image of the foam before etching away copper, shows the three dimensional structure of the graphene foam made of interconnected network of strips (Fig. 4.1 (a)). The images of a single to double layer graphene and few layers of graphene after etching away the copper presented in the figure 4.1 (b) and (c) respectively, indicate that graphene maintains the three dimensional structure of the foam after etching away the copper.

To investigate the elemental composition of the graphene foam after etching away copper, the X-ray photoelectron spectroscopy (XPS) was performed using Thermo

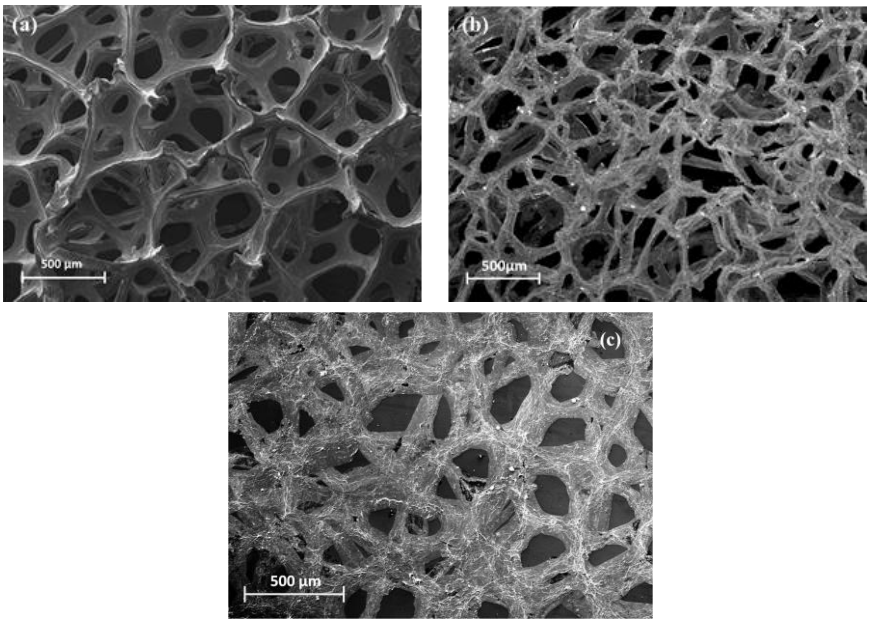

Figure 4.1. SEM images of Graphene foam. (a) Before etching copper. (b) Single to double layer of graphene after etching copper. (c) Few layers of graphene after etching copper.

Scientific K-Alpha XPS system. Results are shown in figure 4.2. The XPS results show the existance of the carbon, oxygen and trace amount of iron remaining after the etching process using ferric chloride. High resolution XPS spectra of copper is presented in Figure 4.2 (b) for further investigation. As it can be seen there is not any clear XPS peaks of copper after etching process and transfering the graphene foam on the glass substrate. Figure 4.2 (c) shows the high resolution XPS spectrum of the C1s which is corresponded to sp2 peak of graphene located at 284.4 eV.

The transmision electron microscopy (TEM) image of monolayer graphene foam on TEM grid, taken using JEOL 2100 system is presented in figure 4.3 (a). It shows the hexagonal lattice structure of the graphene and layers of it placed on each other in the foam. Electron diffraction pattern of the foam shown in figure 4.3 (b) indicates the six fold symmetry of graphene with several layers of the graphene laid down on each other. The Raman spectroscopy of the foam consisted of monolayer and few layers of graphene

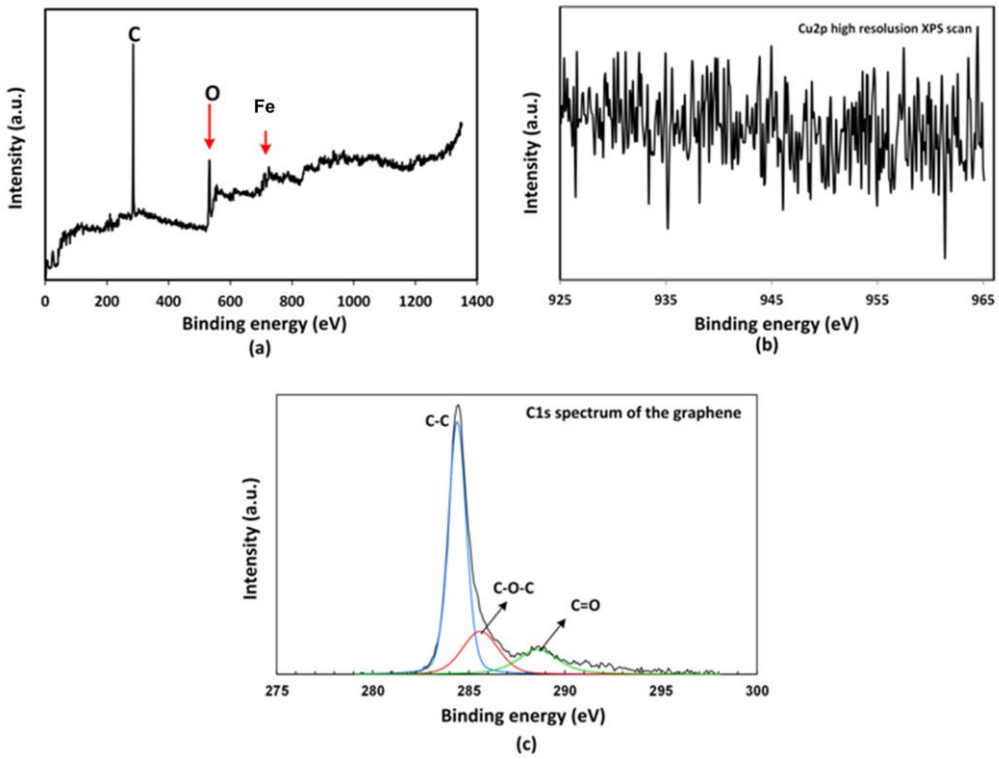

Figure 4.2. The X ray photoelectron spectroscopy of the graphene foam after etching away copper. (a) Full XPS spectrum. (b) High resolution XPS spectra (925-965eV) to investigate the existence of copper. (c) High resolution XPS spectra of the C1s peak located at 284.4eV.

and also the two dimensional monolayer of graphene for comparision, has been performed using Jasco NRS-3100 system, for further composition and crystaline structure investigations. The existence of the G peak and 2D peak with different intensities is observed for different samples. The intensity of G peak increases with increasing the

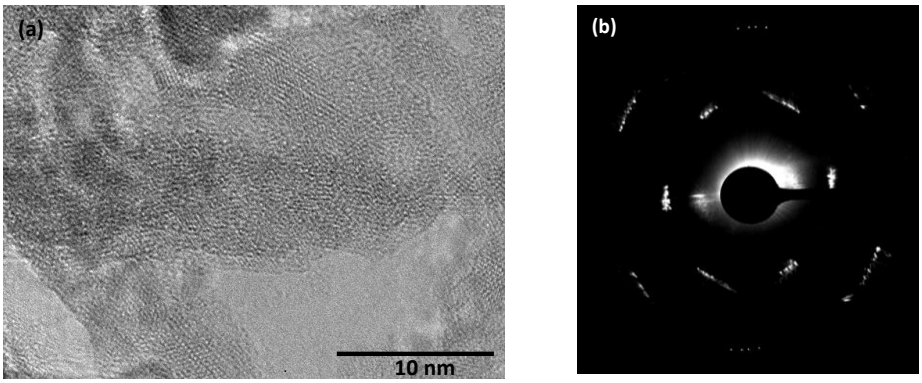

Figure 4.3. TEM results of graphene foam. (a) TEM image of the graphene foam. (b) The electron diffraction pattern of the graphene foam.

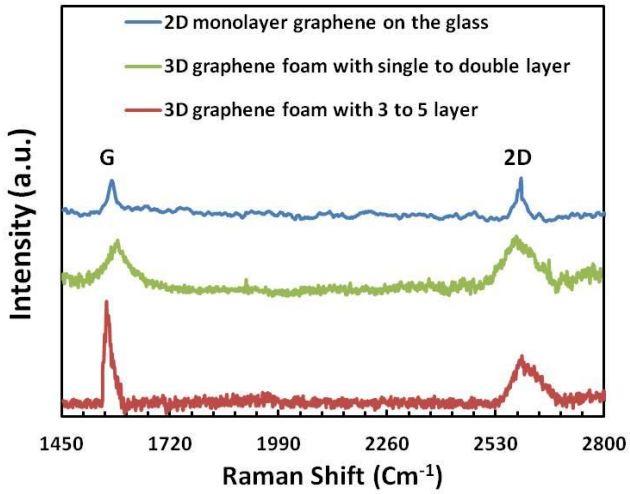

Figure 4.4. Raman spectrum of the three dimensional graphene foams and two dimensional graphene. It shows G and 2D peaks at 1534 cm-1 and 2610cm-1.

number of graphene layers while the intensity of the 2D peak decreases. These results indicate the existence of single to double layers of graphene in one of the graphene foam and few layers of graphene in the other one [127,128]. It is worthwhile to mention that the Raman spectroscopy result is an additional evidence of maintaining three dimensional structure of the graphene foam after etching away copper. The Raman spectrum of the monolayer graphene foam is obviously different than graphite. These result indicate that although after etching away copper, layers of graphene collapse and lay in a random manner in respect to each other (as it was shown in TEM images) but they place independent from each other which is not the case in graphite [129].

4.3 Ionic liquid gated three dimensional graphene transistor

As it was mentioned before, it is well known that because of zero band gap of graphene, transistors with graphene as a channel do not switch off, which is undesirable for RF and analog applications that can utilize its high carrier mobility and its ambipolar for digital logic applications. However there are advantages of using graphene transistor

nature for novel circuit configurations [130-132]. Gigahertz cut-off frequencies have already been reported for graphene-based transistors [130,133-135]. While this has made graphene an attractive alternative for transistors in beyond-CMOS technologies, its true potential may in fact be as an electronic interface to the biological systems primarily due its stable carbonaceous form which is atomically thin yet mechanically strong, and one that offers superior sensitivity to the electric field in its near-field environment enabling electrical recording of biological events or ultrasensitive chemical or biological sensing. So far, experimental demonstrations of field effect transistors using graphene, for either electronic or biomedical applications, have been limited to two-dimensional configurations of graphene [136]. The three-dimensional field effect transistor (FET) provides higher electrostatic gate control of the channel in order to achieve low voltage operation. An ultimate scaled version of this transistor is a nanowire with gate all-around configuration [137]. In these examples, while the gate is three-dimensional, the transistor channel itself is laid out along a single plane. True three dimensional transistors are one where both the channel and the gate can extend in all the spatial dimensions. One recent example of such a transistor based on silicon nanowires was realized at the tip of a microprobe for electrical recording from living cells [138,139]. Given the promise of graphene as a superior electronic material that is also biologically compatible, a three dimensional analog of a graphene transistor would be highly desirable. In this dissertation a three dimensional transistor based on graphene foam and ionic liquid as a gate is presented. The graphene foam consists of three-dimensional network of single and double layer graphene that extends in all the three dimensions. A metal contact on either end of graphene foam forms the drain and source contacts of the transistor. However, making a

solid-state gate is highly challenging for a complex three dimensional structure. We solve this issue by liquid gating of the three-dimensional graphene channel using an ionic liquid electrolyte. Liquid gating provides a natural all-around electrostatic control of the transistor channel. Ionic liquids are non-volatile over wide temperature and pressure range, highly polar, extremely conductive with high ionic strength at room temperature, therefore they are ideally suited as gate dielectric. They have the ability to create huge carrier accumulation in the semiconductor material controllable by electric field effect [140-143]. This is possible due to the formation of electrical double layers (EDLs) on the surface of semiconductor, which consists of large concentration of holes (electrons) in the semiconductor and anions (cations) in the electrolyte, resulting in huge capacitance per unit surface area. As it is well known, a higher value of gate capacitance results in higher carrier concentration, higher on-state current and lower operating voltages. Liquid gating of two dimensional single layer graphene FET was demonstrated by Chen et al using a ionic-liquid BMIM PF_6 with measured a p-type mobility of 1200 $cm^2.V^{-1}.s^{-1}$ [144]. More recently, a trilayer graphene FET was demonstrated using DEME-TFSI ionic liquid for magnetotransport properties [142]. Ionic liquids have also been used for many inorganic and organic transistors although reported mobilities and carrier densities have been much lower than what has been reported for ionic-liquid based graphene FET [143].

In the following sections, the fabrication and electrical characterization of three dimensional FET, based on graphene foam immersed in ionic liquid will be discussed. The channel of presented transistor is composed of complex three dimensional network of free standing single to double layer graphene surrounded all around by ionic liquid gate.

4.3.1 Structural model

Given that the transistor channel consists of seemingly random network of graphene, it is quite complex to estimate the electrical parameters and electronics properties of the device. The effective length and width of the transistor will be different than the drawn length due to three-dimensional nature of the device. In this section, we attempt to create a simple rough structural model to estimate the effective length and width of the channel based on the foam structure and dimensions as seen through an SEM picture. There is some approximation and averaging of the measured dimensions achieved from SEM images. Graphene foam can be simplified as a set of hemispheres, based on SEM images shown in figure 4.5 (a). Every hemisphere seems to resemble the structure made of interconnected irreducible elements that assemble as six interconnected pentagons, and each element is a triangular strips as shown in figure 4.5 (b). Our results show the average diameter of hemispheres is about 860 µm (Fig. 4.5 (a)). Carriers move on the available path on triangular strips that form these hemispheres and are not in straight lines. The effect of curvature of these strips on the effective channel length has been calculated and shown in Fig. 4.5 (a) using geometry of the device. Possible electron pathway is shown is Fig. 4.5 (b) and 4.5 (c) and it depends on the diameter of the hemisphere and the dimension of the pentagons and it is estimated to be around 360 µm. Based on this model and our calculations, the actual electron path length is to be 1.7 times of the given drawn device.

Figure 4.6 (a) shows the cross section of the strips in higher magnification. The width of the device is the sum of the circumference of the strips times the number of strips from source to drain. We model the interconnected parts as the triangular strips based on

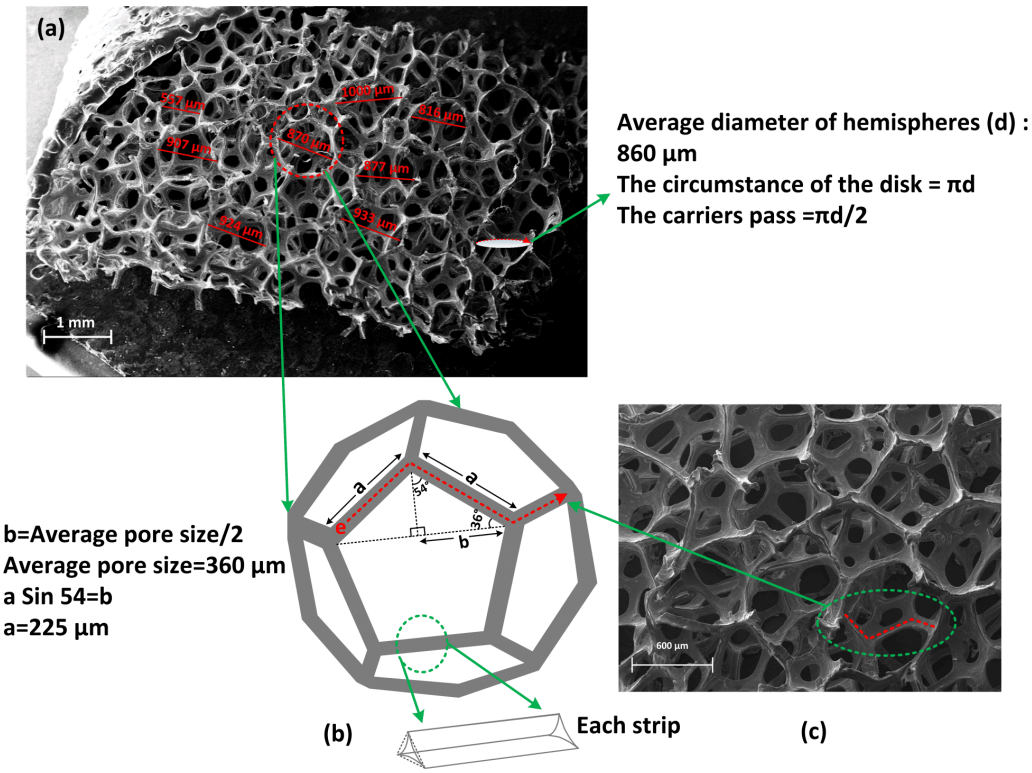

Figure 4.5. Proposed structural model of the three dimensional graphene foam and estimated actual electron pass length. (a) Top view SEM image of the foam. The average diameter of the hemispheres is about 860 µm which is used to estimate increasing the electron path due to curvature. (b) The possible electron path through pentagon in the plane page. (C) Magnified SEM image of the foam with highlighted electron path. Our estimation shows that the actual electron pass length is 1.7 times of the drawn device length for this device.

the morphology observed in SEM images shown in Fig. 4.6 (a). Every strip is modeled as a combination of the three arcs of three circles which are touching each other. We are able to estimate the chord length using several SEM photos taken randomly (see Fig. 4.6 (c)). Using these data we are able to estimate the length of the arc next to the same chord which is one over three part of every triangle circumference (Fig. 4.6 (b)). Figure 4.6 (d) shows the cross section of the foam. The number of the strips per millimeter width of drawn device has been estimated from different SEM images and it is about 6.3 strips per millimeter width of drawn device. The total width of channel is the sum of circumference for a total of 31.5 triangular strips (for drawn device width is 5mm) which results in an

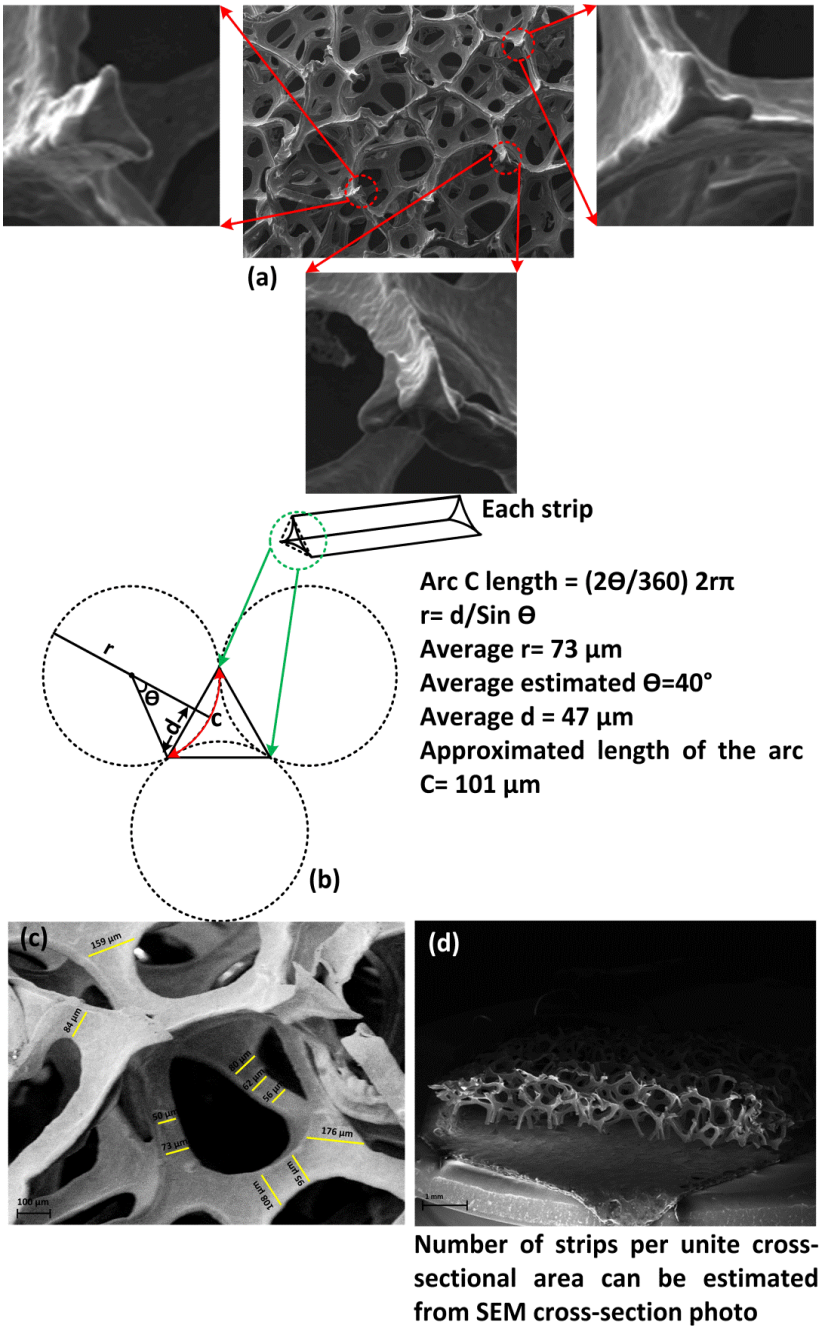

Figure 4.6. Proposed structural model of the three dimensional graphene foam and estimated actual width of the drawn device. (a) The SEM image of the cross section of the strips. (b) Geometric model of the triangular strips. (c) SEM images of the strips with indicated dimension of the strips (2d). (d) The SEM image of foam cross section which help to estimate the number of strips per unite cross sectional area.

effective value of width as 1.9 times of the drawn device width. This width estimate includes both the number of strips and the thickness of the device.

4.3.2 Device fabrication

Figure 4.7 shows the fabrication process flow. Briefly, one begins with a CVD grown graphene on the copper foam. The CVD grown monolayer graphene on the copper foam was cut in to the size of 5mm x 1600 µm, and it was held in the copper etchant (Ferric chloride $FeCl_3$ 0.06 molar) to etch away the copper. Then graphene is transferred on the glass substrate, which was cleaned using RCA method (hydrogen peroxide, 30%, ammonium hydroxide, 27%, and deionized water with the 1:1:5 proportions respectively at 80°C for 10 min). Next, the transferred graphene was rinsed with plenty of DI water to clean any chemical residue left over on the surface of the graphene from the etching

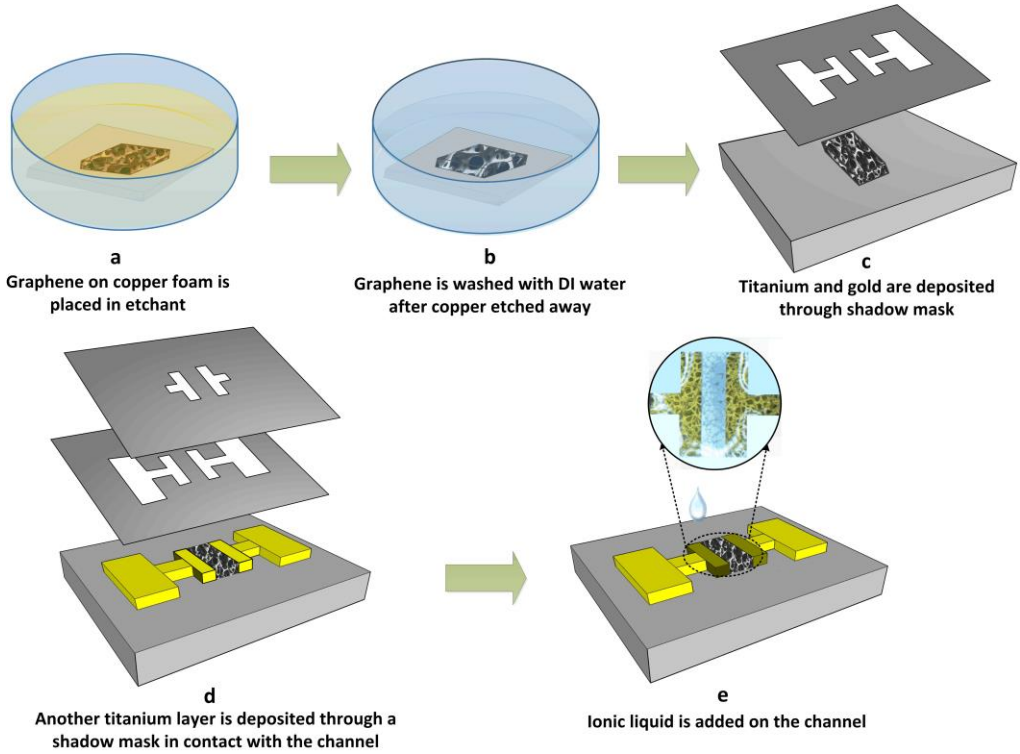

Figure 4.7. Device fabrication process (a) CVD grown graphene on copper foam is held in $FeCl_3$ solution. (b) Copper is etched and graphene is washed with plenty of DI water. (c) Titanium and gold are deposited through shadow mask to form source and drain contacts. The gold and titanium are not covering the graphene network all-around and it is shown in this schematic in this way just for simplicity. (d) A thin layer of titanium is deposited through another shadow mask to cover the gold in the area where contact is made with channel. (e) Shadow mask are removed and ionic liquid is added on the top of the channel. Metal electrode is suspended in the ionic liquid to apply gate voltage.

process. In the next step, titanium with 10 nm thickness followed by gold with 50 nm thickness are deposited using DC sputtering system to form drain and source contacts. This is followed by another deposition of 10 nm of titanium on the source and drain to prevent the leakage current. 1-Butyl-3-methylimidazolium hexafluorophosphate (BMIM-PF_6, 98%) was the choice for ionic liquid to serve as the liquid gate.

4.3.3 Electrical characterization

Electrical measurements were performed using probe station (Signatone H100) and semiconductor parameter analyzer (HP Agilent 4156A) at room temperature and atmospheric pressure in ambient environment. The schematic of the proposed device is shown in the figure 4.8. The three dimensional graphene foam serves as the active channel layer with ionic liquid (1-Butyl-3-methylimidazolium hexafluorophosphate, Bmim PF6, 98%) serving as the gate of the transistor, and metal contacts for source and drain terminals. Using ionic liquid as a gate results in a large capacitance at the liquid-channel interface allowing for low voltage operation of the device [142].

For proof of demonstration, we implement a transistor with gate length of 600 µm and

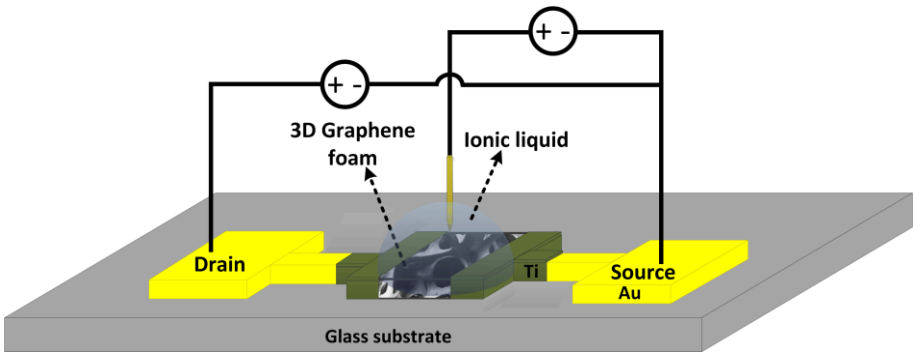

Figure 4.8. Schematic of an all-around three-dimensional liquid gated graphene transistor. The device consists of single and double layer graphene foam as an active layer and ionic liquid as a gate. Metal contacts are used for electrical connections.

width of 5 mm. The effective length and width of the transistor will be different than the drawn length due to three-dimensional nature of the device as discussed earlier. The device sizes were chosen for convenience of measurement and for proof of concept demonstration and could easily be scaled down using standard photolithography. Since graphene layers do not have any structural support after etching copper, micro and nano shrinks are developed that degrade the overall mobility of the carriers. We expect higher mobility of the carriers in graphene foam by preventing the collapse and shrinkage in the active layer after etching copper. This can be done by using a supportive layer during the etching of the copper and performing the process in a more controlled manner (such as adding an etchant at a constant flow rate and reducing overall mechanical vibrations). It is important to point out that the proposed liquid gated FETs are expected to be inherently slow due to the low mobility of the heavy ions in the ionic liquid; the shrinking of graphene does not impose any additional mobility degradation to affect the overall speed performance of the transistor.

Figure 4.9 shows the electrical measurement results for a single transistor. Changes in the drain current with respect to gate voltage with drain potential at 0.5, 0.6 and 0.7 V is shown in Figure 4.9 (a). Conductivity of the channel decreases for gate voltage sweep from -3 V to -0.6 V and again increases from -0.6 V to 1.6 V, beyond which it saturates. This is a well-known ambipolar electric field effect behavior of the graphene based FETs owing to the zero bandgap of graphene. The carrier type depends on the gate voltage; negative gate voltage creates a p-type graphene channel and positive gate voltage creates an n-type channel. The minimum conductivity point (between -0.4 to -0.6 V gate voltage in this device) is known as the Dirac point and the position is dependent to the doping

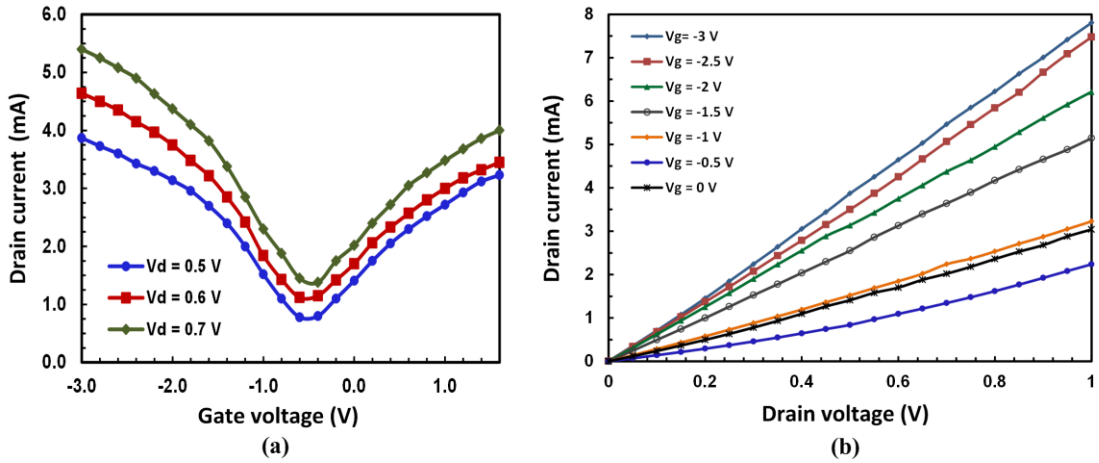

Figure 4.9. Electrical characterization of liquid gated 3D transistor. (a) Drain current versus gate voltage at different drain voltage. (b) Drain current versus drain voltages at different gate voltage between -3 V to 0 V.

and impurities.

The on/off current ratio in this device is about 5. In a long channel graphene transistor, the reported on/off current ratio usually is between 2-20 [47]. Figure 4.9 (b) shows the drain current versus drain voltage characteristic of the transistor. As the carrier velocity increases with increasing drain voltage, the drift velocity does not saturate for small values of V_{DS} and therefore saturation behavior is not observed in graphene transistors [47,145]. To calculate the contact resistance of the channel, resistance between source and drain is measured at different gate biases. From the slope of the curves, one can extract the channel resistance. To calculate contact resistance, channel resistance is subtracted from total resistance. Since there are two contacts, one at the drain and the other at the source, they happen to be in series and therefore the derived contact resistance is divided by two. Figure 4.10 shows the plot of total resistance between source and drain versus length of the device for different gate voltages. The extracted minimum contact resistance at the source/drain terminal is 6.87 Ω.mm and the extracted equivalent

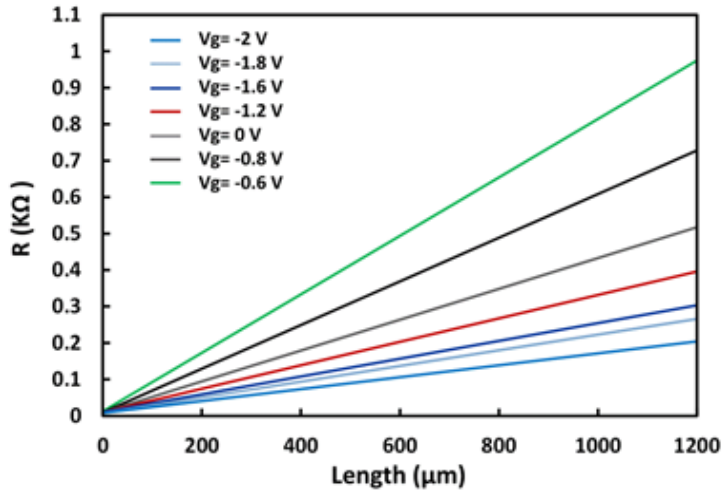

Figure 4.10. Plot of resistance between source and drain versus length of channel at different gate voltage. The channel and contact resistance are extracted using the plot of resistance between source and drain versus length of channel.

sheet resistance of the active layer is 620 Ω/□. Due to three dimensional structure of graphene, forming uniform all-around metal contact is challenging. We have observed the contact area optically and found gold metal over graphene layers, although it is possible that metal does not contact all around the graphene uniformly, which can be the primary reason for higher contact resistance in this device. Contact resistance and sheet resistance can be improved by decreasing the defects and shrinks in graphene. We believe that shrinks in the graphene foam after copper etching can be the secondary reason of high contact resistance.

The ionic solution used as a liquid gate is BMM PF_6 which created a double layer capacitance of approximately 11.7 nF at the interface with the graphene and this serves as the gate capacitance of the transistor. The capacitance was measured between gate and source using RLC meter for the frequency range of 20 Hz to 1 MHz using LCR meter (Agilent E4980A, 20 Hz to 2 MHz) and DC capacitance was extracted by interpolation to zero frequency.

Electrolyte and liquid gated graphene field effect transistor usually show hysteresis which is dependent to the gate voltage sweeping rate. In electrolyte gated transistors, electrical double layer forms at the interface of graphene and liquid due to applying gate voltage through liquid. This capacitance is much larger than conventional solid state capacitors due to very thin dielectric between graphene and ions and the distribution rate of potential in electrolyte is slow which results in hysteresis. Because the potential distribution and its relaxation time is not so fast with decreasing the gate voltage sweep rate hysteresis decreases [146]. Figure 4.11 shows hysteresis in liquid gated three dimensional transistor is clearly dependent on the gate voltage sweep rate.

The electronic performance indicates that liquid gating using high conductivity ionic liquid as a gate provides a high level of electrostatic control of the graphene transistor that results in high carrier concentration and high mobility in the transistor with very low operating voltages. While we have only explored a long channel transistor, the device could be scaled down considerably with even better electronic properties. Figure 4.12 (a) shows the drain current versus gate voltage for transistors with different channel lengths

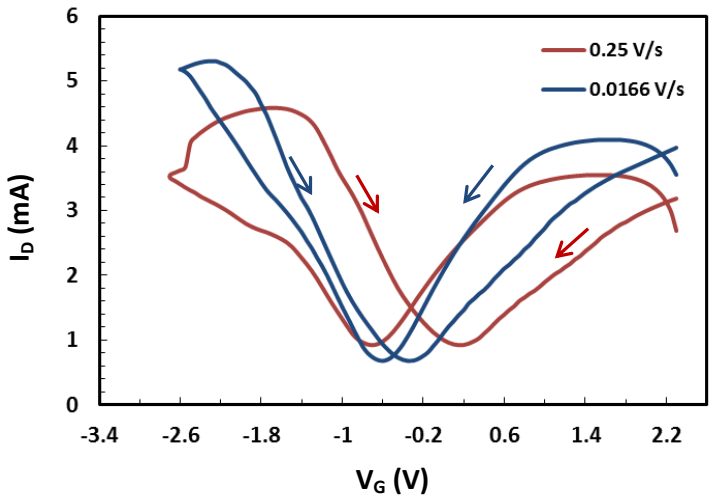

Figure 4.11. Hysteresis of three dimensional graphene transistor with two different scan speed.

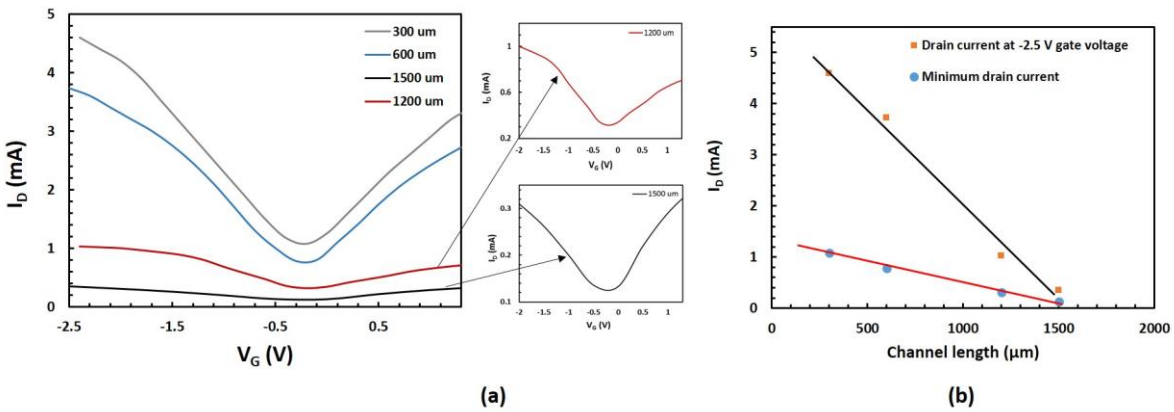

Figure 4.12. Device functionality versus channel length. (a) Drain current versus voltage gate for transistors with different channel length. (b) Changing drain current versus channel length for transistor with different channel length.

changing from 300 µm to 1500 µm. As it can be seen the slope of curves in linear section is increase considerably (more than ten times) by decreasing the channel length. This indicates that the mobility of the electrons and holes is increasing with decreasing the length of transistor which is clearly due to decreasing defects and scattering in shorter device length. This also results in increasing the current capacity of the device as it can be seen in figure 4.12 (b) when channel length decreases. The dimension of the graphene foam pore is dependent to the dimension of the copper foam on which it is grown. Growth of graphene foam with less than five monolayers and pore size of one micron or less has been reported [147]. Using such type of graphene, the device can be scaled down up to the limit of graphene foam pore size but fabrication of such small device still remain challenging due to complex three dimensional structure of device.

4.4 High current density Ionogel gated three dimensional graphene transistor

In the previous part, an ionic liquid gated three dimensional graphene network transistor on a glass substrate is introduced and discussed. The channel of this transistor contains mono to double layer graphene foam. Due to high surface area of the active

layer, a liquid gate, and the electrochemical stability of graphene, this device may have great potential for biological applications. However, for some applications, physical confinement of the ionic liquid is required for stable operation.

In the following, we have addressed this issue by using ionic liquids as an additive to a polymer framework forming an ionic liquid-based gel electrolyte, or ionogel, as a gate to provide physical stability of the liquid dielectric [148,149].

Ionogels are solution processable at room temperature, making them ideal for implementation at low temperatures on flexible plastic substrates. The ionic liquid chosen for this device was 1-ethyl-3-methylimidazolium bis(trifluoromethanesulfonyl)imide (EMI TFSI). Various polymers such as poly(ethylene oxide), poly(vinylidenefluoride-co-hexafluoropropylene) (PVDF-HFP), poly(methyl methacrylate) and poly(ethylene glycol) diacrylate (PEGDA) have been studied as polymer frameworks for ionogels [136,150]. Here, we have implemented a specific monomer, pentaerythritol tetraacrylate (PETEA), as the precursor to form the polymer framework due to its four reactive end groups that facilitate the formation of a highly cross-linked polymer network. A facile synthesis route of ultraviolet (UV)-initiated free-radical polymerization was utilized due to its robustness and quick reaction time of less than 10 minutes under UV exposure. A few nanometer wide electrostatic double layer capacitance forms at the graphene-ionogel interface, resulting in high capacitive coupling between the ionogel gate and graphene, facilitating charge carrier injection into the channel at low operating voltages [151,152].

For realization of the active layer of the transistor, a few layers of CVD-grown graphene on copper foam is transferred onto a parylene substrate after etching away the underlying copper. Metal contacts are deposited through a shadow mask to form source

and drain contacts and the gate is formed by UV curing of ionogel precursor solution added onto the channel region of the transistor. This flexible transistor demonstrates very high current capacity (~93 mA) at low operating voltages, less than 2.5 V drain to source voltage. This device shows very high current capacity in comparison to an equivalent two dimensional graphene transistor (26.72 times) fabricated and tested in this work.

4.4.1 Ionogel synthesis

Ionogel synthesis is done by our collaborator Anthony J. D'Angelo under supervision of Professor Matthew J. Panzer in Department of Chemical and Biological Engineering at Tufts University.

Synthesis began by preparing the ionogel precursor solution in which EMI TFSI, the photoinitiator (2-hydroxy-2-methylpropiophenone, HOMPP), and PETEA were combined in a small vial and measured by an analytical balance. The ionogel composition consisted of 2 wt. % HOMPP, 14.88 wt. % PETEA, and the remainder (83.12 wt. %) EMI TFSI. The vial was then sufficiently mixed by using a standard vortex mixer for 1 minute. Solutions were visibly determined to be well-mixed and homogenous. The ionogel precursor was cured and cross-linked via UV irradiation at 365 nm (Spectronic Corp., 8 W) for 10 minutes. It was confirmed that the gel was a solid-state material by verification of minimal flow.

For electrical characterization testing, the ionogel precursor solution was injected into a parallel plate geometry setup of two tin-doped indium oxide-coated glass electrodes (ITO) (Thin Film Devices, Inc.) sandwiching an annular poly(tetrafluoroethylene) spacer (PTFE, outer diameter 13.2 mm, inner diameter 6.35 mm, thickness 1.58 mm). Both the spacer and ITO electrodes were cleaned via sonication in a sequence which includes 2

vol. % Micro 90 in DI water, DI water, acetone, and boiling isopropanol. The spacer contained a small incision for syringe placement to inject ionogel precursor solution. The glass/ITO/precursor solution/ITO/glass sample was exposed to UV radiation at 365 nm for 10 minutes to form the ionogel device. AC impedance spectroscopy measurements were performed under ambient temperature (22 °C) and pressure conditions. AC impedance spectra were measured using a VersaSTAT 3 potentiostat with a built-in frequency response analyzer (Princeton Applied Research) over the frequency range of 1 Hz to 100 kHz using a sinusoidal voltage amplitude of 10 mV. Cyclic voltammetry performed using the VersaSTAT 3 was used to analyze the capacitive behavior of the gel electrolyte under linear positive and negative voltage sweeps at a scan rate of 1 V/s. Mechanical characterization was performed by compression testing via free-extension mode using a dynamic mechanical analyzer, RSA3 (TA Instruments).

The ionic liquid, EMI TFSI, was purchased from EMD Chemicals Inc. and was stored in a nitrogen-filled glove box until the time of use to prevent moisture absorption. Pentaerythritol tetraacrylate was purchased from Sigma Aldrich and stored in a nitrogen-filled glove box until time of use. The photoinitiator, HOMPP, was purchased from Sigma Aldrich.

4.4.2 Ionogel characterization

Ionogel characterization is done with our collaborator Anthony J. D'Angelo under supervision of Professor Matthew J. Panzer in Department of Chemical and Biological Engineering at Tufts University.

For electrical characterization of the ionogel, precursor solution was injected between two glass slides coated with ITO and separated by a PTFE spacer. After curing the

precursor under UV, AC impedance spectroscopy was performed over the frequency range of 1 Hz to 100 kHz. The AC impedance response captures both the resistive and capacitive behaviors of the ionogel across the entire frequency range. As it can be seen in figure 4.13 (a), the magnitude of impedance versus frequency indicates a combination of resistive and capacitive behavior of the ionogel. At low frequencies, less than 1 kHz, the magnitude of the impedance changes with frequency, which is due to the predominantly capacitive behavior of the ionogel. The series resistance of the testing setup, consisting of both ITO electrodes and electrical leads, was approximately 80 Ohms. The phase angle of impedance, θ, is defined as:

$$\tan\theta = \frac{Z''}{Z'} \qquad (4.1)$$

Where Z' and Z'' are the real and imaginary components of impedance, respectively. Figure 4.13 (b) shows the phase angle change versus frequency. A phase angle of -90° represents a purely capacitive response, and a phase angle of 0° is characteristic of a pure resistive response. As seen in figure 4.13 (b), at low frequencies the gel electrolyte behaves primarily as a capacitor, while at high frequencies resistive behavior is dominant. Cyclic voltammetry was used to analyze the capacitive behavior of the gel electrolyte under linear positive and negative voltage sweeps at a scan rate of 1 V/s. As seen in figure 4.13 (c), the current response of the ionogel is close to an ideal rectangular shape required for a capacitor. The voltage window was pushed to 2 V, and it is clear that the electrolyte is stable under these conditions while showing few negative side effects from ambient moisture absorption. The capacitance of the gel can be calculated using the following equation:

$$i = Cv \qquad (4.2)$$

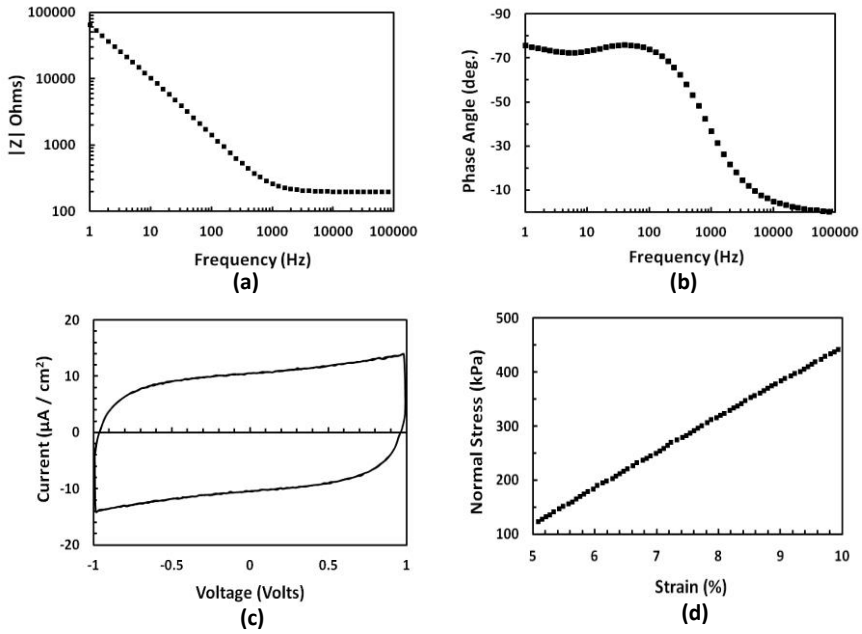

Figure 4.13. Electrical and mechanical characterizations of the ionogel electrolyte. (a) Magnitude of impedance versus frequency. (b) Phase angle of impedance versus frequency. (c) Cyclic voltammogram measured at a voltage scan rate of 1 V/s. (d) Compressive stress versus strain data.

Where i is current, ν is voltage scan rate, and C is capacitance. The capacitance per interfacial area between the ionogel and the planar electrodes is calculated to be 10 $\mu F/cm^2$.

Free-extension compression testing in the axial direction was performed on the gel electrolyte to yield a stress vs. strain curve up to 15 % strain. A linear response is observed in the region of 5 % to 10 % strain, as shown in figure 4.13(d). The elastic modulus (E) can be calculated by the following equation:

$$\sigma = E\varepsilon \qquad (4.3)$$

Where σ is the applied normal stress, E is the elastic modulus, and ϵ is the strain of the sample in the axial direction. Elastic modulus is calculated by determining a best-fit line to the stress-strain data and evaluating its slope. For the 14.8 wt.% PETEA in EMI TFSI ionogel, an elastic modulus (E) of 6.56 MPa was calculated with a best-fit line R2

value of 0.9997.

4.4.3 Device fabrication

The fabrication process began with the deposition of parylene, which served as the flexible substrate (see figure 16). Parylene-C with thickness of 28±2 µm was coated on a silicon wafer using a parylene coater system (Specialty Coating Systems PDS2010). The dimer was monomerized at 690 °C and evaporated at 175 °C; parylene was deposited at 135 °C. After deposition, parylene was separated from the silicon wafer and placed on a piece of glass for physical support during transistor fabrication. Figure 4.14 shows the fabrication process flow. The CVD grown graphene on copper foam was placed in copper etchant (ferric chloride, $FeCl_3$, 0.06 molar) to etch away the copper. Thereafter, graphene

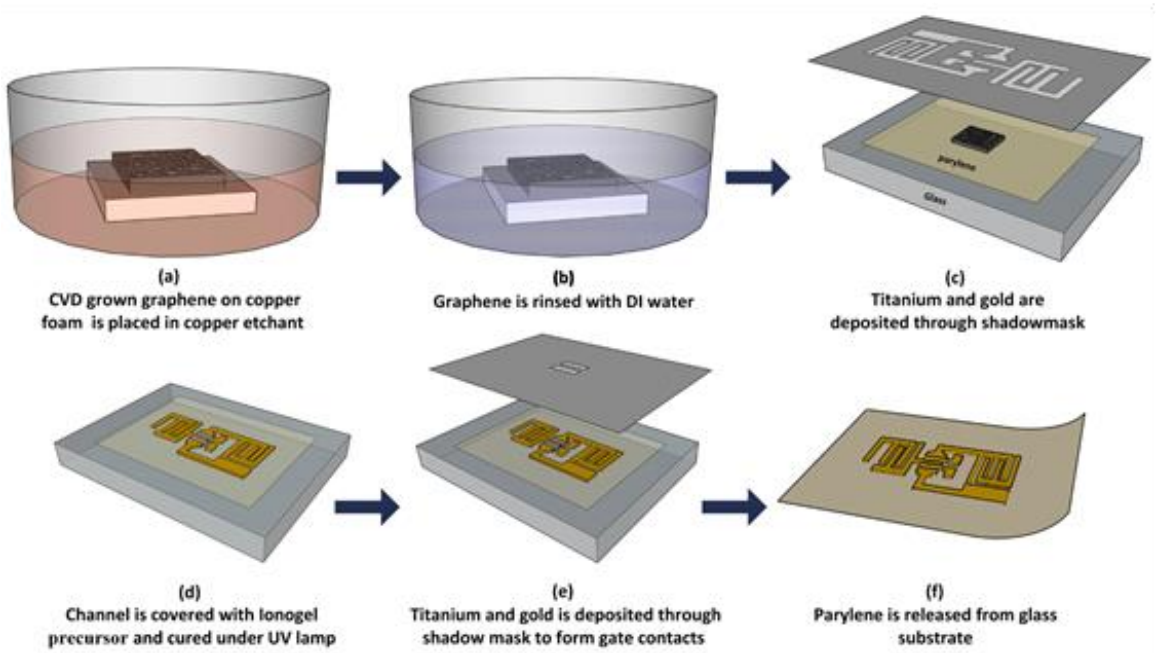

Figure 4.14. Fabrication process of three dimensional graphene transistor on parylene. (a) CVD-grown graphene is placed in $FeCl_3$ solution. (b) Graphene is rinsed with DI water. (c) Titanium and gold are deposited through shadow mask to form contacts and connections. (d) Ionogel precursor is placed on the channel and cured under a UV lamp. (e) Gate contact is formed by deposition of titanium and gold on the ionogel. (f) Parylene, which was held on the glass for physical support, is released.

on the parylene substrate was rinsed with a sufficient amount of deionized water to remove the chemical residue left over from the etching process. Titanium (30 nm) and gold (220 nm) were deposited using DC magnetron sputtering (NSC 3000) through a shadow mask to form source and drain contacts (with 1500 µm length and 5mm width). The length and width of the transistor channel were 600 µm and 5 mm, respectively. In the next step, ionogel precursor solution was spin coated onto the device at 1000 rpm, then cured under the UV lamp through a shadow mask for 10 minutes. After the ionogel was sufficiently cured, titanium and gold were deposited on the top of the ionogel to form the gate contact.

A two dimensional graphene transistor was fabricated to compare its current density with the three dimensional graphene transistor. To fabricate this device, a monolayer of graphene was transferred onto a glass substrate and covered with photoresist. The photoresist was then patterned using optical lithography, with dimensions of 1mm×5mm used as a mask to pattern the graphene by oxygen plasma etching (300 W for 30 s). Then photoresist was removed using acetone, and the sample was rinsed with isopropanol and DI water and dried by blowing air. The sample was heated at 500 °C in nitrogen atmosphere for 20 min to remove any residue of the photoresist left over from processing. In the next step, source and drain contacts were formed by sequentially depositing titanium and gold through a shadow mask.

Then, ionogel precursor was spin coated onto the channel and cured under UV through another shadow mask. The gate contact was formed on top of the ionogel by depositing titanium and gold through a final shadow mask. The length and width of this device were600 µm and 5 mm, respectively, which is the same as the length and width of the

three dimensional graphene transistor.

Three different logic-gates, NOR, NOT and NAND were formed to investigate the functionality of the transistors. Even though graphene exhibits no bandgap and therefore is not an ideal switch, typically required for digital applications, one can still construct functional logic gates for large area applications as shown here. We utilize resistive loads for NAND and NOR gates and complementary configuration without the resistor similar to conventional complementary MOSFET-like configuration for the realization of the NOT gate. Interdigitated metal was used to form connections between transistors and the resistors, and a simple graphite ink (PELCO® Conductive Graphite) with 300 Ω/□ sheet resistance was used between metal connections to form the resistors needed for the logic gates. This conductive ink can be removed easily making it possible to reconfigure the circuits as needed. The value of each resistor is dependent on the width of conductive ink between metal connections.

To study material characteristics of the graphene foam, the Raman shift was studied using a Raman spectrometer (Jasco NRS-3100) and Zeiss EVO scanning electron microscopy was used for taking scanning electron microscopy images. Electrical measurements were performed at room temperature and atmospheric pressure in ambient environment using a semiconductor parameter analyzer (HP Agilent 4156A) and probe station (Signatone H100).

4.4.4 Electrical characterization of Ionogel gated three dimensional transistor

Figure 4.15 (a) shows drain current changes versus gate voltage at different drain voltages (0.25 V to 2 V) in which gate voltage is swept between -2.5 V to 2.5 V. The transistor achieves a current capacity as high as 93 mA at 2.5 V gate voltage and 2 V

drain voltage. Conductivity of the channel decreases with sweeping gate voltage from -2.5 V to the Dirac point, where the channel exhibits minimum conductivity, and increases again as the voltage is increased from Dirac point to 2.5 V. In graphene, the carrier type depends on the polarity of the applied gate voltage. With negative gate bias, holes serve as the majority charge carriers and the channel is p-type, and at positive gate bias, electrons are the majority charge carrier and the channel is n-type. As it was mentioned earlier, this behavior is known as the ambipolar field effect and it is attributed to a non-existence of a bandgap in graphene.

The on-off current ratio of the device is about 2. The on-off current ratio of the device can be increased by decreasing the device size and by improving the metal contacts [47]. Our previous study showed that the contact resistance of three dimensional graphene transistors (6.87 Ω.mm) is higher than that of conventional two dimensional graphene transistors. We believe that several factors contributed to the higher contact resistance in this type of transistor which was discussed earlier in this chapter. In our previous study, mono- to double layer graphene foam was used as a channel for the three dimensional graphene transistor and an equivalent channel sheet resistance of 620 Ω/□ was extracted. In this transistor, number of layers in the graphene foam is more, resulting in an equivalent sheet resistance of 37 Ω/□, which represents 94 % reduction in the channel resistance. Changes in drain current versus gate voltage at a low drain voltage of 50 mV are shown in figure 4.15 (b). This result shows a relatively high current capacity in a transistor with channel length as long as 600 μm at drain voltage as low as 50 mV. Since graphene foam possesses a high surface area and low sheet resistance, this device shows higher current capacity in comparison to the two dimensional graphene

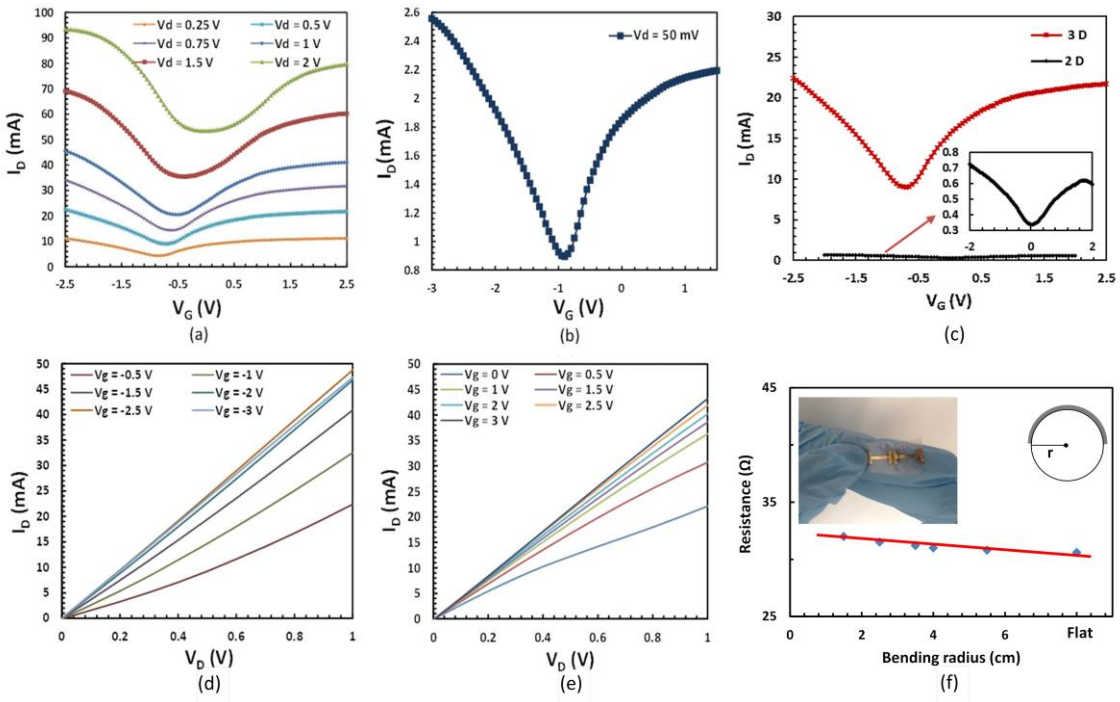

Figure 4.15. Electrical characterization of the device. (a) Plot of drain current versus gate voltage for different drain voltages; (b) Plot of drain current versus gate voltage at 50 mV drain voltage; (c) Comparisons of drain current between 2D and 3D graphene transistors at 0.5V drain voltage; (d) Plot of drain current versus drain voltage for different gate voltages between -0.5 V to -3V; (e) Plot of drain current versus drain voltage for different gate voltage between 0 V to 3V; (f) Drain to source resistance for different bending radius, inset is the photo of the device.

transistor with the same channel dimensions (600 µm length and 5mm width). Figure 4.15 (c) compares the transfer characteristics of two dimensional and three dimensional graphene devices at 0.5 V drain voltage. Our results show that the drain current at -2 V gate voltage in this three dimensional transistor is 26.72 times more than the equivalent two dimensional transistor.

Figures 4.15 (d) and (e) show the drain current versus drain voltage for different gate voltages between -3 V to 3 V. Since graphene does not have a band gap, carrier density increases continuously with increasing V_D; therefore, the current does not reach saturation for values of applied electric field in this graphene transistors. To study the flexibility of the transistor, drain to source resistance has been measured at different

bending radii (r). Results are shown in figure 4.15 (f). Based on our findings, less than a 4% change occurred for bending radii of 15 mm. The inset of figure 4.15 (f) shows the fabricated graphene transistor on the flexible substrate (parylene).

To demonstrate current carrying capacity, the fabricated transistor was used to drive three LEDs, where their brightness depends on the current level through them. The circuit schematic is shown in figure 4.16 (e). Three LEDs are connected in parallel with each other and in series with the transistor at source terminal. To demonstrate actual performance, the LEDs were held next to the screen semiconductor parameter analyzer during an experiment where V_G was swept from 2.5 V to -2.5 V. Due to LEDs internal resistance the Dirac point of transistor had shifted to higher V_G. Figure 4.16 (a) to 4.16 (d) show the transfer characteristics of a transistor while LEDs are driven. As seen from the figure, by sweeping V_G from +2.5 V to -2.5 V, LEDs turned on with higher biasing

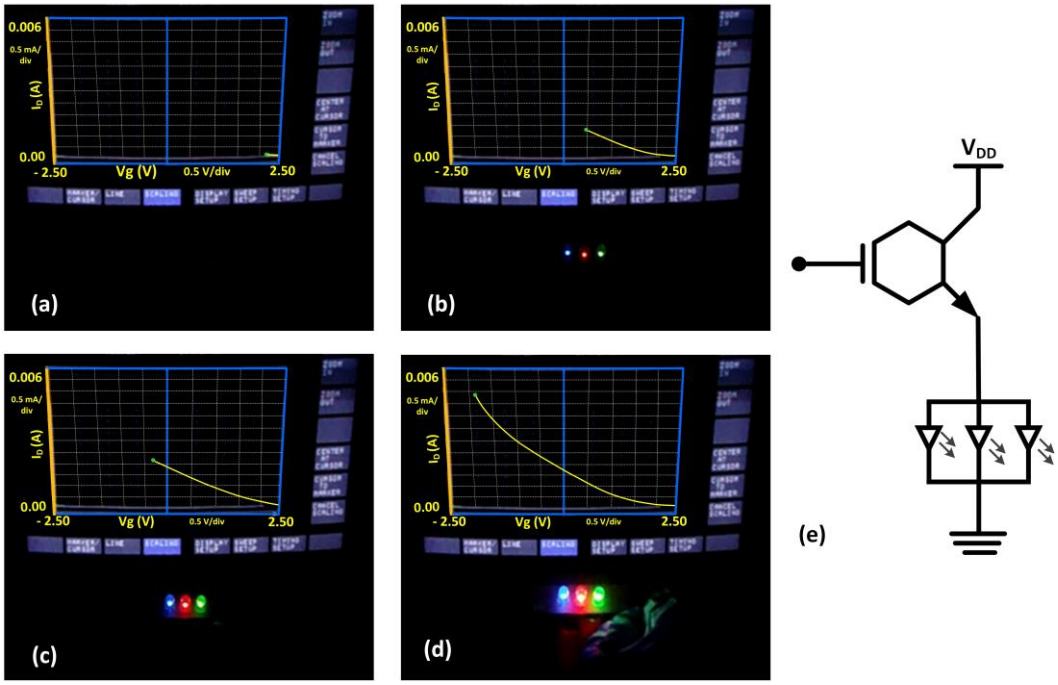

Figure 4.16. Driving LED using high current capacity 3D graphene transistor (a) to (d). (e) The schematic of the circuit.

resulting in high bias currents and consequently brighter output. This transistor can find use in many applications needing high current carrying capacity such as power amplifiers and power electronics.

To investigate the functionality of the device, three different inverter circuits were also implemented. Two transistors with interdigitated metal connections were fabricated on a parylene substrate. This circuit was designed to be reconfigurable. Graphite ink with a sheet resistance of 300 Ω/□ was used instead of a discrete resistor to serve as resistive load. Graphite ink was painted in different widths to obtain various resistance values. Applied ink can be easily removed in one place and be painted in another location to form various circuit configurations. To demonstrate actual performance, the LEDs were held next to the screen of the semiconductor parameter analyzer during an experiment where V_G was swept from 2.5 V to -2.5 V. Figure 5 (a) to 5 (d) show the transfer characteristics of a transistor while LEDs were driven. Due to LEDs internal resistance the dirac point of transistor had shifted to higher voltages. As seen from the figure, sweeping V_G from +2.5 V to -2.5 V, LEDs turned on with higher biasing resulting in high bias currents and consequently brighter output. This transistor can find use in many applications needing high current carrying capacity such as power amplifiers and power electronics.

A photo of the fabricated circuit on a parylene substrate is shown in figure 4.17(d). The results for the different configurations, are shown in figures 4.17 (a), 4.17 (b), and 4.17 (c). Pulses of -2 V to 2 V were applied as an input to the circuit. The V_{DD} and V_{SS} were set to 2 V and -2 V, respectively. The inverter circuits can perform functionally in different configurations. Charging and discharging times are dependent on the

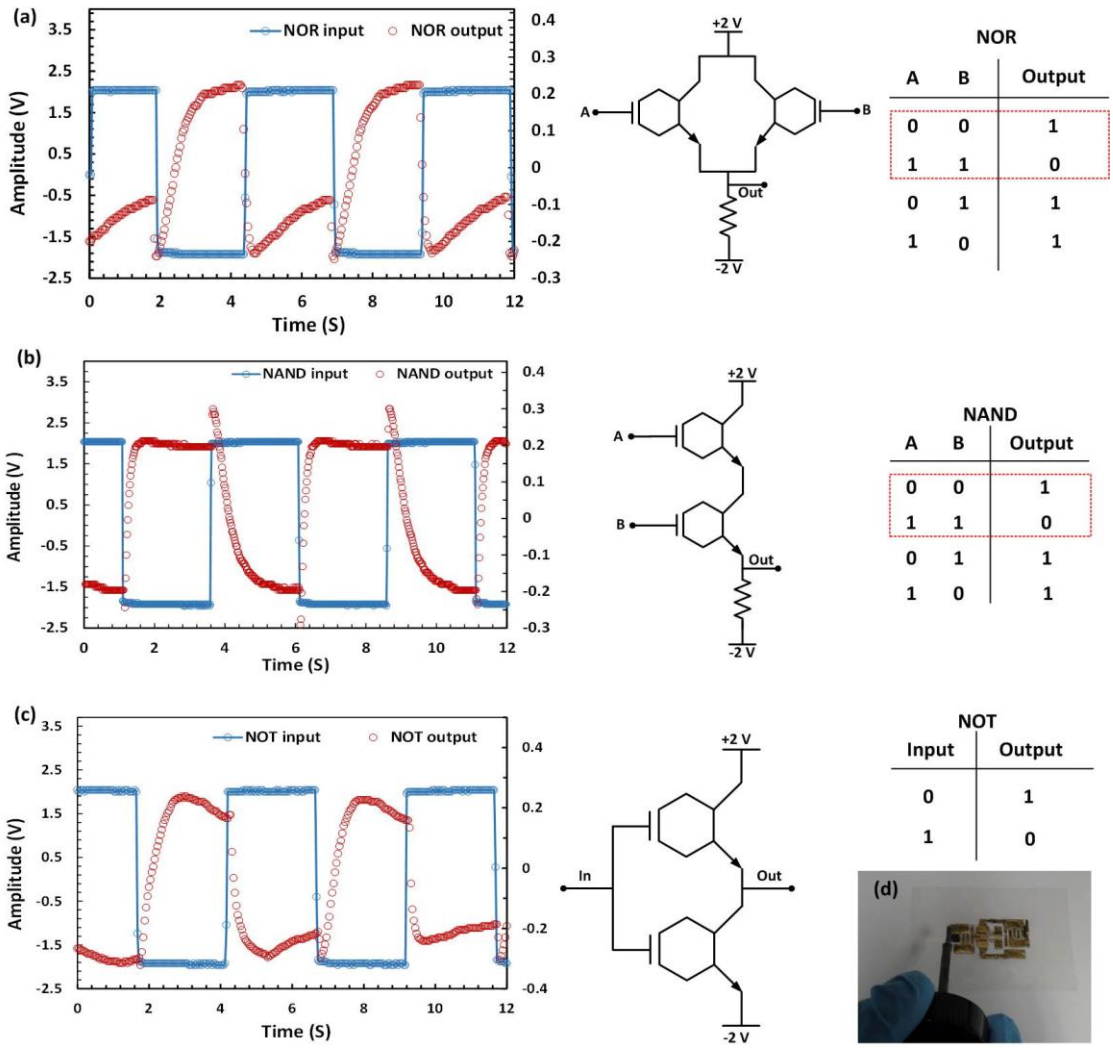

Figure 4.17. Electrical measurement of different circuit configurations. (a) NOR; (b) NAND; (c) NOT; (d) Reconfigurable resistor is formed by brushing graphite ink between titanium-gold connections for different circuit configurations.

transistor properties (gate capacitance, source/drain capacitance, sheet resistance of the resistive load) as well as circuit configuration.

4.5 Summary

In conclusion for the first time, an all-around three dimensional liquid and Ionogel gated graphene transistor were presented. The liquid gated transistor is made of single and double layer graphene in a foam configuration as an active layer with ionic liquid as

a gate. The transistor has very large surface area due to the three dimensional structure of the graphene. The combination of high surface area of the active layer and the use of ionic liquid as gate results in large double layer capacitance at the liquid channel interface which provides high level of the electrostatic control over channel conductivity at very low operating gate voltages. Avoiding the use of supportive layer for the graphene structure causes shrinks and ripples which had an undesirable effect of reducing the overall mobility of charge carriers. Decreasing shrinks and ripples of the graphene will improve the electronic properties of the transistor and will be the focus of future work. Next the three dimensional graphene foam based transistor with ionogel as a gate dielectric for realization of a flexible transistor was presented in this chapter. This transistor has been fabricated on a flexible parylene substrate with a channel made of few layers of the graphene foam and shows 26.72 times higher current density in comparison with a two dimensional graphene transistor of similar size. We believe that the higher current capacity of this transistor is due to higher surface area of this device and further increase in porosity of the foam with deceasing the pore size to the few microns, results in extremely high current capacity transistor. The fabrication process of this device is performed at room temperature and ambient pressure, making it suitable for realization on many flexible polymeric substrates. We believe that with advance lithography, scaling down, improving metal contacts and the quality of the graphene, very high performance three dimensional graphene based transistor can be fabricated. Such device will find new and exciting applications in large area electronics and life sciences such as electrical recording and stimulation of single cells, cell networks, tissues and organs, both ex-vivo and in vivo.

CHAPTER 5

Three Dimensional Graphene Transistor for pH Sensing

In this chapter a pH sensor based on three dimensional graphene transistor is introduced and its potential for real time monitoring of pH in biological environment is discussed. The 3D graphene based pH sensor can monitor the pH at high ionic strength medium with high sensitivity. Below, the motivation behind of this work, the process of the device fabrication and sensor functionality are presented.

5.1 Motivation and background

Owing to all carbonaceous form and biocompatibility of graphene, it has been found a lot of application in bio-electronics [153,154]. Large varieties of bio molecules have been sensed using liquid gated graphene based sensors during recent years [155-157]. Graphene can be made very sensitive to the surrounding environment due to its atomic thickness which makes it promising for sensing charge molecules. This mechanism of sensing is known as charge-detection based sensing mechanism and it also has been used

to sense the pH [158]. However, performance of pH sensing using graphene transistors has not been consistent with reported sensitivities varying widely from 17 to 99 mV/pH [159-162]. Recently, it has also been shown that a perfect defect-free graphene transistor is not sensitive to the pH ions and pH measurement is mediated by existence of defects and dangling bonds on graphene surface and edges. Leakage current through bare source and drain gold contacts also influences the overall measurement [162]. Thus, the quality of the graphene and the leakage current through bare electrodes strongly dictate the sensitivity of the graphene transistor to pH.

Another problem associated with charge-detection based sensing of pH especially for bio applications is the limited sensitivity to pH due to charge screening at high ionic strengths in biological medium. At any electrode-electrolyte interface there is a presence of electrical double layer and effect of potential on the electrode decreases exponentially away from the electrode-electrolyte interface. The effect is captured by the characteristic length known as Debye length beyond which the electrostatic effect of the electrode is minimal, and is defined as [159]:

$$\lambda_D = \sqrt{\frac{\varepsilon K_B T}{q^2 \sum_i Z_i^2 n_{i0}}} \qquad (5.1)$$

Where ε is permittivity, K_B is Boltzmann's equation, T is temperature, q is electron charge and Z_i is charge of the species i and n_{i0} is the concentration (number per volume) of the species *i* at equilibrium neutrality. At constant temperature Debye length is just dependent to the permittivity and ionic strength of the electrolyte in contact with channel. Most bio-sensing are performed in aqueous solutions with high ionic strength which the Debye length is very short. As an example in 100 mM aqueous electrolyte at room

temperature, the Debye length is only about 1.3 nm beyond which the charge carriers in the bulk are not affected by the electrode potential. In the most biological medium, the electrolyte concentration is higher than 100 mM, for example the extracellular fluids and human blood serum, the osmolality is between 277 to 305 mOsmol/Kg which correspond to 270 and 297.4 mM respectively [163]. Debye length in such concentration is even less than the estimated value. Therefore to be able to sense biomolecule in biological samples like as blood serum, urine and extracellular fluids, using ion sensitive electrodes, one needs to perform desaltation of sample to reduce the overall ionic strength [164].This is one of the reasons why existing pH sensors cannot work directly with biological fluids. However, for real time monitoring especially in emergency care, sensing of pH and other ions in the blood and biological fluids without sample preparation can be extremely useful. The normal pH of the blood in mammalian is between 6.8 to 7.8 and in human, the arterial pH of blood is between 7.37 to 7.42. If arterial blood pH falls below 7.37 acidosis occurs. Sever acidosis can lead to shock and death [165,166].

It has been shown that by adding oxide on graphene, OH groups at the surface of oxide in contact with electrolyte, can be protonated or deporotonated based on the pH of the solution and oxide surface composition [167-170]. Using aluminum oxide coated graphene channel for sensing pH is reported and it has been shown that by growing less than 2 nm of Al_2O_3 using ALD at low temperature, the sensitivity of the sensor increases from 6 mV/pH to 17±2 mV/pH. The reason of still low sensitivity of reported device is that growing less than 2nm of uniform oxide with the mentioned conditions is not feasible. The sensitivity of 40 to 50 mV/pH, by adding high quality aluminum oxide on the gate of transistor has been reported [163,168].

In this chapter the functionality of the three dimensional graphene as a channel of transistor, coated with 20 nm hafnium oxide using atomic layer deposition as a gate oxide for pH sensing in biological environment is discussed. This device shows the sensitivity of 79 ± 7 mV/pH, at high concentration of background electrolyte like DPBS or blood serum. We believe that high surface area of the graphene foam and its higher volumetric coverage is the reason for high sensitivity of the device at high concentration of the background electrolyte.

5.2 Sensor fabrication

Fabrication process of three dimensional graphene transistor has been presented in our previous work in detail, in this work additional HfO_2 layer has been added as a sensing surface [171]. The fabrication flow process has been shown in figure 5.1. Briefly CVD grown graphene was placed in ferric chloride ($FeCl_3$, 0.06 M) to etch a way copper, then rinsed with sufficient amount of deionized water (DI water) to remove the residue left over from etching process. Titanium and gold were deposited through shadow mask using DC magnetron sputtering (NSC 3000) with the thickness of 30 nm and 220 nm respectively to form source and drain contacts. The length and width of transistor were 600 µm and 5mm respectively. In the next step 20 nm of HfO_2 was deposited using Savannah atomic layer deposition (ALD, Cambridge NanoTech) all over the device. Then additional thin layer of PDMS (Polydimethylsiloxane) was used as a protective layer to prevent any direct physical contact between gold (source and drain contacts) and electrolyte thus minimizing leakage current. A well is made around the channel from PDMS and bound to the device, to prevent spreading electrolyte on the device.

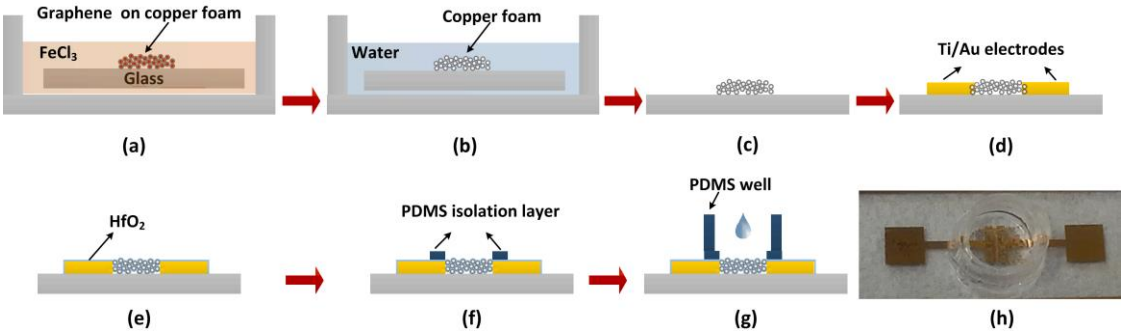

Figure 5.1. Cross sectional view of the pH sensor fabrication process. (a) CVD grown graphene on copper foam is placed in $FeCl_3$. (b) After etching away copper graphene is rinsed with DI water. (c) Graphene foam is dried. (d) Ti/Au were deposited through shadow mask to form source and drain connections. (e) HfO_2 is grown on the device. (f) Contacts area close to the channel are covered with PDMS protective layer. (g) PDMS well is fabricated and attached to the device. (h) Photo of the fabricated device with PDMS well.

5.3 Sample preparation

Dulbecco phosphate buffered saline (DPBS) (calcium chloride, $CaCl_2$, 1 gL^{-1}, magnesium chloride, $MgCl_2.6H_2O$, 1 g L^{-1}, potassium chloride, KCl, 2 g L^{-1}, potassium phosphate monobasic, KH_2PO_4, 2gL^{-1}, sodium chloride, NaCl, 80 g L^{-1}, sodium phosphate dibasic, $Na_2HPO_4.7H_2O$, 21.6 g L^{-1}, water) [172], and blood serum of a male sprague-dawley rat were used to test the functionality of the pH sensor at actual biological background. Different DPBS (150 mM) based pH solutions with pH range of 3 to 9 were made by adding sodium hydroxide (NaOH) and Hydrochloric acid (HCL). The rat blood serum at four different pH values from 6.4 to 7.7, which is the critical range of the pH in blood acidosis diagnosis, was used for testing the sensor with spiked blood samples. The initial pH of the serum measured to be 7.7. To provide blood serum with different pH, blood was extracted from a male sprague-dawley rat and added to tube containing polymer gel for separating serum. After separating the serum, it was divided to four parts and transferred to appropriate sterilized containers, then three pieces of nafion membrane were placed on the top of each part of serum in contact with them.

Since the nafion membrane is just permeable to the protons in solution, we could simulate blood acidosis in the mice blood serum by spiking it with HCL. A drop of 0.03 M hydrochloric acid (HCl) is placed on the top of membrane and at the same time serum was stirred using a magnetic stirrer continuously. The pH was monitored during the time using pH meter. Once the pH of serum reached to the desired value, HCl was removed and the sensor was tested with it.

5.4 Characterization of pH sensor

Graphene foam used in this device contains mono to double layer of graphene grown on copper foam. Hafnium oxide with the thickness of 20 nm was grown on the graphene to form a sensing surface with OH binding sites. Due to the sp2–hybridized crystalline structure of graphene, hydrophobicity and lack of dangling bonds, growth of HfO_2 on graphene using ALD is challenging. Growth of HfO_2 starts at defects or boundaries of bilayer graphene islands which usually form during the growth of monolayer graphene on copper and act as the nucleation sites. Growth continues with forming island of oxide which at sufficient thickness of oxide, merge and form a continuous layer [173].

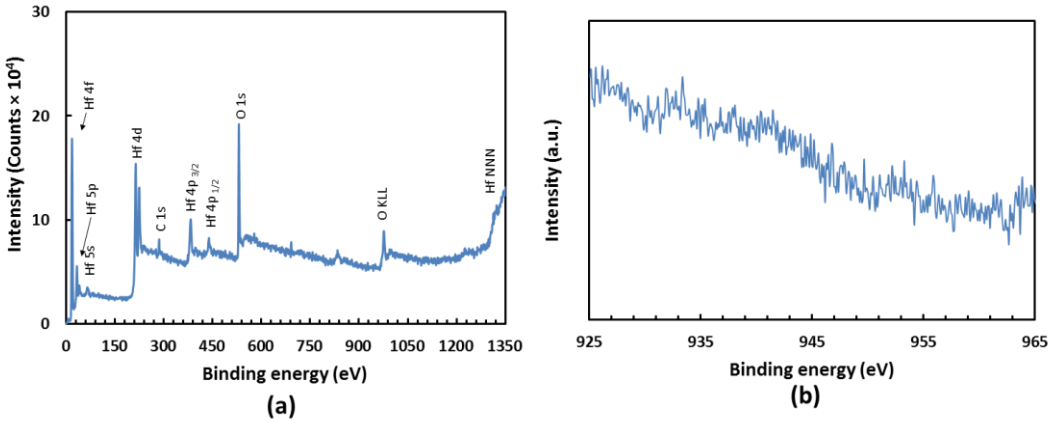

Figure 5.2. (a) The XPS of HfO_2 with 20 nm thickness on the graphene before etching away the copper foam. (b) High resolution XPS spectra of copper.

To investigate the quality and continuity of the HfO_2 grown on graphene, X-ray photoelectron spectroscopy (XPS) of HfO_2 with the thickness of 20 nm grown on the graphene before etching away copper was performed at several random spots. The X-ray spot size was set to be 200 μm. Considering the fact that, the XPS only provides surface information from top 10 to 20 nm of the investigated layer and the thickness of the grown HfO_2, if the oxide forms a continuous layer at top of the graphene no copper peaks should be observed in the XPS results. Figure 5.2 (a) shows the XPS result. The C1s peak reveals the existence of carbon in the oxide layer, attributed to the organic residue from precursor decomposition during growth [174]. Figure 5.2 (b) shows high resolution XPS spectra of copper. As it seen no peak, related to copper was observed, which conforms the continuity of the HfO_2 film on the graphene. The SEM images of graphene coated with 20 nm of HfO_2 layer are shown in figure 5.3. As seen there is a continuous layer of HfO_2 grown all around the graphene. The higher magnification of SEM images reveals the existence of HfO_2 islands which are merged together and form a continuous layer.

To investigate the sensing mechanizem in this device, we have performed the pH sensing using the 3D graphene transistors with and without HfO_2 layer (sensing surface). Before performing experiment contacts were covered with PDMS to minimize the leakage current and a PDMS well were attached on the device around the channel to prevent spreading of the electrolyte on the surface of the device. Experiment was performed in ambient atmospheric pressure and at room temperature. The leakage current was measured to be at least three orders of magnitude less than drain to source current. The results are shown in figure 5.4. Figure 5.4 (a) shows the transfer characteristics of the

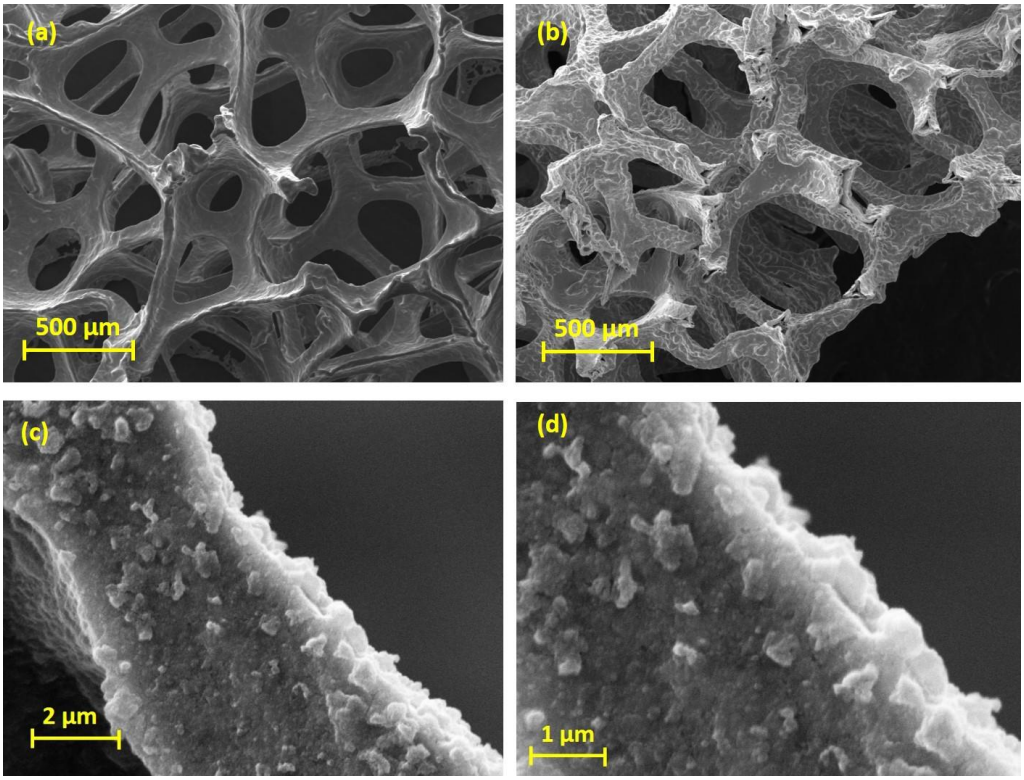

Figure 5.3. SEM images of the graphene foam after growth of 20 nm of HfO_2 on it. (a) The SEM photo of the graphene on the copper foam before growth of HfO_2. (b) After growth of HfO_2. (c) and (d) Different perspective of the HfO_2 grown on graphene at higher magnifications.

transistor gated with different DPBS based pH solution with the pHvalue of 3 to 9. DPBS is a typical isotonic buffered solution which is widely used for biological applications. With increasing pH of the electrolyte, the Dirac point shifts linearly toward more positive voltages while the poition of the dirac point does not change by changing the pH in the device without HfO_2, as it seen in figure 5.4(b). This can be explained using site binding model [170]. Based on this model, depends on the pH of the electrolyte, oxide surface composition and its hydrophilicity, the OH groups on the surface of oxide can be protonate and form OH_2^+, remain neutral, or deprotonate and form O^-. When pH of solution is acidic, OH groups protonate and as a result Dirac point shifts toward more negative voltages and when pH of solution is basic, OH groups

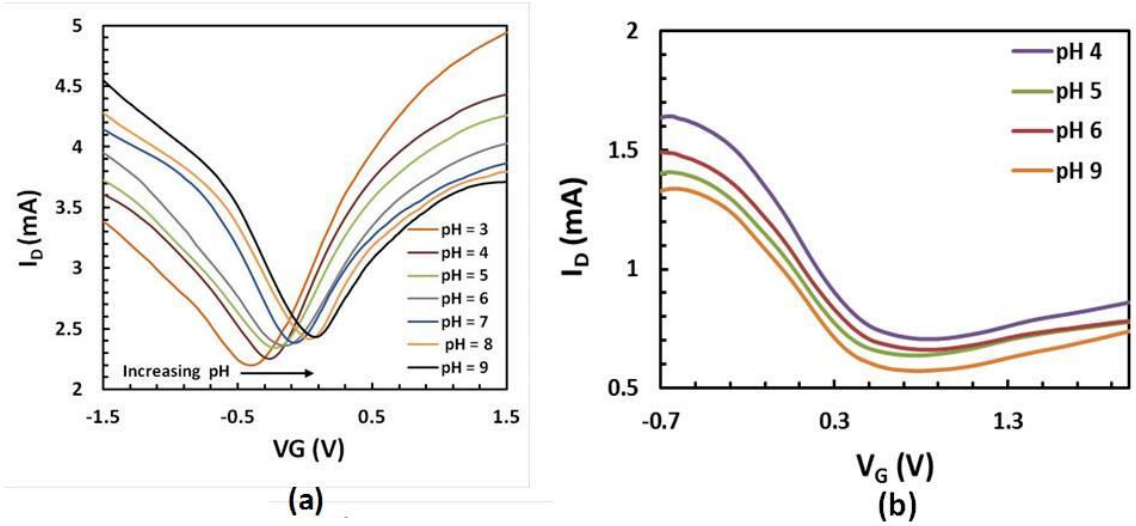

Figure 5.4. (a) Transfer characteristics of transistor with HfO_2 all around the gate as a sensing surface, at different DPBS based pH solutions. (b) Transfer characteristics of transistor without HfO_2, at different DPBS based pH solutions.

deprotonate and Dirac point shifts toward more positive voltages. Therefore, changing the pH of solution will affect the carrier concentration in the graphene. But due to the sp2–hybridized crystalline structure of graphene and lack of dangling bonds the device which is not coated with HfO_2 , it does not show considerable sensitivity to pH. Figure 5.5 (a) shows that the sensitivity of the device to the pH change is linear. The error bars represent the variation of sensitivity for four devices fabricated and tested in the same conditions. The sensitivity of 79 ± 7 mV/pH for this device was deduced. Proposed device can perform sensing in higher ionic strength electrolyte background which has been challenging [159,160,168,175]. We believe that special three dimensional structure of the gate which provides higher surface to volume ratio and using HfO_2 as a sensing surface contribute in beyond Debye length sensing and ultra-sensitivity of this device.

The real time monitoring of the pH was demonstrated and results were shown in figure 5.5 (b). In this experiment the gate to source voltage was fixed at -0.5 V and drain to

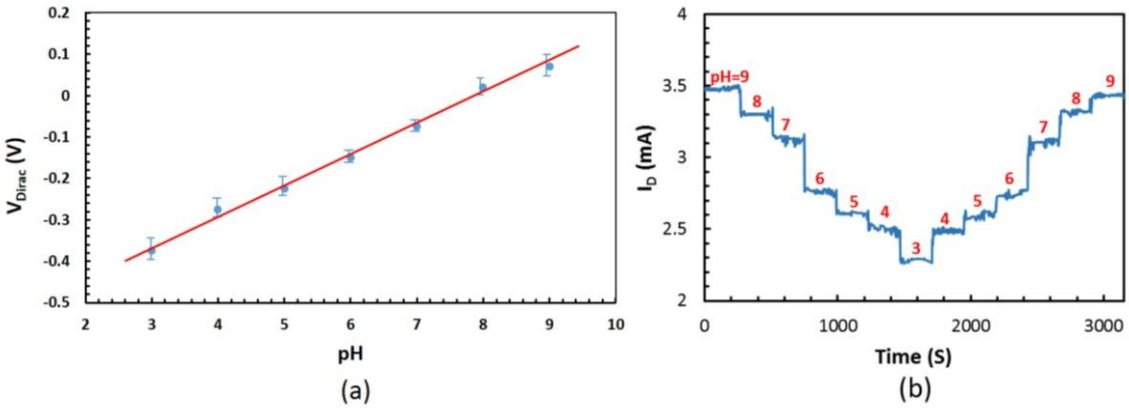

Figure 5.5. (a) Shift of gate voltage at Dirac point for different pH solutions. (b) Real time monitoring of the pH with changing the pH from 9 to 3 and then from 3 to 9.

source voltage on 0.5 V. The solutions with different pH from 9 to 3 and then 3 to 9 were added at the top of the channel of transistor every 240 seconds. The change in the drain current was recorded for different pH solution as a function of time. This result is consistent with the change in transfer characteristics of the transistor in hole conduction regime (V_G= -0.5 V) for different pH of electrolyte. Results show good reversibility for sensing pH from 3 to 9 using presented device.

To investigate the functionality of the sensor in the body fluidic, blood serum of a rat (296±1 mOsm/kg) at four different pH values from 6.4 to 7.7 was used for sensing. Results of sensing the pH of the serum has been shown in figure 5.6. As it seen Dirac point shifts clearly toward the more positive voltages with increasing pH from 6.4 to 7.7. The sensitivity of the device was not effected with increasing of ionic strength of the background electrolyte (almost two times).We attribute it to the very high surface area of the graphene foam in comparison with conventional two dimensional graphene channel coated all around with HfO_2 which forms a lot of site bonds on the surface of the oxide. The serum contains varieties of molecules and ions. To explore that any other factor does not dictate the sensitivity of the device, another set of experiment was performed. In

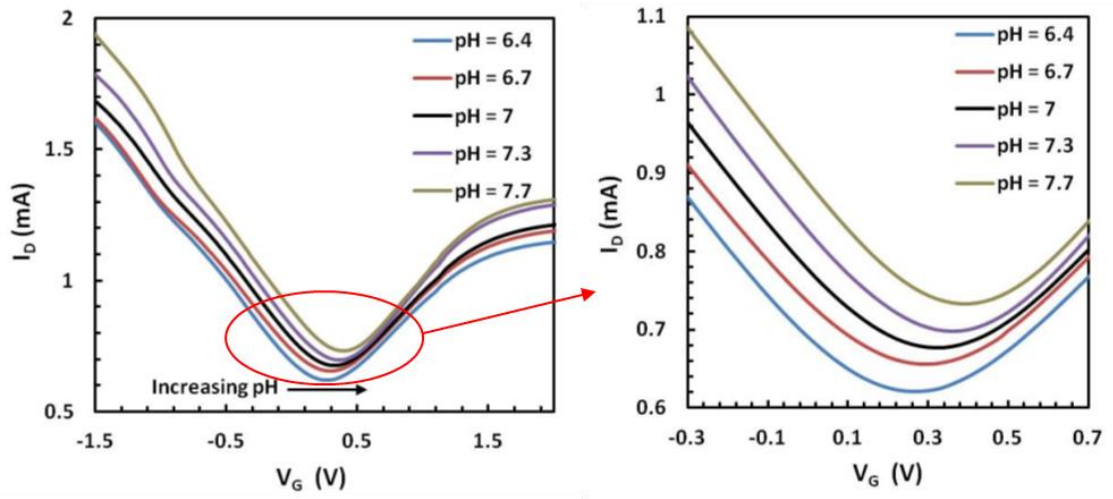

Figure 5.6. Transfer characteristics of the three dimensional graphene transistor at different pH values of blood serum.

this experiment DI water was added into a small container, then a nafion membrane was placed on the top of it and in contact with water. A small drop of HCl/NaOH was added on the membrane and held for a sufficient amount of time to adjust the pH of water to the desire values in the range of 6.5 to 7.8. Once the desire pH is achieved, 200 µL of it was added into the PDMS well attached around the channel of the transistor and measurements were performed. Figure 5.7 shows the transfer characteristics of the device

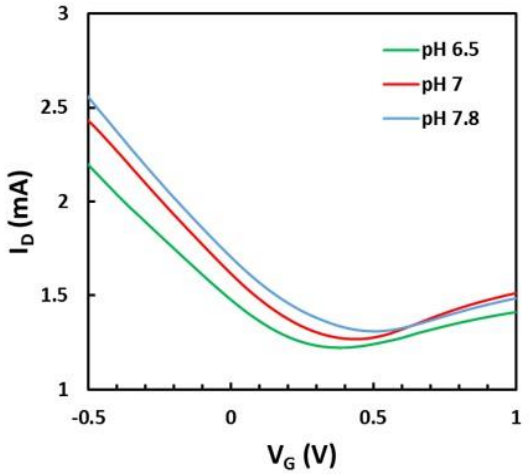

Figure 5.7. Transfer characteristics of the three dimensional graphene transistor based pH sensor for different DI water abased pH solution.

for three different pH values, 6.5, 7 and 7.8. These results show that the sensitivity of the device does not change by replacing the serum with DI water, therefore we can conclude that no considerable electrochemical reaction which affect the sensitivity of the sensor occurs in this device during sensing pH in blood serum.

5.5 Summary

In conclusion, highly sensitive pH sensor based on three dimensional liquid gated graphene transistor was presented. The channel of this device consists of graphene foam covered all around with HfO_2 as a sensing surface. Sensing is performed with protonizing or deprotonizing of the OH groups at the surface of the oxide, depends on the pH of electrolyte. We have shown that this device can perform its functionality at high ionic strength of background electrolyte like as DPBS and blood serum with the sensitivity of 79 ±7 mV/pH. This device has potential to be used for real time monitoring of the pH in biological environment and blood acidosis diagnosis. We believe that three dimensional structure of the sensor provides high surface to volume ratio and as the result high sensitivity and beyond Debye length sensitivity.

CHAPTER 6

Three Dimensional Graphene Transistor for Strain Sensing

In this chapter, strain sensing using three dimensional graphene transistor is presented and the fabricated sensor characterization is discussed. Graphene foam shows promise for strain sensing application due to its exceptional electrical and mechanical properties. The outline of this chapter is as follows.

First, the motivation and background behind this work is presented. Second, the fabrication process is described and the performance of the graphene transistor based strain sensor and its potential applications are discussed. Detailed experimental results are presented which validate the functionality of the sensor device.

6.1 Motivation and background

Strain sensors have various applications in structural health monitoring of civil infrastructure, monitoring of orthopedic and tissue implants, and for fundamental biological studies of cells/tissues and organs and broadly for studying material fatigue in both synthetic and natural systems [176-182]. Conventional strain sensors based on

semiconductors and metals are low cost and highly sensitive but they are usually unidirectional and could be quite bulky. In comparison, using nano-materials for strain sensing has the advantage of high resolution, scalability, high sensitivity and multi-directionality. Varieties of nano-materials such as zinc oxide nanowires, zinc-stannate ($ZnSnO_3$) nanowires, carbon nanotubes (CNT), graphene layers, flakes and nano-sheets have been used for strain sensing with different values of gauge factor (GF) (a quantitative factor which is used to define the sensitivity of sensor to the applied strain) between 0.06 to 10^6 [183-187,74]. Graphene has impressive mechanical stability, high carrier mobility and electrical conductivity. Furthermore it is transparent, biocompatible and nonhazardous which make it an attractive material for strain sensing especially for biological application. Graphene film based strain sensors usually have higher gauge factor than metal silver nano-wire based sensor with gauge factor of 2, comparable with conventional metal based strain sensor with gauge factor of 2 to 5 and much lower than ZnO nanowire (116), CNT (1000-2600) and $ZnSnO_3$ nanowires (3750) based strain sensors [164,165,188-190]. However, one of the biggest advantages of graphene is that it can be processed to form micro-ribbon, micro and nano-flakes, graphene ripples, woven graphene and graphene foams which show their structure-dependent mechanical and electrical properties. It has been shown that graphene film based strain sensors have the gauge factor of 0.11 to 6.6, rippled graphene, 2, micro-ribbon, 9.49, nano-graphene film 300 and graphene woven fabric 10^3 to 10^6 [169,184,191,192]. The scalability of the gauge factor is highly desirable because different gauge factor is needed for diverse applications. The high gauge factor sensors are suitable for low strain applications while low gauge factor sensors are appropriate for high strain applications. However there is a

tradeoff between elasticity and gauge factor in graphene based strain sensor, due to mechanism of the sensing in these type of sensors, which is based on formation of cracks during stretching. For example, the highest gauge factor reported for graphene based strain sensor is gauge factor of woven graphene which is about 1000 for up to 6% strain and increases to 10^6 by increasing the strain up to 10%, while the super elastic rippled graphene shows linear increase of the gauge factor with increasing strain up to 30% but it has just the gauge factor of 2 [171,184]. In the other words in the conventional film based gauge strain sensor, more of elasticity leads to smaller gauge factor and vice versa.

The use of multilayer free standing graphene foam for strain sensor has been reported. It has been shown that graphene foam/PDMS composite is highly stretchable and it can be strained up to 90% [73]. However, multilayer graphene foam grown on nickel used in graphene foam/PDMS composite is highly conductive, therefore; it does not show very high gauge factor at low strains. But it has a big advantage of existence of interconnected graphene network of foam in three dimensions which can provide multiple parallel pathways for electrons and holes for conduction, giving fault-tolerance even in presence of cracks and discontinuity due to strain.

To keep the advantages of interconnects in graphene foam and also achieve high sensitivity at low strains, we have used few-layer of graphene to implement a transistor that provides strain sensitivity. In this dissertation, we have discussed the implementation of a strain gauge sensor based on three dimensional graphene foam. The effect of strain on the transfer characteristics of the ionic liquid gated three dimensional transistor was presented. This sensor was gated through the ionic liquid using Ag/AgCl electrode. The results show that the conductivity of the channel decreases with increasing the strain

which results in decreasing the overall drain to source current. Our results shows graphene maintains its semimetal behavior under high strain (up to 30%) and the transistor still shows the ambipolar behavior. Proposed strain sensor shows the gauge factor of 1.5, 16.6 and 71.3 at 0.5%, 20% and 30% strain respectively which is higher than conventional two dimensional graphene based strain sensors. In the following sections, the theory, functionality, fabrication and performance of this device will be discussed in detail.

6.2 Theory

In this section, the mechanisms of sensing strains using flexible geometries are discussed. One of the biggest categories of the strain sensors which can be made flexible are piezoresistors. In this type of strain sensors one exploits the material's inherent mechanical-to-electrical transduction, which could be captured as a change in resistance under strain. In piezoresistive semiconductors, strain causes change in the bandgap changing the carrier density of the material and as a result impacts the carrier mobility and consequently changes its conductivity. Theoretical study predicts that uniaxial strain opens bandgap in graphene but this hypothesis has not been proven experimentally yet.

Large group of flexible strain sensors are based on strain gauge materials. The conductivity of strain gauges change by reversible physical deformation when they are stretched below their permanent deformation point. Gauge factor (GF) is a quantitative factor which is used to define the sensitivity of sensor to the applied strain and it is defined as

$$GF = \frac{\Delta R}{\varepsilon R_0} \qquad (6.1)$$

Where ΔR is change in the resistance due to strain, R_0 is initial resistance and ε is strain which is defined as $\Delta L/L_0$. The parameters, ΔL and L_0 are change in the length due to strain and initial length respectively [193]. It is widely believed that this mechanism is the dominant mechanism of the sensing in the graphene films and composites based strain sensors [163,172].

Another group of the strain sensors are made of nano-particles, nano-wires nanotubes, nano-plates and nanowire composites. The operation of these sensors can be explained using percolation. Here usually conductor fillers are embedded in insulated polymer matrix. In the presence of strain and stress, embedded conductor particles rearrange the connection path and as the result conductivity between two end on the matrix changes. Based on the particle geometry and aspect ratio, the resistance either increases or decreases. Increasing the resistance by applying compressive strain is called negative pressure coefficient and it happens when the fillers are low aspect ratio particles such as metal powders. The opposite effect is called positive pressure coefficient which the resistance decreases by applying compressive strain. The strain sensors made from high aspect ratio fillers such as CNTs and graphite nano-sheets show positive pressure coefficient in the presence of compressive strain.

Nano-particles such as graphene nano-sheets embedded within stretchable substrate can be also used as a strain sensor. The mechanism of sensing in this group of sensors is quantum tunneling of electron between nanometer gaps of nanoparticles. Local electric field enhances at the sharp edge of nanoparticles and provides the possibility of the tunneling for electrons [173]. In these type of sensors, huge change in resistivity is observed as results of small strain. The probability of the tunneling is strongly dependent

on the shape and size of the particles.

6.3 Device fabrication and experimental setup

Fabrication of the three dimensional graphene based strain sensor was performed using similar fabrication process, explained in section 4.3.2, with few differences. In this device PDMS was used as a substrate instead of glass, contacts were formed by deposition of 30nm of Ti and 220 nm of Au films and the graphene foam used in this device consists of few layers of graphene. Graphene foam which is used as a strain gauge material is liquid gated using ionic liquid to function as a transistor. To investigate the functionality of the three dimensional liquid gated transistor based strain sensor, device was gated by adding ionic 1-Butyl-3-methylimidazolium hexafluorophosphate (BMIM-PF6, 98%) and was strained using customized set up. The transfer characteristic of the device with different percentages of strain was measured using semiconductor parameter analyzer (HP Agilent 4156A). The photo of the customized setup has been shown in figure 6.1. The device was held using two clips connected to a moving stage with micrometer movement precision. The sensor was gated through the ionic liquid using

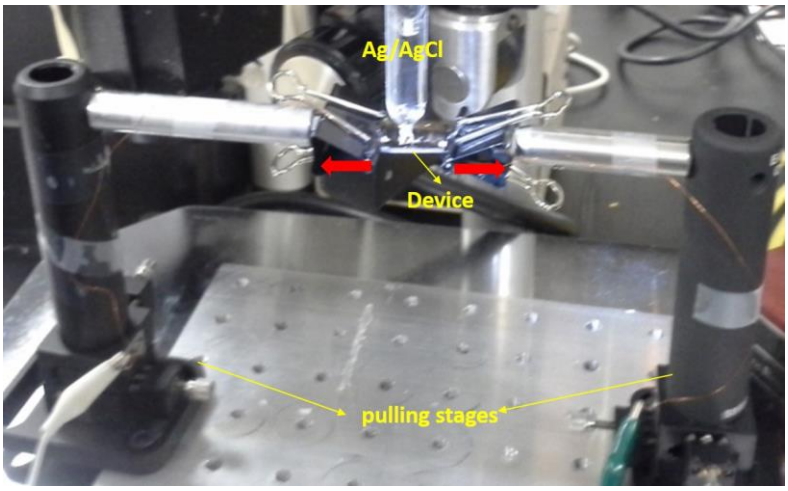

Figure 6.1. Photo of the customized set up for measuring the transfer characteristics of the three dimensional graphene transistor based strain sensor.

Ag/AgCl electrode.

The cyclic tests of strain gauge were performed using Instron 3369, interfaced with PC-based data acquisition and analysis software, LABVIEW, to record data and for processing to investigate a stability and repeatability of the response to the strain in the presented device. The schematic and the photo of the system are shown in figure 6.2.

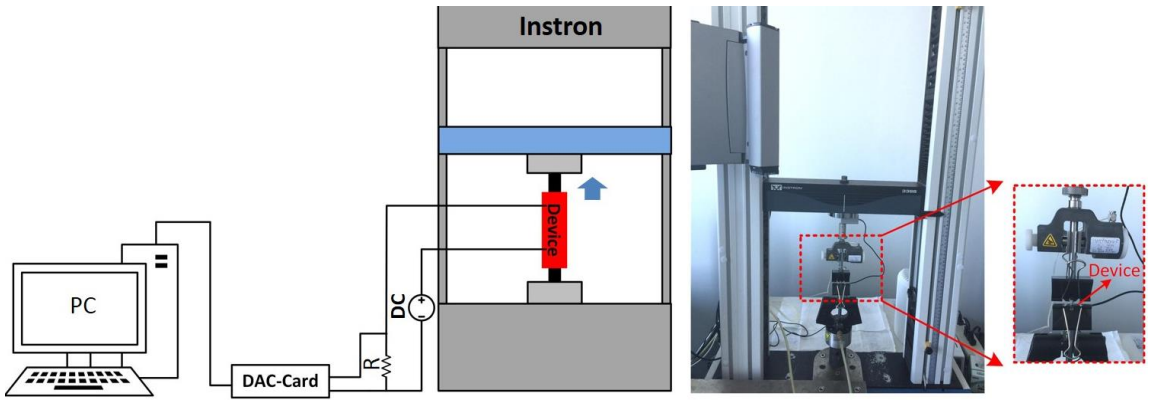

Figure 6.2. (a) Schematic of a cyclic measurement set up for strain sensing. (b) The photo of the instron with loaded sample.

6.4 Results and discussion

Using transistor for sensing strain has the advantage of inherent amplification of the response by applying voltage between gate and source. We have investigated the effect of strain on the functionality of the 3D liquid gated graphene transistor. Figure 6.3 shows the transfer characteristics of the device for different percentages of the strain.

As seen, the conductivity of the channel decreases by applying different percentages of strain from 0.5% to 30%. This is due to the deformation of the graphene and the formation of cracks and discontinuity in the channel of the transistor. As a result, the current through device decreases by applying strain and returns to the initial value by releasing it. Due to strain, cracks may form partially in some of the strips in the

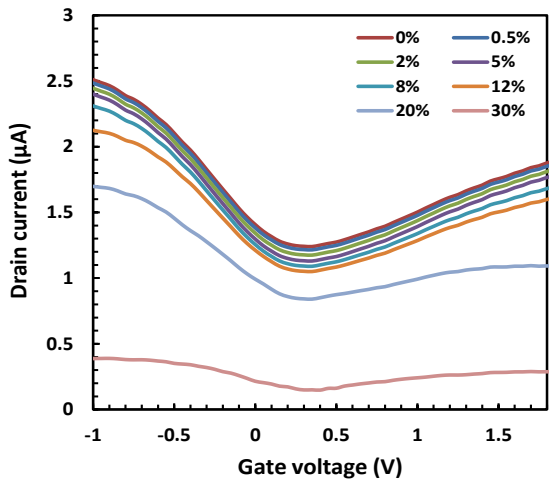

Figure 6.3. Transfer characteristics of the three dimensional graphene transistor based strain sensor at different percentages of strain.

graphene foam.

The 3D form of the graphene strips interconnects provides many different possible pathways for electrons in the presence of cracks which leads to the stable and robust functionality of the device at high percentages of strain. As long as the applied strain force is below the point where discontinuities and deformation become permanent, the change in the resistivity is reversible. Figure 6.4 shows the cyclic measurement under saw-tooth wave strain for different percentages of strain. Our results show that the response and recovery in graphene are stable and repeatable even under high percentage of strain which represents the potential application of this device for sensing both low and high level of tensile strain. Therefore the channel of this device behaves as a variable resistance under the strain which the resistance of it increases with increasing strain. However one should notice that if strain is applied to the gold contacts, cracks will also form in the metals and propagate faster than in graphene due to a greater difference in stiffness and rigidity of the PDMS and the metal. This causes exponential response at very beginning of applying strain (around 1%). Beyond which the resistance

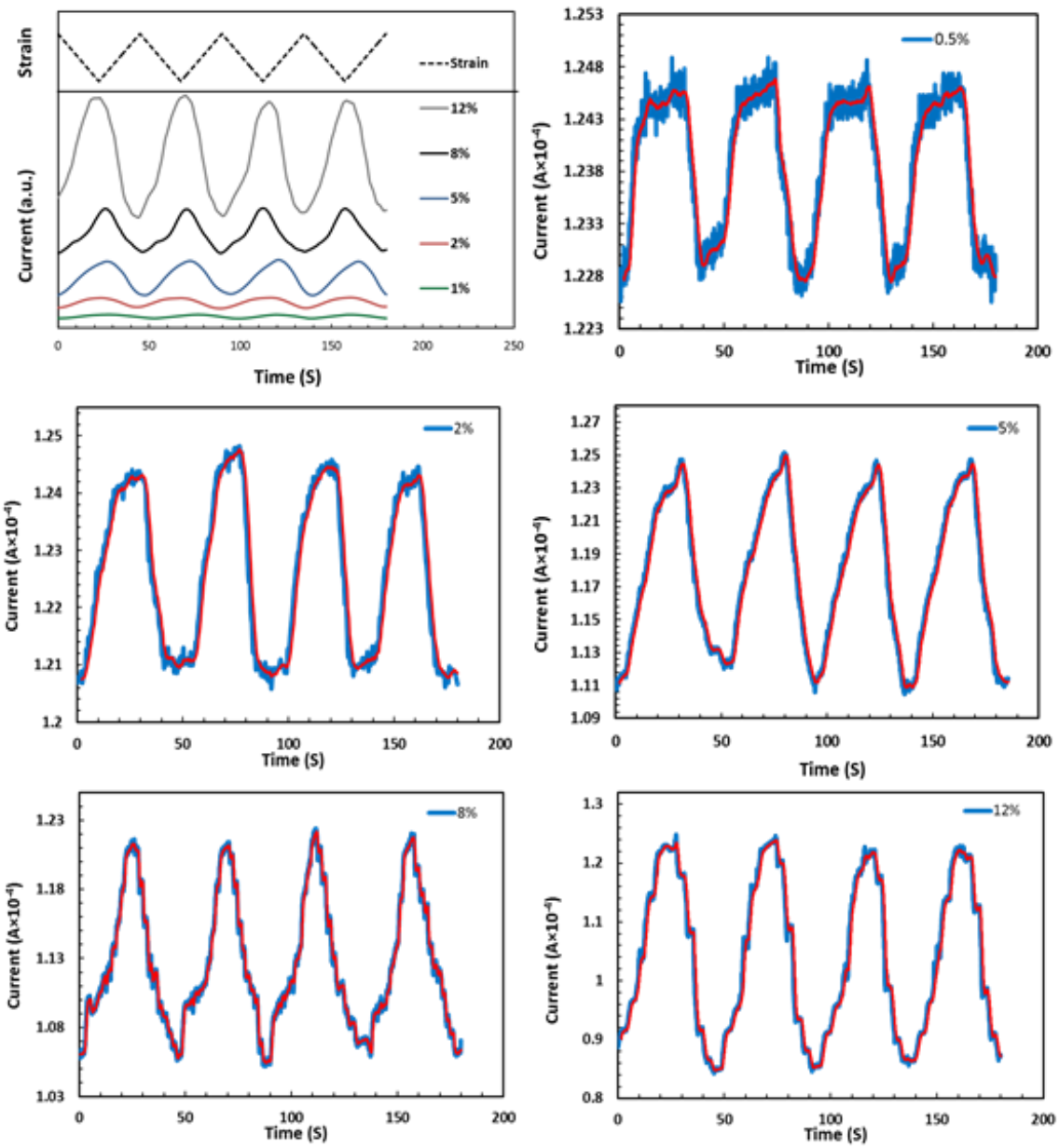

Figure 6.4. Cyclic testing of the three dimensional graphene based strain sensor for different percentage of strain between 0.5% to 12%.

remains almost constant and then decreases exponentially and reaches to the initial value with the release the strain. Figure 6.5 shows the cyclic measurement when device is clipped right after the gold contacts, at two ends of the PDMS. Due to the application of strain at the contacts and the fast formation and propagation of cracks in the metal, the

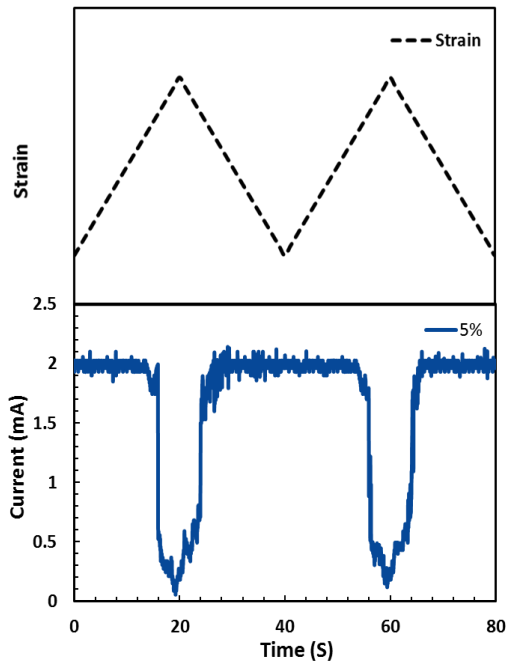

Figure 6.5. Cyclic testing of the three dimensional graphene based strain sensor, when device is clipped at two ends, after gold contacts, for 5% percentage of strain.

response of the device to the strain is not linear. It is important to point that the response of the graphene to the strain is different than the combination of the responses of the gold and graphene to the strain, as it is shown in figure 6.4 and 6.5. This can cause huge error in the results and extracted sensitivity of the device.

Figure 6.6 shows the gauge factor of the device versus different percentages of strain. The device shows the gauge factor of 1.5 at 0.5 %, 5.5 at 1% to 12 %, 16.6 at 20% and 71.3 at 30% of strain. The gauge factor increases linearly up to 12 % and exponentially from 12% to 30%. Although it has been shown that the interconnected graphene network can be modeled as a combination of the series and parallel resistors of value that results in exponential increase of the resistance due to formation of cracks but there is an order of magnitude difference between experimental and calculated results, this raises the probability of associated tunneling effect at higher values of tensile strain through

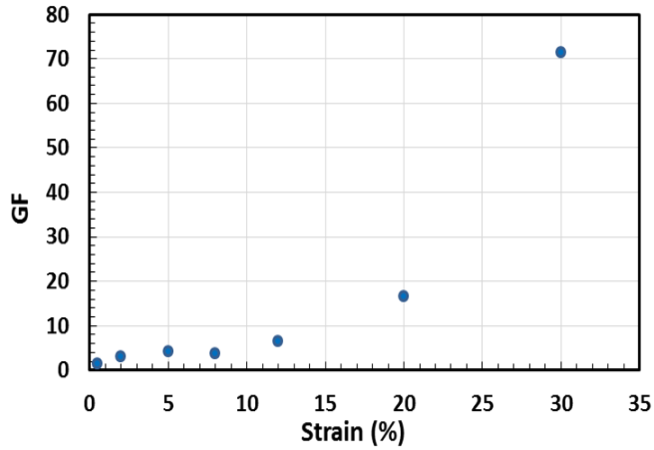

Figure 6.6. Gauge factor of the strain sensor versus strain for different percentages of the strain.

nanometer gaps graphene caused by the strain [163].

The result of cyclic measurement at different frequencies, 0.022 Hz, 0.2 Hz and 0.5 Hz, at 0.5 % of the strain is presented in figure 6.7. This result shows the similar response to the strain at different frequencies which indicates, the device performance is repeatable and stable and it is not dependent to the measurement speed.

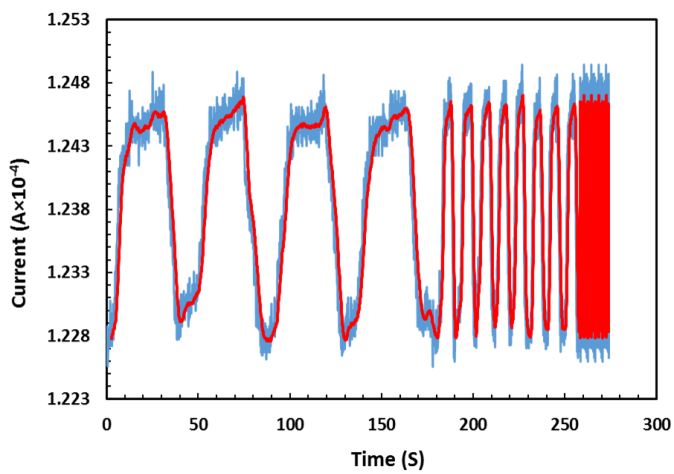

Figure 6.7. Cyclic measurement of the strain sensor at different speeds for 0.5% of tensile strain

6.5 Summary

In conclusion, the proposed three dimensional graphene foam based strain sensor shows the high sensitivity at both low, 0.5%, and high strain, 30%. The gauge factor is

1.5 at 0.5%, 5.5 at 1% to 12 %, 16.6 at 20% and 71.3 at 30% of strain. The device shows the stable and repeatable functionality over different frequencies of saw-teeth strain wave between 0.022 Hz to 0.5 Hz tested in this work. The effect of applying strain to the contacts has been studied.

The 3D structure of graphene provides many different possible pathways for electron or hole carriers in the presence of discontinuity or cracks in some of the graphene strips of the foam in case of high applied strain. Based on our results, the presented device is robust and stable under high strain which is due to the special three dimensional networked structure of graphene. The mechanism of sensing in this device is mainly based on the formation of defects and deformation of the graphene which increases the resistance of the graphene. There is also a possibility of associated tunneling effect of electron through the gaps between cracks at high tensile strain.

CHAPTER 7

Three dimensional graphene for recording the electrical activity from electrogenic cells

High conductivity, biocompatibility and three dimensional network structure of the graphene foam, make it a promising candidate for multi-functional bio-electronic interface which can perform different tasks such as sensing, cell stimulation and cellular studies at the same time and also serve as a non-planar scaffold for cell growth. Various electrogenic cells such as cardiomyocytes, neuron and skeletal muscle cells can be expected to grow within the scaffold. In this chapter, preliminary results of our study on the growth of different electrogenic cells lines such as HL-1 cardiac cells, and PC-12 neuronal cells on the three dimensional graphene foam have been studied. In the beginning, a background and theory behind this work is presented, following which we discuss the experiments and the results.

7.1 Motivation and background

In this study, we have grown diffrerent cell lines on the graphene foam and investigated their viability. We have used HL-1 cell line to investigate the functionality of

the graphene foam for recording electrical signal from cells. HL-1 cells are derived from AT1 mouse artrial cardiomyocyte tumor at 1998 [194]. Unlike other cardiomyocytes, these cells contract and maintain cardiac electrophysiological, morphological and biochemical characteristics after many times passaging. The pattern of gene expression of HL-1 cells is similar to the adult mice artrial myocytes. For better understanding of the device function and cells-graphene interface, one should review the electrophysiological mechanism of myocytes.

All human cells are surrounded by bilayer membrane known as plasma membrane, consisting of various phospholipids and proteins. The phospholipid molecules contain hydrophobic lipid chains and hydrophilic phosphate head as shown in figure 7.1 [196]. In contact with aqueous solution the hydrophilic phospholipid molecules arrange into a double layer. The hydrophilic phosphate head is placed on the outer side of double layer and lipid chains at the inner side of it. Membrane proteins act as the channels through the membrane and function as pumps which facilitate the passive and active transport of various ions and molecules to the cells and out of it. Most of the human cells have nucleus which contains genetic materials. Internal environment of cells is called endoplasm and consists of water, enzymes and organelles such as mitochondria,

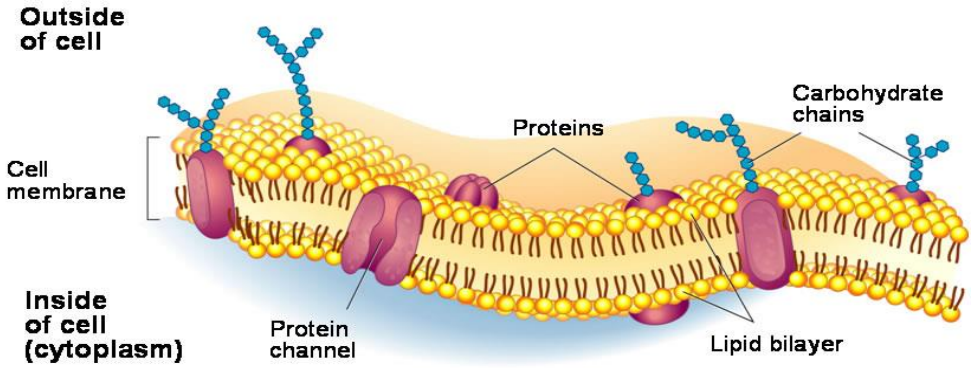

Figure 7.1. Mammalian cell membrane contains phospholipids, and protein [195].

ribosome, lysosome, etc. [197]. The cell membrane of cardiac myocytes is called sarcolemma. Inside of the cell membrane of myocytes there are a nucleus and many numbers of mitochondria to provide adenosine triphosphate (ATP) which transfers chemical energy to the cells for continues beating and other cellular functions (see figure 7.2). The contraction of myocytes is possible because of the existence of contractile protein called actin and myosin and regulatory proteins known as troponin and tropomyosin [196]. Actin and myosin are enclosed in the network of sarcoplasmic reticulum which is equivalent to the endoplasmic reticulum in other cells. Sarcoplasmic reticulum continues through actin and myosin and forms transverse tubules (T tubules) wrapping myofilament bundles as it can be seen in figure 7.2. The action potential propagates in extracellular fluids continue to flow in T tubules. Cardiac myocytes settle end to end at the intercalated disk at Z-line. The gap junction between myocytes provides path way with low resistance to facilitate propagation of the signal from one cell to neighboring one. At rest, there is a potential difference between two sides of the cell membrane which is known as the resting potential.

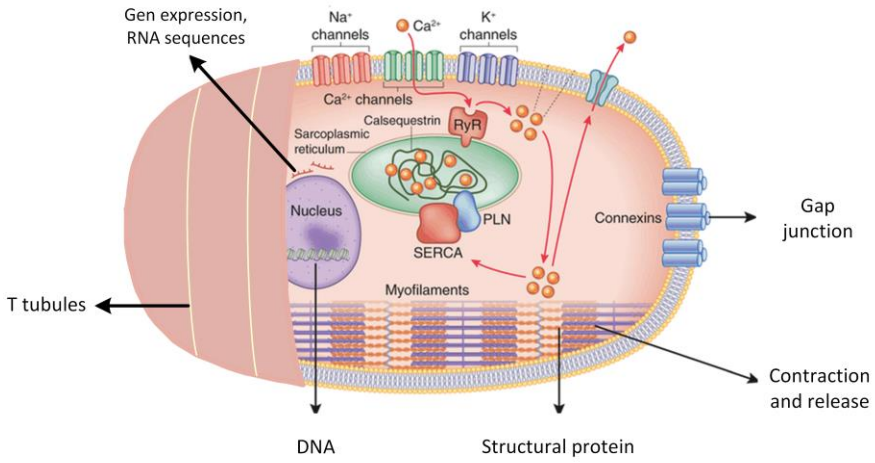

Figure 7.2. The T tubule, sarcolemma, mitochondria and nucleus in a cardiomyocyte [197].

At rest, inside of the membrane is more negative than outside. The resting potential of myocytes is about -90 mV. The cardiomyocytes fall in two categories, pacemakers and non-pacemakers. The non-pacemaker cells show a prolonged action potential and plateau, but the pacemaker cells do not have long resting period and they do not show long plateau phase. The plateau phase in non-pacemaker cells last about 300 ms. Figure 7.3 shows the action potential phases in the non-pacemaker cardiomyocyte. First phase known as the depolarization phase which leads to the membrane potential change from -90 mV to 10 mV, due to decreasing and increasing the permeability of the membrane to the potassium and sodium ions respectively. In the second phase the permeability of the membrane to the Na+ ions decreases and partial repolarization happens. With increasing the cell membrane permeability to the calcium ions the third phase of the action potential occurs. Higher concentration of calcium ions inside of cell membrane causes prolongation of the action potential and plateau. At the end of the plateau phase the permeability of the membrane to the calcium decreases and the plateau preserves by exchanging three sodium ions into the cells with one calcium ion to outside, through

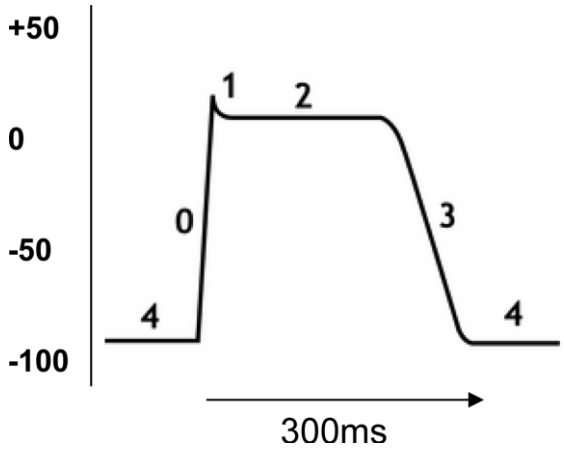

Figure 7.3. The non-pacemaker cardiomyocyte action potential shows 5 different phases; phase 0, depolarization; phase 1, partial polarization; phase 2, plateau phase; phase 3, repolarization; phase 4, resting potential [197].

sodium-calcium exchanger. In the fourth phase, calcium channels are inactivated and following potassium ions into the cells ends plateau. The fifth and last phase is resting membrane potential which the potential of the membrane returns to the initial value of -90 mV. The next action potential occurs just when the previous one is completed. This process lasts about 300 ms for non-pacemaker cells. The pacemaker cells action potential does not have the second and third phases (phase 1 and phase 2). Increasing the permittivity of the membrane to the calcium through T-type channel (transient type), and decreasing its permittivity to the potassium and sodium causes rising the action membrane potential to threshold voltage in the first phase of action potential in non-pacemaker cells. Once the voltage reaches threshold, L-type calcium channels are opened and potential increases to maximum and depolarization happens. In the next phase, the permittivity of the membrane to the potassium increases and re-polarization happens as shown in figure 7.4.

There are different methods to record action potential of cardiomyocyte such as optical techniques, using voltage sensitive dyes, patch-clamp and recording pacemaker

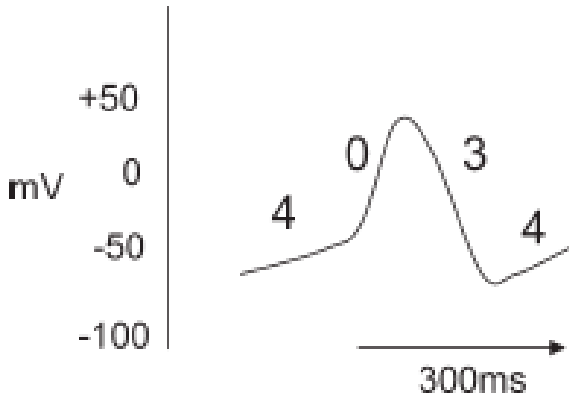

Figure 7.4. The action potential of pacemaker cardiomyocyte is not including phases 1 and 2. Phase 4 occurs due to increasing calcium and sodium ions concentration in the cells. Phase 0 is depolarization and phase 3 is repolarization [197].

current [198-200]. Both intracellular and extracellular action potential recording have been reported in the literatures [201-204]. In this dissertation, the extracellular recording using 3D graphene networked has been investigated; therefore the focus of this section is on the principle of extracellular recording.

Conventionally, two dimensional planar arrays of electrodes are used to record the extracellular electrical activity from the cells [205,206]. In vitro extracellular signal recording can be performed by growing cells directly on the top of the planar array or by bringing electrodes in vicinity of cells grown on another platform [207,208].The working mechanism of such devices is sensing changes in local electric field potential during cell activity. To perform in vivo signal recording, multi-electrode arrays (MEA), the array of metal electrodes, are widely used. One of the most important parameter for the signal coupling between cells and MEAs is the low input impedance of the electrode. The input impedance is dependent on the surface topology and the type of material used for electrodes [209]. Another approach for recording the signal of cell is using a field effect transistor (FET), which has the advantage of intrinsic amplification of any signal coupled to its gate [208,209].

The interface of electrode with cells can be described using point-contact model [210]. The structural and circuit component model of a cardiomyocyte on a planar two dimensional electrode can be simplified as a combination of cell, cleft area and electrode which are modeled as a set of series and parallel capacitors and resistors as shown in figure 7.5. The cleft area between the cell membrane and the electrode is filled with the background medium. One side of cell membrane, in contact with electrode, forms cell

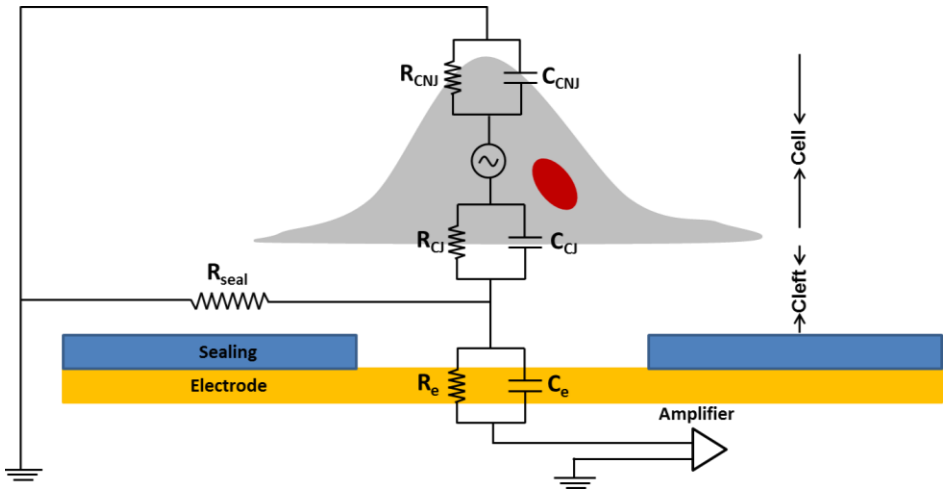

Figure 7.5. The structural and circuit component model of a cardiomyocyte on a planar two dimensional electrode [212].

junctional resistance, R_{CJ}, and capacitance, C_{CJ}, and the other side which faces bathing medium, forms cell non-junctional resistance, R_{CNJ}, and capacitance, C_{CNJ}. The surrounding medium in the cleft area forms sealing resistance, R_{seal}. Action potential of the cells as a result of ions exchange, changes membrane potential and causes a current flow. This current flows between non-junctional and junctional membrane. The potential change over sealing area modulates the voltage of electrode. The electrical coupling between a cell and electrode are included the membrane oscillations, synaptic potentials and action potential coupling. The membrane oscillation and synaptic potential signal occur at much lower frequencies than the action potential signal [211].

Conventional electrodes used for electrogenic action potential recording have so far been metals. The biggest advantage of metal electrodes are accessibility and simple fabrication process, but there are several drawback to using metal electrode for many bio applications such as low charge injection, mechanical mismatch with biological tissues and cells it is interfaced with, foreign body response, electrochemical instability, high

noise level and non-transparency [210,212]. Graphene is a promising candidate for this purpose due to biocompatibility, remarkable mechanical stability, flexibility, good electrochemical stability and transparency [136,213,214].

In this chapter, the utilization of the three-dimensional graphene foam as a scaffold for growing electrogenic cell lines and as electrode for recording of the action potential of cells in-situ during the growth is discussed. Our results show excellent biocompatibility of the proposed device which allows long term growth of the cells and maintaining their electrophysiological and morphological characteristics while providing direct sensing of key electrophysiological parameters.

7.2 Cells culture

Three types of cell lines, PC-12, Schwann cells and HL-1, are cultured on the graphene foam to investigate the biocompatibility and viability of these cell lines on three dimensional graphene as a cell scaffold.

PC-12 cell line was established in the year1976 by Greene from transplantable rat adrenal pheochromocytoma. This cell line responds to the nerve growth factor (NGF) and after one week starts to multiply and extend its branching. This cell line can be serially cultured and be used as a model system for neurobiological studies [215].

Schwann cells are satellite cells in the peripheral nervous system which surround motor nerve terminals and axons. Axons peripheral nerve in mammalians can be as long as meter or more which are surrounded with Schwann cells. These cells support axons and in myelinated axons perform isolation and elaborate the myelin sheath of the myelinated nerves which is necessary for propagating and conducting electrical signal in the nerves. They are also involved in nerve development and regeneration. Schwann cells

have attracted a lot of interests in spinal cord injury therapy especially because of their roll in regeneration of nerves and myelination [216-218].

HL-1 cells, derived from mouse AT1 mouse artrial cardiomyocyte tumor in the year 1998. This cell line unlike other cardiomyocytes, contract continuously and maintain cardiac electrophysiological, morphological and biochemical characteristics after many times passaging. The pattern of gene expression of HL-1 cells is similar to the adult mice artrial myocytes and therefore, they can be used for the study of cardiac function [195]. In the following sections we describe the cell culture procedure of these three cell lines.

7.2.1 PC-12 and Schwann cells culture

The procedure of culturing PC-12 and Schwann cells are very similar but the growth mediums are different. The PC-12 media culture consists of Dulbecco's modified Eagles medium (DMEM), 10% fetal bovine serum (FBS), 5% horse serum and 100 U/ml penicillin and 100 mg/ml streptomycin [119]. The Schwann cells are maintained in medium consisting DMEM, with 10% FBS, 100 U/ml penicillin and 100 mg/ml streptomycin [220]. The cells are reserved at 37° C and 5% CO_2 after seeding. To culture the cells on the graphene foam, the media culture is aspired from the flask containing the precultured, confluent cells. Then 5 mL trypsin EDTA (0.025%) is added to the flask and kept for 5 minutes at 37° C. In the next step 5ml of the cell medium is added to the cell suspension and transferred to a spinning tube. Cell suspension is centrifuged for 2 minutes at 1500 rmp. The upper liquid is removed and remained cells at the bottom of tube, are suspended in 1mL of medium. The cell suspension is diluted with cell medium to achieve the final concentration of 10^4 cell/mL. Finally 200 µL of this suspension is added at the top of the graphene foam and placed in incubator for 12 hours to help the

cells to settle before adding extra medium. After 8 to12 hours the old medium is removed and several mL of new medium depends on the size of well plate is added. The medium is exchanged every 2 days.

7.2.2 HL-1 cell culture

HL-1 cells, derived from mouse atrial tumors (gift from Dr. William Claycomb,Department of Biochemistry and Molecular Biology, the Louisiana State University School of Medicineand obtained via collaboration with Prof. Lauren Black from Biomedical Engineering Department at Tufts University) [195]. Cells were maintained in Claycomb Medium (Sigma-Aldrich, St. Louis, MO) which is supplemented with 10% FBS, 100 μg/mL penicillin/streptomycin, 2 mM L-glutamine, and 0.1 mM norepinephrine. The norepinephrine is essential to maintain the beating cardiomyocyte phenotype. Before seeding cells (from passages 40-45), graphene foam was uninfected and then coated with 0.02% gelatin/ 0.005% fibronectin and incubated for 8-12 hours before adding cells on the device. The process of seeding cells on the graphene is the same as explained in previous section.

7.3 Growth of PC-12 and Schwann cells on 3D graphene

To investigate the biocompatibility of the 3D graphene and cell viability, multilayer graphene grown on the nickel foam and monolayer graphene grown on copper foam using CVD method were transferred on the glass substrate and used as the scaffold for cell growth. The free standing multilayer graphene foam and monolayer graphene grown on copper foam was purchased from Graphene supermarket. The process of the etching copper is described in chapter 3. After transferring the graphene foam on the glass

substrate, it was sterilized by keeping the device in 70% ethanol for 30 to 40 minutes and drying with blowing air. After growing cells they were stained with calcein AM (Life Technologies, Carlsbad, CA) to investigate the cell viability.

Figure 7.6 shows the photos of the Schwann cells grown on free standing 3D multilayer graphene foam with initial concentration of 10^4 cells/mL, 24 hours and 18 days after seeding. Cells were stained with Calcein AM dye. Results show the ability of the

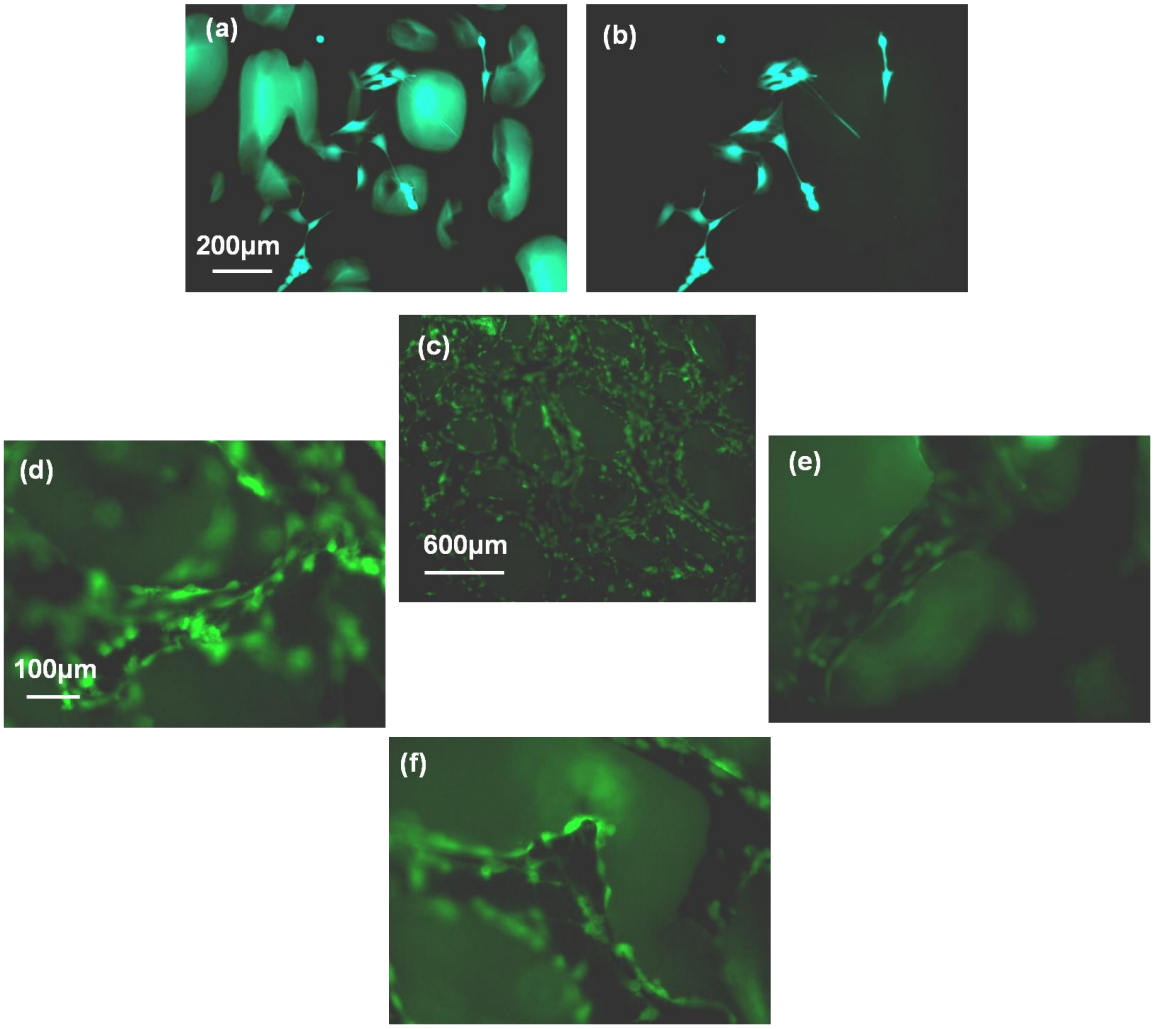

Figure 7.6. Fluorescent images of Schwann cells grown on 3D free standing multilayer graphene foam. Cells are stained with calcein AM; (a) photo was taken 24 hours after seeding cells with a combination of the white and fluorescent light; (b) fluorescent photo of cells 24 hours after seeding; (c) fluorescent photo of cells 18 days after seeding; (d) to (f) photos with higher magnification. (d) to (f) have same scale bar.

cells to adhere and grow all-around of the graphene strips in the foam. It was noticed that cells are able to continue the growth for longer period of time on the 3D graphene compare to the cell culture flask. We attribute this to the natural three dimensional structure of graphene which provides higher available surface area for cells to grow.

PC-12 cells were cultured on monolayer graphene foam grown on the copper foam. After etching copper and sterilization of graphene transferred on glass substrate cells

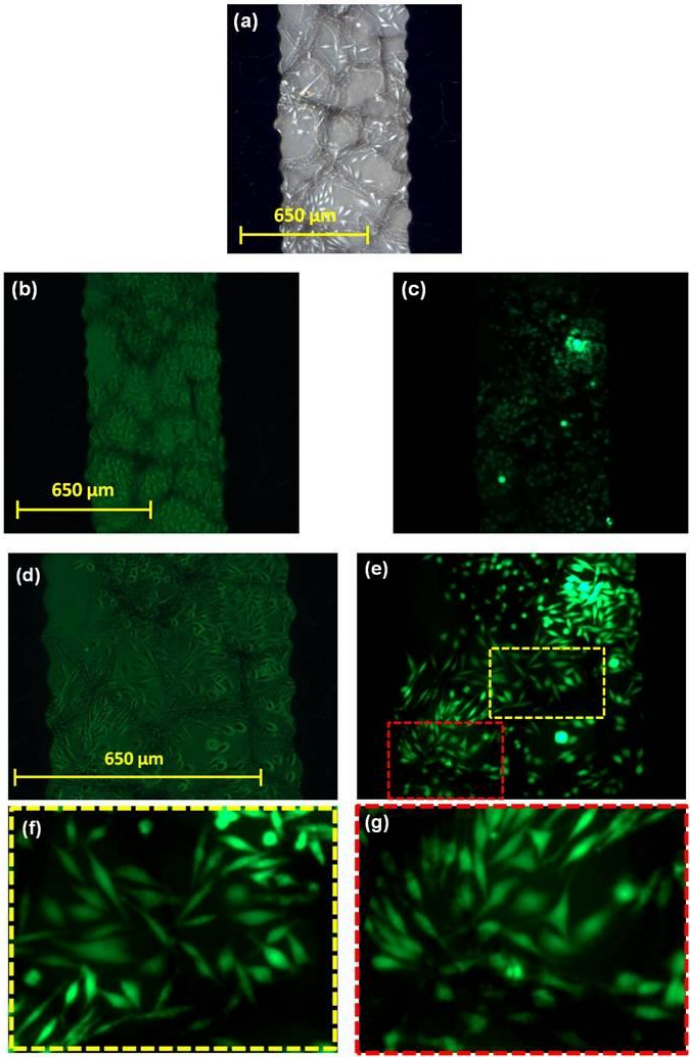

Figure 7.7. Optical and fluorescent images of the PC-12 cells grown on monolayer graphene foam. Cells are stained with calcein AM. (a) Optical photo of the cells 24 hours after seeding. (b) Photo was taken using the combination of white and fluorescent light from the cells 6 days after seeding. (c) Fluorescent photo of cells 6 days after seeding; (d) to (g) are figures 7.7(b) and (c) with higher magnification.

were cultured on it. Figure 7.7 shows the optical and fluorescent images of the cells stained with Calcein AM, 24 hours and 6 days after seeding cells. Results shownontoxicity of monolayer graphene foam and cell viability. As seen in figure 7.7, cells grow all over the graphene strips in the foam showing good biocompatibility.

7.4 HL-1 cells viability on monolayer graphene

The HL-1 cell line was cultured on graphene foam (one to two layers) after sterilization. The surface in contact with this cell line was treated with gelatin-fibronectin to help the cells to grow and contract. The effect of extracellular matrix on the growth of HL-1 has been studied in literature [221]. Figure 7.8 shows the photo of cell cultured in cell culture flask and on the graphene 18 hours after seeding. It was observed that the more numbers of the cells adhere to the graphene than the polymer in the first 18 hours. Cells started contracting after reaching confluency usually 3 days after seeding. In this specific sample, cells were contractile 3days after seeding and they continue to contract up to 9 days which shows the viability of HL-1 cells grown on 3D monolayer graphene. Photos of cells at different days of growth and up to 8 days are shown in figure 7.9. As

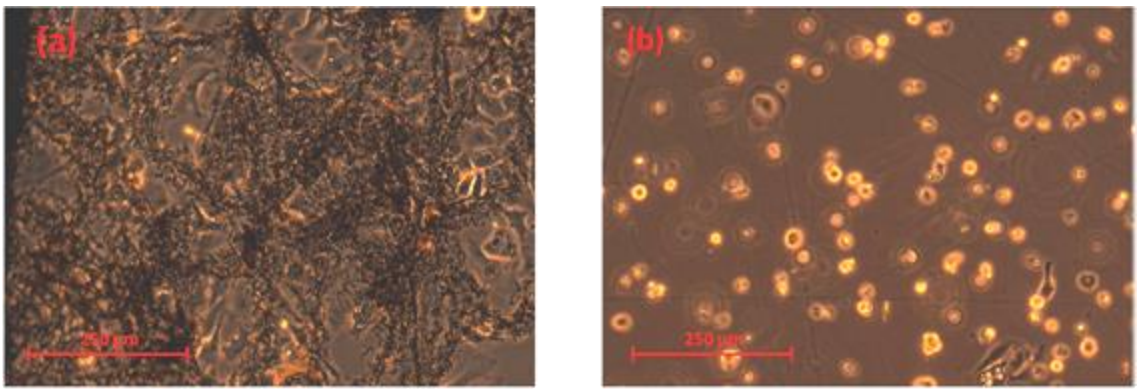

Figure 7.8. HL-1 cells 24 hours after seeding; (a) grown on graphene foam; (b) on polymer (culture flask).

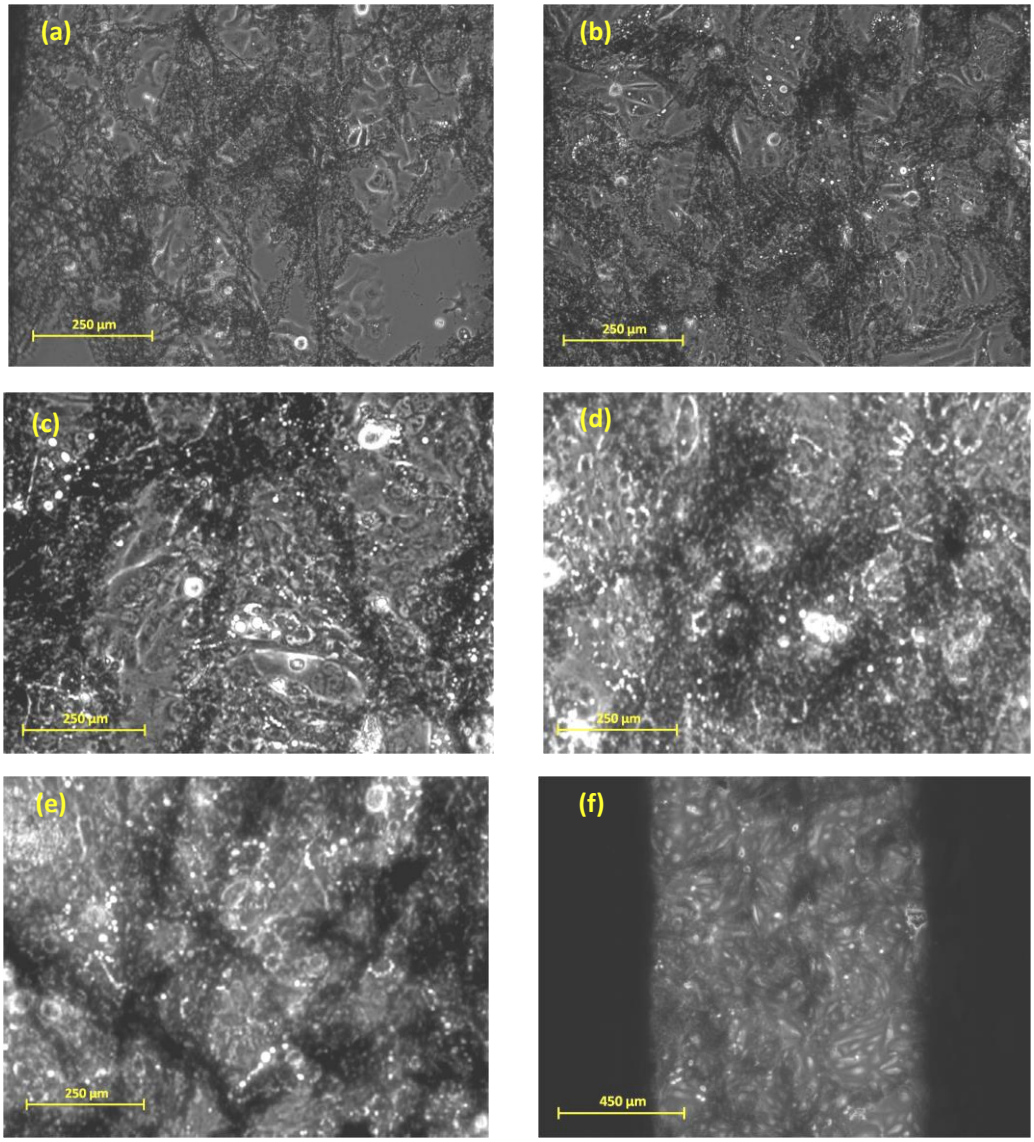

Figure 7.9. HL-1 cell line cultured of the graphene foam. (a) 24 hours, (b) 4 days, (c) 5 days, (d) 6 days and, (e) 8 days after seeding. (f) Overall view of the device 8 days after seeding cells in lower magnification.

seen, the cells grow all-around of graphene and covered it completely.

7.5 Measurement of the calcium transient and electrical cell signaling

The Fluo 4AM (Life Technologies, Carlsbad, CA) was utilized to visualize and measure calcium transients when the islands of the HL-1 cells were formed. The fluorescent indicator fluo-4 acetoxymethyl (AM) (Life Technologies, Carlsbad, CA) was used at a

concentration of 10 μL/mL of Fluo-4 AM (10 × 50 μg, F14201, Invitrogen). Culture plates were wrapped in aluminum foil to prevent light contamination then placed in the incubator for 20 minutes to allow the fluo-4 AM binding to calcium. The fluo-4 AM solution was then removed and replaced with Tyrode's solution containing 140 NaCl, 5 KCl, 5 HEPES, 1 NaH_2PO_4, 1 $MgCl_2$, 1.8 $CaCl_2$ and 10 glucose (pH 7.4) adjusted with NaOH. All salts and buffers were purchased from Sigma-Aldrich. After an additional 20 minutes in the incubator, the cells were imaged in the Tyrode's solution using Metamorph software on an Olymus IX-81 microscope equipped with a fluorescent camera. Analysis of the calcium transients was performed using region analysis in the Metamorph software. Figure 7.10 shows the results of calcium transient measurement. When fluo-4 AM enter to the cells it bounds to calcium ions which results in the intensity change of the green light monitored and reordered with microscope and software. Two spots, one island of cells and the other one substrate, are selected to compare the results of photo-signal recording. As it is shown, the change in the concentration of the calcium in the cells due to their beating, causes the change in the photo-intensity.

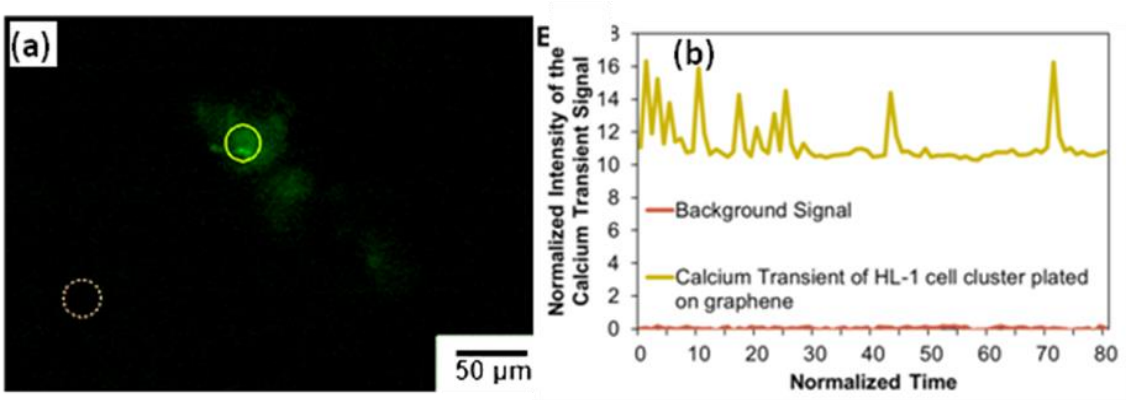

Figure7.10. Calcium transient measurement in HL-1 cells plated on graphene. (a) Identification of the regions used to determine the background (red/white dash) and beating cells (yellow circle). (b) Normalized change in fluorescent intensity in for spontaneously beating HL-1 cells plated on graphene mesh.

The extracellular electrical recording of the cell was performed using the 3D monolayer graphene foam device. The device consists of graphene foam in the middle of two Ti/Au electrodes at two ends. Electrodes are covered with a layer of PDMS to prevent the physical contact between cell and medium with electrodes. The electrical circuit was used to amplify the signal from the cells and filter the noise (see figure 7.11). The device was grounded at the source terminal as well as the medium. The bio-potential resulting from the cell activity was measured across the device. The voltage at the drain terminal was first coupled with a sub-Hertz high pass filter, consisted from capacitors and resistors, to remove the DC offset. The remaining AC signal was buffered with an op-amp (OP177) in unity gain feedback configuration. This stage was followed by an RC twin-T notch filter (with a potentiometer for tuning) to remove 60Hz line noise as well as a first order RC filter with a 2kHz cut-off frequency to remove high frequency interference from the incubator. The remaining signal was amplified by 10x. The filter and amplify stage were repeated for a total amplification of 10000x for the in- band signal.

The output was fed into a National Instruments DAQ card for analysis in Labview.

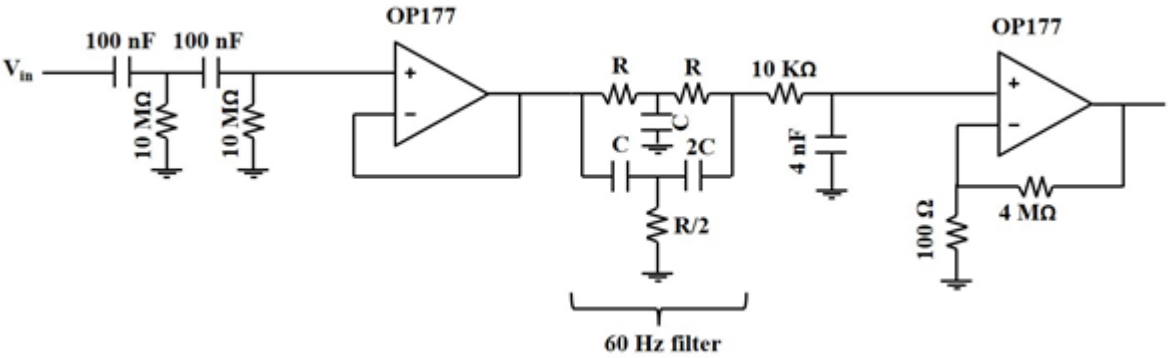

Figure 7.11. Schematic of the circuit for amplifying the signal from cells.

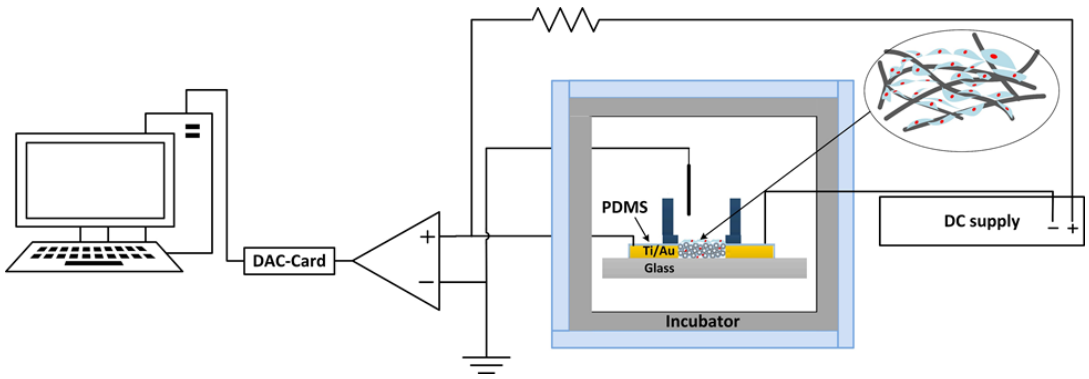

Figure 7.12. Schematic of the system for recording the electrical signal from cells.

Schematic of the system has been shown in figure 7.12. During beating cells the total extracellular concentration of the K^+, Na^+ and Ca^{2+} ions around the graphene and inside the medium are changed which result in the change of the conductivity of the graphene and consequently change in the current following through the graphene and dropping voltage between two contacts. The change in the voltage is amplified using the circuit and recorded. Result of recording the signal from cells has been shown in figure 7.13. This shows that the graphene foam can be the appropriate electrode for recording of the electrical activity from the electrogenic cells.

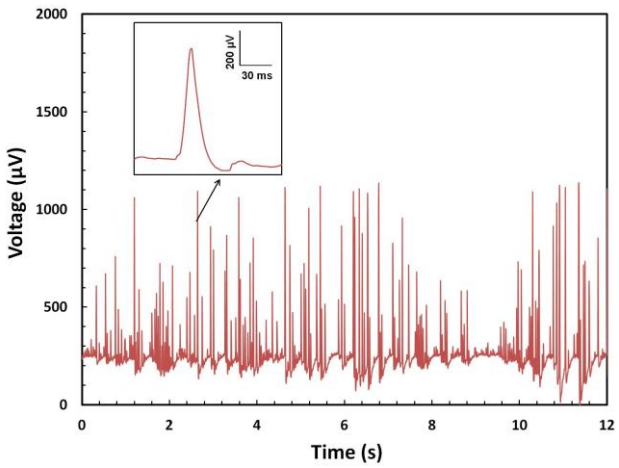

Figure 7.13. Electrical signal of HL-1 cells grown on graphene foam recorded using same scaffold.

7.6 Summary

In summary, it was shown that the mono to double layer and multilayer free standing graphene foam are promising as a scaffold for growing different types of electrogenic cells. Recording the electrical activity of the HL-1 cells was performed using mono to double layer graphene foam. Based on presented results in this chapter graphene foam can be used as a multifunctional scaffold for cells. Based on our other work where we have used graphene foam based transistor for sensing chemical, and mechanical activity one can see the possibility of graphene foam serving as a multi-functional device for monitoring electrical, chemical and mechanical activity from the cell, while at the same time serve as a true three dimensional scaffold for cells.

CHAPTER 8

Conclusion and Future Work

8.1 Conclusion

We have proposed the first three dimensional graphene transistor and introduced some of its applications in sensing and bioelectronics. We have also introduced robust and electrochemically stable, graphene based microfluidic device for dielectrophoretic (DEP) trapping of mammalian cells and lysing the cells using high DC electric field. It has been shown that the two dimensional graphene can be used as an electrochemically stable electrode in biological environment in presence of high DC electric field.

The fabrication process and the electrical characteristics of two different versions of three dimensional graphene transistor, liquid gated and ionogel gated, were presented. The channel of liquid gated transistors is made of mono to double layer graphene grown on the copper foam using CVD. The Long channel (600 to 1200 µm) three dimensional graphene transistor shows consistency in electrical characteristics between devices.

The ionogel gated version of three dimensional transistor with the channel made of few layers of graphene foam, was fabricated on flexible Parylene film with the thickness

of 28±2 μm. This transistor shows ~26.72 times more current capacity than equivalent two dimensional graphene transistor.

Using liquid gated three dimensional graphene transistor, sensing pH in high ionic strength medium (higher than 100 mM) was performed. By adding a 20 nm of HfO_2 all-around of the 3D graphene gate, as a sensing surface, the sensitivity of a 79 mV/pH at high ionic strength medium and blood serum is achieved. We attribute the high sensitivity and beyond Debye length sensitivity of this device to the special three dimensional structure of the graphene and existence of a sensing surface in this device.

A strain gauge sensor based on the presented transistor was implemented which shows 0.5% to 30% with the gauge factor of 1.5 to 71.3 at different percentages of strain. This device shows mechanical robustness due to the network structure of the foam which provides many possible pathways for carriers in the presence of cracks.

Multilayer free standing graphene foam and mono to double layer of graphene foam were used as a nonplanar scaffold for growing PC-12, Schawnn and HL-1 cell lines. The cells grown on three dimensional graphene maintain their viability. The HL-1 cells were grown on the mono to double layer three dimensional graphene foam and their electrical signal was recorded using graphene scaffold during growth.

8.2 Publications

8.2.1 Journals

1. S. K. Ameri, P. K. Singh, S. Sonkusale, “Liquid gated three dimensional graphene network transistor”, Carbon, 79, 572–577, 2014.

2. S. K. Ameri, P. K. Singh, S. Sonkusale, “Utilization of graphene electrode in transparent microwell arrays for high throughput cell trapping and lysis”, Biosensors and

Bioelectronics, 61, 625–630, 2014.

3. S. K. Ameri, P. K. Singh, M. R. Dokmeci, A. Khademhosseini, Q. Xu and S. Sonkusale, “All electronic approach for high-throughput single cell trapping and lysis with electrical impedance monitoring”, Biosensors & bioelectronics, Biosensors and Bioelectronics 54, 462–467, 2014.

4. Y. Zilberman, S. K. Ameri, S. R. Sonkusale, “Microfluidic optoelectronic sensor based on a composite halochromic material for dissolved carbon dioxide detection”, Sensors and Actuators B: Chemical, 194, 404–409, 2014.

5. P. K. Singh, S. K. Ameri, L. Chao, M. N. Afsar and S. Sonkusale, “Flexible broadband metamaterial absorbers for millimeter wave frequencies”, Progress In Electromagnetics Research, 142, 625-638, 2013.

6. S. K. Ameri, S. R. Sonkusale, “Three dimensional graphene transistor for ultra-sensitive ph sensing directly in biological media”, submitted.

7. S. K. Ameri, P. K. Singh, A. D'Angelo, M. J. Panzer, S. R. Sonkusale, “Flexible three dimensional graphene transistors with ionogel dielectric demonstrates low operating voltage and high current capacity” Submitted.

8. S. K. Ameri, P. K. Singh, W. Stoppel, L. Black, S. R. Sonkusale, “Three dimensional graphene network scaffold for electrogenic cells electrical recording”, to be submitted.

9. M. Akbari, S. Bagherifard, Y. Chen, M. Comotto, G. Fu, , E. Lesha, L. Serex, A. Tamayol, Y. Zilberman, S. K. Ameri, M. R. Dokmeci, S. R. Sonkusale, and A. Khademhosseini, “Flexible pH-sensing hydrogel fibers for monitoring of wound condition”, to be submitted.

8.2.2 Conferences and meetings

1. S. K. Ameri, P. K. Singh and S. R. Sonkusale, “Stretchable three dimensional graphene foam based transistor for strain sensing”, MRS, fall 2014.

2. S. K. Ameri, P. K. Singh and S. R. Sonkusale, "Three dimensional monolayer graphene foam for ultrasensitive pH sensing", 56th Electronics Materials Conference (EMC), June 2014.

3. S. K. Ameri and S. R. Sonkusale, “Graphene based platform for high throughput cell trapping and lysis”, World Congress on Biosensors, (Biosensors) May 2014.

4. S. K. Ameri, P. K. Singh and S. Sonkusale, “Transparent micro-fluidic setup for electric field manipulation of cells”, MRS Fall Meeting, 2012.

5. K. Park, S. K. Ameri and S. R. Sonkusale, “A dielectrophoretic lab-on-chip platform with 3D reconfigurable electrodes for label-free detection of microorganisms, International conference on label-free technologies, 2015.

6. K. Park, S. K. Ameri and S. R. Sonkusale, “CMOS dielectrophoretic lab-on-chip platform for manipulation and monitoring of cells,” EMBC 2015.

7. Y. Chen, S. K. Ameri and S. R. Sonkusale, “Functionalized optical fiber sensor platform for detection of gastric ammonia and carbon dioxide for early screening of stomach disease” International conference on label free Technologies, 2015.

8. S. K. Ameri, P. K. Singh and S. R. Sonkusale “Large area gold nanoparticle based optical absorbers”, MRS, Fall 2013.

9. P. K. Singh, S. K. Ameri, and S. R. Sonkusale, “Metamaterials on fabrics using the paint process”, MRS, Fall 2013.

10. Y. Zilberman, S. K. Ameri and S. R. Sonkusale, “Microfluidic optoelectronic sensor array for detection of dissolved co2 based on halocromic dye-doped polymeric

microbeads", IEEE sensors, 2013.

11. K. Park, S. K. Ameri and S. R. Sonkusale, "A CMOS Dielectrophoretic LoC platform for bio-impedance detection," BioCAS 2015.

8.2.3 Invention disclosure

1. Three dimensional graphene transistor

8.3 Future work

The following improvement can be made to enhance the functionality of presented device:

- The current version of this device is very large. The channel length of this transistor is selected bigger than average pore size of the graphene foam to keep the consistency between devices. Using a graphene foam with few micrometer pore size for the channel of this transistor can feasible the realization of shorter channel length transistor with very high current capacity and improve the sensitivity of sensors made based on it.
- Since we have shown the utility of a three dimensional graphene foam transistor for electronics, chemical and mechanical sensing applications, the next steps are to combine two or more of these functionalities in one device for multimodal sensing. This will be highly desirable in biological applications.
- Due to biocompatibility of a proposed device, flexibility, ability to work in liquid and high ionic strength environment and also mechanical robustness, it has great potential to be integrated and used as an implantable device for monitoring the electrical activity of tissue and chemical sensing of its surrounding environment.

- Considering novelty of the proposed device there are a lot of possible electronics and bio electronics applications which can be further investigated.
- The structural model which is proposed here is based on many approximations on the geometry of the device, improving the structural model of this device using an appropriate software can help to better understand the fundamental physics aspects of the proposed device and lead to finding more possible applications for it.

Appendices

Appendix A

A.1 Graphene crystalline structure

Graphene has hexagonal crystalline structure with two sub lattices. Figure A.1 (a) shows sublattice A indicated with green balls and sublattice B indicated with red balls. The vectors $\boldsymbol{a_1}$ and $\boldsymbol{a_2}$ are primitive translation vectors and the gray area is a unit cell. The unite vector has been marked as $\boldsymbol{\tau}$ which connects two neighboring atoms from two different sublattices A and B. The Brillouin zone and reciprocal lattice vectors are shown in figure A.1 (b). Every corner is corresponding to a Dirac point [222].

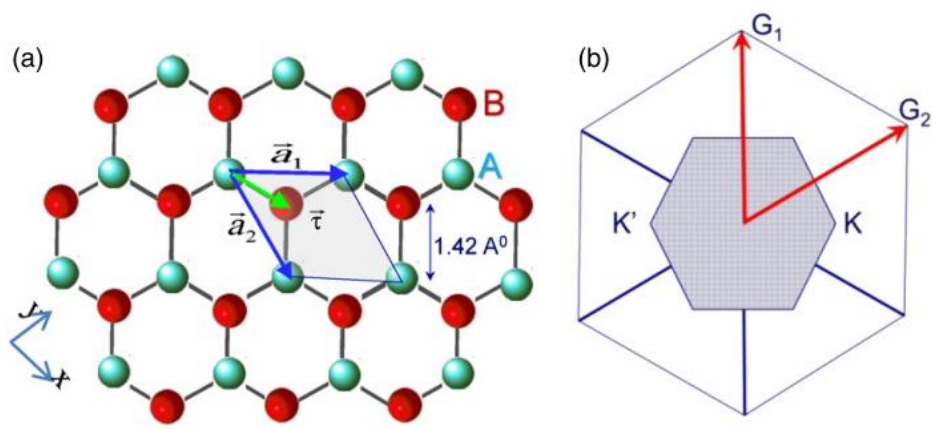

Figure A.1. (a) The hexagonal crystalline structure of graphene. (b) The first Brillouin zone of the graphene [222].

Appendix B

B.1 Circuit for amplification of cell signal and suppressing noise

The operational amplifier used in this circuit (OP177) was purchased from Anaglog Devices. The simplified schematic of this circuit has been shown in figure B.1. This low noise amplifier has open loop gain of 12 V/μV over ±10 V output range and operate at the range of temperature between -40°C to 85°C [223].

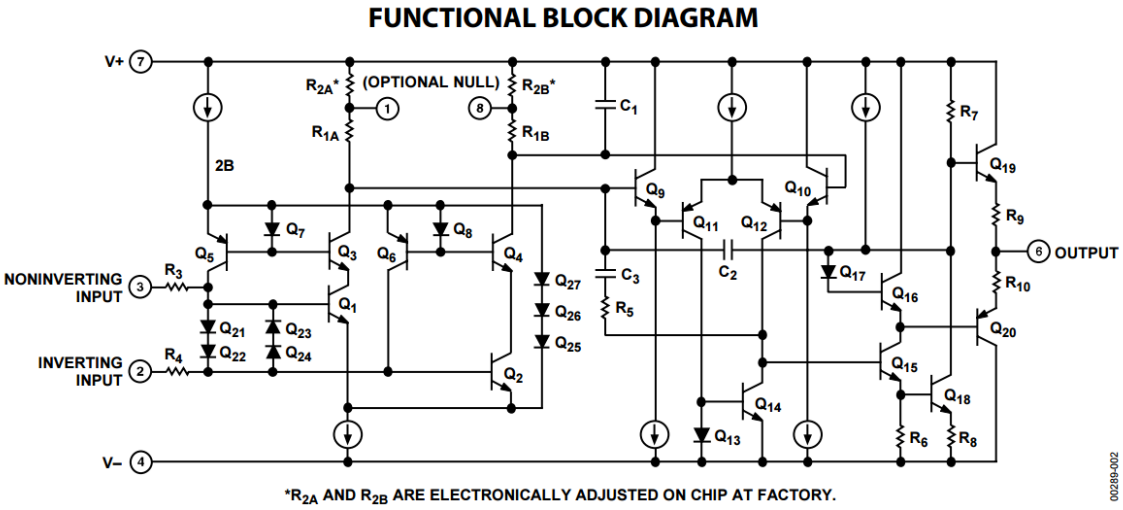

Figure B.1. The simplified circuit schematics of operational amplifier OP177 [223].

References

[1] S-J Han, A. V. Garcia, S. Oida, K. A. Jenkins, W. Haensch, “Graphene radio frequency receiver integrated Circuit,” Nature Communications 2014, 5, 3086.
[2] N. Mohanty, V.Berry, “Graphene-based single-bacterium resolution biodevice and DNA transistor: interfacing graphene derivatives with nanoscale and microscale biocomponents,” Nano Lett. 2008, 8, 4469–4476
[3] L. M. Zhang, Z. Lu, Q. Zhao, J. Huang, H. Shen, Z. Zhang, “Enhanced chemotherapy efficacy by sequential delivery of siRNA and anticancer drugs using PEI-grafted graphene oxide,” Small 2011, 7, 460–464.
[4] L. M. Zhang, J. Xia, Q. Zhao, L. Liu, Z. Zhang, “Functional graphene oxide as a nanocarrier for controlled loading and targeted delivery of mixed anticancer drugs. Small 2010, 6, 537–544.
[5] S. R. Ryoo, Y. K. Kim, M. H. Kim, D. H. Min, “Behaviors of NIH-3T3 fibro-blasts on graphene/carbon nanotubes: Proliferation, focal ad-hesion, and gene transfection studies,” ACS Nano 2010, 4, 6587–6598.
[6] O. N. Ruiz, K. A. Fernando, B. Wang, N. A. Brown, P. G. Luo, et al., “Graphene oxide: a nonspecific enhancer of cellular growth,” ACS Nano 2011, 5, 8100–8107.
[7] Y. Shao, J. Wang, H. Wu, J. Liu, I. A. Aksay, et al., “Graphene based electrochemical sensors and biosensors: a review, “Electroanalysis 2010, 22, 1027 – 1036.
[8] P. R. Wallace, "The Band Theory of Graphite," Physical Review 1947, 71, 622.
[9] K. S. Novoselov, A. K. Geim, S. V. Morozov, D. Jiang, Y. Zhang, S. V. Dubonos, I. V. Grigorieva, A. A. Firsov, “Electric field effect in atomically thin carbon films,” Science 2004, 306 ,666-669.
[10] D. Reddy, L. F Register, G. D. Carpenter, S. K. Banerjee, “Graphene field-effect transistors,” J. Phys. D: Appl. Phys. 2011, 44, 313001.
[11] A. H. C. Neto, F. Guinea, N. M. R. Peres, K. S. Novoselov, A. K. Geim, “The electronic properties of graphene,” Rev. Mod. Phys. 2009, 81, 110-162.
[12] H. Liu, Y. Liu, D. Zhu, “Chemical doping of graphene”, J. Mater. Chem., 2011, 21, 3335–3345.
[13] Y. Zhang, Y.-W. Tan, H. L. Stormer, P. Kim,” Experimental observation of the quantum Hall effect and Berry’s phase in graphene,” Nature 2005, 438, 201-204.
[14] M. I. Katsnelson, K. S. Novoselov, A. K. Geim, “Chiral tunnelling and the Klein paradox in graphene”, nature physics 2006, 2,620-625.
[15] H. F.-Moran, “Single crystals of graphite and mica as specimen support for electron microscopy”, J Appl Phys 1960,31,1844.
[16] E. Dujardin, T. Thio, H. Lezec, TW. Ebbesen, “Fabrication of mesoscopic devices from graphite microdisks”, Appl. Phys. Lett. 200, 79, 2474–6.
[17] A. Krishnan, E. Dujardin, MMJ. Treacy, J. Hugdahl, S. Lynum, TW. Ebbesen, “Graphitic cones and the nucleation of curved carbon surfaces”, Nature 1997, 388, 451–4.
[18] X. K. Lu, H. Huang, N. Nemchuk, R.S. Ruoff, “Patterning of highly oriented pyrolytic graphite by oxygen plasma etching”, Appl. Phys. Lett. 1999, 75, 193–5.
[19] Y. B. Zhang, J. P. Small, W. V. Pontius, P. Kim, “Fabrication and electric-field-dependent transport measurements of mesoscopic graphite devices,” Appl Phys Lett. 2005;86, 073104.
[20] P. Blake, E. W. Hill, A. H. C. Neto, K. S. Novoselov, D. Jiang, R. Yang, et al., “Making graphene visible”, Appl. Phys. Lett. 2007, 91, 063124.
[21] C. Soldano, A. Mahmood, E. Dujardin, “Production, properties and potential of graphene”, Carbon 2010, 48, 2127 – 2150.
[22] S. Eigler, M. E.-Heim, S. Grimm, P. Hofmann, W. Kroener, et al., “Wet Chemical Synthesis of Graphene”, Adv. Mater. 2013, 25, 3583–3587.
[23] Y. Hernandez, V. Nicolosi, M. Lotya, F. M. Blighe, Z. Sun, “High-yield production of graphene by liquid-phase exfoliation of graphite”, nature nanotech. 2008, 3, 363-368.

[24] S. Stankovich, D. A. Dikin, R. D. Piner, K. A. Kohlhaas, A. Kleinhammes, et al., “Synthesis of graphene-based nanosheets via chemical reduction of exfoliated graphite oxide”, Carbon 2007, 45, 1558–1565.
[25] D. V. Badami, “X-Ray studies of graphite formed by decomposing silicon carbide”, Carbon 1965, 3, 53-57.
[26] C. Berger, Z. M. Song, T. B. Li, X. B. Li, A. Y. Ogbazghi, R. Feng, et al., “Ultrathin epitaxial graphite: 2D electron gas properties and a route toward graphene-based nanoelectronics”, J. Phys. Chem. B 2004, 108, 19912–6.
[27] C. Berger, Z. Song, X. Li, X. Wu, N. Brown, C. Naud, et al., “Electronic confinement and coherence in patterned epitaxial graphene”, Science 2006, 312, 1191–6.
[28] W. Norimatsu, M. Kusunoki, “Growth of graphene from SiC {0001} surfaces and its mechanisms”, Semicond. Sci. Technol. 2014, 29, 064009.
[29] Y. Q. Wu, P. D. Ye, M. A. Capano, Y. Xuan, Y. Sui, M. Qi, et al. , “Top gated graphene field-effect-transistors formed by decomposition of SiC”, Appl. Phys. Lett. 2008, 92, 092102.
[30] K. S. Kim, Y. Zhao, H. Jang, S. Y. Lee, J. M. Kim, K. S. Kim, J.- H. Ahn, P. Kim, J.-Y. Choi and B. H. Hong, “Large-scale pattern growth of graphene films for stretchable transparent electrodes Nature, 2009, 457, 706.
[31] J. Coraux, A. T. N’Diaye, C. Busse and T. Michely, “Structural coherency of graphene on Ir(111)“, Nano Lett., 2008, 8, 565.
[32] X. Li, W. Cai, J. An, S. Kim, J. Nah, D. Yang, R. Piner, A. Velamakanni, I. Jung, E. Tutuc, S. K. Banerjee, L. Colombo and R. S. Ruoff, “Large-area synthesis of high-quality and uniform graphene films on copper foils”, Science, 2009, 324, 1312.
[33] S.-Y. Kwon, C. V. Ciobanu, V. Petrova, V. B. Shenoy, J. Bare~no, V. Gambin, I. Petrov and S. Kodambaka, “Growth of semiconducting graphene on palladium”, Nano Lett., 2009, 9, 3985.
[34] P. W. Sutter, J.-I. Flege and E. A. Sutter, “Epitaxial graphene on ruthenium”, Nat. Mater., 2008, 7, 406.
[35] Y. Hao, M. S. Bharathi, L. Wang, Y. Liu, H. Chen, et al., “The role of surface oxygen in the growth of large single-crystal graphene on copper”, Science 2013, 342, 720-723.
[36] W. Zhu, T. Low, V. Perebeinos, A. A. Bol, Y. Zhu, H. Yan, et al., “Structure and electronic transport in graphene wrinkles”, Nano Lett. 2012, 12, 3431−3436.
[37] F. de Juan, A. Cortijo, M. A. H. Vozmediano, “Charge inhomogeneities due to smooth ripples in graphene sheets,” Phy. Review B 2007, 76, 165409.
[38] E.-A. Kim and A. H. C. Neto, “Graphene as an electronic membrane,” EPL 2008, 84, 57007.
[39] T. O. Wehling, H. P. Dahal, A. I. Lichtenstein, A. V. Balatsky, “Local impurity effects in superconducting graphene”, Physical review B 2008, 78, 035414.
[40] A. Toyoda, T. Ando, “Theory of Electron Scattering by lattice defects in monolayer graphene”, J. Phys. Soc. Jpn. 2010,79, 094708.
[41] V. M. Pereira, F. Guinea, J. M. B. Lopes dos Santos, N. M. R. Peres, A. H. C. Neto, “Disorder induced localized states in graphene”, PRL 2006, 96, 036801.
[42] J. Ren, H. Guo, J. Pan, Y. Y. Zhang, X. Wu, et al., “Kondo effect of cobalt adatoms on a graphene monolayer controlled by substrate-induced ripples,” | Nano Lett. 2014, 14, 4011−4015.
[43] B. Uchoa, C.-Y. Lin, and A. H. C. Neto, “Tailoring graphene with metals on top”, Phys. Rev. B 2008, 77, 035420.
[44] M. Calandra, F. Mauri, “Electronic structure of heavily-doped graphene: the role of foreign atom states”, Phys. Rev. B 2007, 76, 199901.
[45] M. Hentschel, F. Guinea, “Orthogonality catastrophe and Kondo effect in graphene”, Phys. Rev. B 2007,76, 115407.
[46] K.Sengupta, G. Baskaran, “Tuning Kondo physics in Graphene with gate voltage”, Phys. Rev. B 2008, 77, 045417.
[47] F. schwierz, “Graphene transistors,” nature nanotechnology 2010, 5, 487- 496.

[48] E. V. Castro, K. S. Novoselov, S. V. Morozov, N. M. R. Peres, J. M. B. Lopes dos Santos, et al., “Biased bilayer graphene: semiconductor with a gap tunable by electric field effect”, Phys. Rev. Lett. 2007, 99, 216802.
[49] Y. Zhang, T.-T. Tang, C. Girit, Z. Hao, M.l C. Martin, et al., “Direct observation of a widely tunable bandgap in bilayer graphene”, Nature2009, 459, 820-823.
[50] M. Y. Han, B. O zyilmaz, Y. Zhang, P. Kim, “Energy band-gap engineering of graphene nanoribbons”, PRL 2007, 98, 206805.
[51] M. Bokdam, T. Amlaki, G. Brocks, P. J. Kelly, “Band gaps in incommensurable graphene on hexagonal boron nitride”, Phys. Rev. B 2014, 89, 201404.
[52] R. Balog, B. Jørgensen, L. Nilsson, M. Andersen, E. Rienks, et al., “Bandgap opening in graphene induced by patterned hydrogen adsorption”, Nature Materials 2010, 9, 315-319.
[53] J.-C. Ren, R.-Q. Zhang, Z. Ding, M. A. V. Hove, “Symmetry-dependent band gap opening in graphene induced by g-C3N4 substrates”, RSC Adv., 2014, 4, 64577–64582.
[54] G. Giovannetti, P. A. Khomyakov, G. Brocks, P. J. Kelly, J. van den Brink, “Substrate-induced band gap in graphene on hexagonal boron nitride: Ab initio density functional calculations”, Physical review B 2007, 76, 073103.
[55] S. Y. Zhou, T. Ohta, A. Bostwick, E. H. Hwang, M. Polini, et al., “Origin of the energy bandgap in epitaxial graphene,” Nature Mater. 2008, 7, 259–260.
[56] S.Y. Zhou, D.A. Siegel, A.V. Fedorov, F.El Gabaly, A.K. Schmid et al., “Origin of the energy bandgap in epitaxial graphene,” Nature Mater 2008, 7, 258–259.
[57] L. Yang, C.-H.n Park, Y.-W. Son, M. L. Cohen, S. G. Louie, “Quasiparticle energies and band gaps in graphene nanoribbons”, PRL 2007, 99, 186801.
[58] X. Li, X. Wang, L. Zhang, S. Lee, H. Dai, “Chemically derived, ultrasmooth graphene nanoribbon semiconductors”, SCIENCE 2008, 319, 1229-1232.
[59] Y. Zhang, T.-T. Tang, C. Girit, Z. Hao, M. C. Martin, et al., “Direct observation of a widely tunable bandgap in bilayer graphene”, Nature 2009, 459, 820-823.
[60] K.I. Bolotin, K.J. Sikes, Z. Jiang, M. Klima, G. Fudenberg, et al., “Ultrahigh electron mobility in suspended graphene” Solid State Communications 2008, 146, 351–355.
[61] X. Du, I. Skachko, A. Barker, E. Y. Andrei, “Approaching ballistic transport in suspended graphene”, nature nanotechnology 2008, 3 , 491-495.
[62] W. Norimatsu, M. Kusunoki, “Growth of graphene from SiC{0001} surfaces and its mechanisms”, Semicond. Sci. Technol. 2014, 29, 064009.
[63] V. E. Dorgan, A. Behnam, H. J. Conley, K. I. Bolotin, E.Pop, “High-field electrical and thermal transport in suspended graphene”, Nano Lett. 2013, 13, 4581−4586.
[64] R. S. Shishir, D. K. Ferry, “Velocity saturation in intrinsic graphene”, J. Phys. Condens. Matter 2009, 21, 344201.
[65] C. J. Docherty, M. B. Johnston, “Terahertz properties of graphene”, J Infrared Milli Terahz Waves 2012, 33, 797–815.
[66] J. Ma1, G. Xie, P. Lv, W. Gao, P. Yuan, et al., “Wavelength-Versatile Graphene-Gold Film Saturable Absorber Mirror for Ultra-Broadband Mode-Locking of Bulk Lasers”, Scientific reports 2014, 4, 5016.
[67] F. Xia, T. Mueller, Y.-M. Lin, A. V.-Garcia, P. Avouris, “Ultrafast graphene photodetector”, Nature nanotechnology 2009, 4, 839-843.
[68] X. An, F. Liu, Y. Joon Jung, S. Kar, “Tunable Graphene−Silicon Heterojunctions for Ultrasensitive Photodetection,” Nano Lett. 2013, 13, 909−916.
[69] Y. Zhang, T. Liu, B. Meng, X. Li, G. Liang, et al., “Broadband high photoresponse from pure monolayer graphene photodetector”, Nature Communications 2013, 4, 1811.
[70] G. Konstantatos, M. Badioli, L. Gaudreau, J. Osmond, M. Bernechea, et al., “Hybrid graphene–quantum dot phototransistors with ultrahigh gain” Nature nanotechnology 2012, 7, 363-368.
[71] H. Chang, Z. Sun, Q. Yuan, F. Ding, X. Tao, et al., “Thin film field-effect phototransistors from bandgap- tunable, solution-processed, few-layer reduced graphene oxide films”, Adv. Mater. 2010, 22, 4872–4876.

[72] J. Zhao, C. He, R. Yang, Z. Shi, M. Cheng, et al.," Ultra-sensitive strain sensors based on piezoresistive nanographene films", Appl. Phys. Lett. 2012, 101, 063112.
[73] Z. Chen, W. Ren, L. Gao, B. Liu, S. Pei, H.-M. Cheng, "Three-dimensional flexible and conductive interconnected graphene networks grown by chemical vapour deposition", Nature materials 2011, 10, 424-428.
[74] S-H. Bae, Y. Lee, B. K. Sharma, H.-J. Lee, J.-H. Kim, et al., "Graphene-based transparent strain sensor", Carbon 2013, 51, 236–242.
[75] Y. Wang, L. Wang, T. Yang, X. Li, X. Zang, et al., "Wearable and highly sensitive graphene strain sensors for human motion monitoring", Adv. Funct. Mater. 2014, 24, 4666–4670.
[76] T. Q. Trung, N. T. Tien, D. Kim, J. H. Jung, O. J. Yoon, et al., "High thermal responsiveness of a reduced graphene oxide field-effect transistor", Adv. Mater. 2012, 24, 5254–5260.
[77] F. Yavari, Z. Chen, A. V. Thomas, W. Ren, H.-M. Cheng, et al., "High sensitivity gas detection using a macroscopic three-dimensional graphene foam network", Scientific reports, 1, 166.
[78] Y.-H. Zhang,Y.-B. Chen, K.-G. Zhou, C.-H. Liu, J. Zeng, et al., "Improving gas sensing properties of graphene by introducing dopants and defects: a first-principles study", Nanotechnology 2009, 20, 185504.
[79] F. Schedin, A. K. Geim, S. V. Morozov, E. W. Hill, P. Blake, M. I. Katsnelson, et al., "Detection of individual gas molecules adsorbed on graphene", nature materials 2007, 6, 652-655.
[80] W. Yuan, G. Shi, "Graphene-based gas sensors", J. Mater. Chem. A, 2013, 1, 10078–10091.
[81] B. Zhan , C. Li , J. Yang , G. Jenkins , W. Huang, et al., "Graphene field-effect transistor and its application for electronic sensing", small 2014, 10, 4042–4065.
[82] Y. Wen , F.Y. Li , X. Dong , J. Zhang , Q. Xiong, et al., "The electrical detection of lead ions using gold-nanoparticle- and dnazyme-functionalized graphene device," Adv. Healthcare Mater. 2013, 2, 271–274.
[83] M. Gong , T. Zhou , D. D. Song , L. Z. Zhang ," Monodispersed Au nanoparticles decorated graphene as an enhanced sensing platform for ultrasensitive stripping voltammetric detection of mercury(II)," Sens. Actuators B 2010 , 150 , 491 .
[84] S. R. Guo, J. Lin, M. Penchev, E. Yengel, M. Ghazinejad, et al., "Label free DNA detection using large area graphene based field effect transistor biosensors", J Nanosci Nanotechnol. 2011, 11, 5258-63.
[85] B. Cai, S. Wang, L. Huang, Y. Ning, Z. Zhang, et al., "Ultrasensitive label-free detection of pna–dna hybridization by reduced graphene oxide field-effect transistor biosensor", ACS Nano, 2014, 8, 2632–2638.
[86] Y. Ohno, K. Maehashi, K. Matsumoto, "Label-free biosensors based on aptamer-modified graphene field-effect transistors", J. Am. Chem. Soc. 2010 , 132 , 18012.
[87] K. Mao, D. Wu, Y. Li, H. Ma, Z. Ni, et al., "Label-free electrochemical immunosensor based on graphene/methylene blue nanocomposite", Anal Biochem. 2012 , 1, 422-427.
[88] Y. H. Kwak, D. S. Choi, Y. N. Kim, H. Kim, D. H. Yoon, "Flexible glucose sensor using CVD-grown graphene-based field effect transistor", Biosens Bioelectron. 2012, 37, 82-87.
[89] J. Park, S. Park, S. Ryu, S. H. Bhang, J. Kim, et al., "Graphene–regulated cardiomyogenic differentiation process of mesenchymal stem cells by enhancing the expression of extracellular matrix proteins and cell signaling molecules", Advanced healthcare materials 2014, 3, 176–181.
[90] G.-Y. Chen, D.W.-P. Pang, S.-M. Hwang, H.-Y. Tuan, Y.-C. Hu, "A graphene-based platform for induced pluripotent stem cells culture and differentiation", Biomaterials 2012, 33, 418–427.
[91] N. Li, Q. Zhang, S. Gao, Q. Song, R. Huang, et al., Three-dimensional graphene foam as a biocompatible and conductive scaffold for neural stem cells", Scientific reports, 3, 1604.
[92] P.J. Marc, C.E. Sims, M. Bachman, G.P. Li, N.L. Allbritton," Fast-lysis cell traps for chemical cytometry", 2008, Lab Chip 8, 710-716.
[93] D.K. Wood, D.M. Weingeist, S.N. Bhatia, B.P. Engelward,"Single cell trapping and DNA damage analysis using microwell arrays", P. Natl. Acad. Sci. U.S.A. 2010. 107, 10008-10013.
[94] N. Bao, C. Lu, "A microfluidic device for physical trapping and electrical lysis of bacterial cells ",Appl. Phys. 2008, Lett. 92, 214103-1-3.
[95] A. Winkleman, K.L. Gudiksen, D. Ryan, G.M. Whitesides, D. Greenfield, M. Prentiss, "A magnetic trap for living cells suspended in a paramagnetic Buffer", Appl. Phys. Lett. 2004, 85, 2411-2413.

[96] A. Ashkin, J.M. Dziedzic, T. Yamane," Optical trapping and manipulation of single cells using infrared laser beams", Nature 1987, 330, 769-771.
[97] C.H. Chuang, Y.W. Huang, Y.T. Wu, "Dielectrophoretic chip with multilayer electrodes and micro-cavity array for trapping and programmably releasing single cells", Biomed. Microdevices 2012, 14, 271-278.
[98] S.K. Ameri, P.K. Singh, M.R. Dokmeci, A. Khademhosseini, Q. Xu, S.R. Sonkusale, "All electronic approach for high-throughput cell trapping and lysis with electrical impedance monitoring", Biosens.Bioelectron. 2014,54,462–467.
[99] M. Bocchi, M. Lombardini, A. Faenza, L. Rambelli, L. Giulianelli, N. Pecorari , R. Guerrieri, "Dielectrophoretic trapping in microwells for manipulation of single cells and small aggregates of particles",Biosens. Bioelectron 2009, 24, 1177-1183.
[100] C.H. Chiou, L.J. Chien, T.C. Chou, J.L. Lin, J.T. Tseng, "Rapid whole-cell sensing chip for low-level arsenite detection", Biosens. Bioelectron. 2011, 26, 2484-2488.
[101] K. Khoshmanesh, N.Kiss, S. Nahavandi, C.W. Evans, J.M. Cooper, D.E. Williams, D. Wlodkowic, "Trapping and imaging of micron-sized embryos using dielectrophoresis", 2011. Electrophoresis 32, 3129-3132.
[102] C.P. Jen, J.H. Hsiao, N.A. Maslov, "Single-Cell Chemical Lysis on Microfluidic Chips with Arrays of Microwells", Sensors-Basel 2012, 12, 347-358.
[103] S. K. Baek, J. Min, J.H. Park, "Wireless induction heating in a microfluidic device for cell lysis", Lab Chip 2010, 10, 909-917.
[104] D. Di Carlo, K.H. Jeong, L.P. Lee ," Reagentless mechanical cell lysis by nanoscale barbs in microchannels for sample preparation", Lab Chip 2003,3, 287-291.
[105] S.S. Donato, V.Chu, D.M.F. Prazeres, J.P. Conde, "Metabolic viability of Escherichia coli trapped by dielectrophoresis in microfluidics", Electrophoresis 2013, 34, 575-582.
[106] J. Gao, R. Riahi, M.L.Y. Sin, S.F. Zhang, P.K. Wong," Electrokinetic focusing and separation of mammalian cells in conductive biological fluids ", Analyst 2012, 137, 5215-5221.
[107] S.H. Kim, T. Yamamoto, D. Fourmy, T. Fujii, "Electroactive Microwell Arrays for Highly Efficient Single-Cell Trapping and Analysis", Small 2011, 7, 3239-3247.
[108] N.R. Armstrong, A.W.C. Lin, M. Fujihira, T. Kuwana, "Electrochemical and surface characteristics of tin oxide and indium oxide electrodes" Anal. Chem. 1976, 48, 741-750.
[109] E. Matveeva, "Electrochemistry of the Indium-Tin Oxide Electrode in 1 M NaOH Electrolyte", J. Electrochem. 2005, Soc. 152, H138-H145.
[110] V. Lvovich, S. Srikanthan, R.L. Silverstein, "A novel broadband impedance method for detection of cell-derived microparticles", Biosens. Bioelectron. 2010, 26, 444-451.
[111] D.A.C. Brownson, C.E. Banks, "Graphene electrochemistry: an overview of potential applications ", Analyst 2010, 135, 2768-2778.
[112] H. Hwang, Y. J. Choi, W. Choi, S. H. Kim, J. Jang, J. K. Park , "Interactive manipulation of blood cells using a lens-integrated liquid crystal display based optoelectronic tweezers system", Electrophoresis 2008, 29,1203–1212.
[113] W.C. Lee, C.H.Y.X. Lim, H. Shi, L.A.L. Tang, Y. Wang, C.T. Lim, K.P. Loh, "Origin of enhanced stem cell growth and differentiation on graphene and graphene oxide", ACS Nano 2011, 5, 7334-7341.
[114] G. Yoon, "Dielectric Properties of Body Fluids with Various Hematocrit Levels," World Academy of Science Engineering and Technology, 2011, 60, 640-643
[115] C. C. Kwong, N. Li and C.-M. Ho, Pro. of SPIE, 2005, 6003. 60030N-1.
[116] O. K. Baskurt, M. Uyuklu and H. J. Meiselman, "Time Course of Electrical Impedance During Red Blood Cell Aggregation in a Glass Tube: Comparison With Light Transmittance," IEEE Trans. Bio-Med. Eng., 2010, 57, 969-978.
[117] J. H. Hoffman, J. H. Kaplan, T. J. Callahan and J. C. Freedman, Annals of the New York Academy of Sciences, 1980, 341, 357-360.
[118] P. Mirtaheri, S. Grimnes and O. G. Martinsen, IEEE Trans. Bio-Med. Eng., 2005, 52, 2093-2099.
[119] J. D. Robertson, J. Cell Biol.,1981, 91, 189-204.

[120] J. Gimsa, Th. Schnelle, G. Zechel, and R. Glaser, Biophys. J., 1994, 66 , 1244-1253.
[121] Jason E. Gordon, Zachary Gagnon, and Hsueh-Chia Chang, Biomicrofluidics, 2007, 1, 044102.
[122] D. Padmaraj, J. H. Miller, J. Wosik and W. Zagozdzon-Wosik, Biosens. Bioelectron., 2011, 29, 13-17.
[123] P. K. Ang, W. Chen, A. T. S. Wee, K. P. Loh, "Solution-gated epitaxial graphene as ph sensor," J. AM. CHEM. SOC. 2008, 130, 14392–14393
[124] Agre, P., Parcker, 1989. Red Blood Cell Membranes: Structure: Function: Clinical Implications, Marcel Dekker,INC. , Newyork.
[125] S.H. Kim, X.M. He, S. Kaneda, J. Kawada, D. Fourmy, H. Noji, T. Fujii, "Quantifying genetically inserted fluorescent protein in single iPS cells to monitor Nanog expression using electroactive microchamber arrays "Lab Chip 2014, 14, 730-736.
[126] A. K.Geim, "Graphene: status and prospects," Science, 2009, 324,1530-4.
[127] S. Gorantla, A. Bachmatiuk, J. Hwang, H. A. Alsalman, J. Y. Kwak, T. Seyller et al., "A universal transfer route for graphene," Nanoscale, 2014, 6, 889-896.
[128] A. C. Ferrari, J. C. Mayer, V. Scardaci, C. Casiraghi, M. Lazzeri, F. Mauri, et al., "Raman spectrum of graphene and graphene layers," Phys. Rev. Lett., 2006, 97, 187401.
[129] S. Bae, H. Kim, Y. Lee, X. Xu, J. S. Park, Y. Zheng, "Roll-to-roll production of 30-inch graphene films for transparent electrodes," Nature Nanotechnology 2010, 5, 574-578.
[130] Y.M. Lin, A. Valdes-Garcia, S. J. Han, D. B. Farmer, I. Meric, Y. N. Sun, et al., "Wafer-scale graphene integrated circuit," Science 2011, 332, 1294-7.
[131] H. Wang, A. Hsu, J. Wu, J. Kong, T. Palacios, "Graphene-based ambipolar rf mixers," IEEE Electron Device Letters. 2010, 31, 906-8.
[132] H. Wang, D. Nezich, J. Kong, T. Palacios Graphene frequency multipliers, "IEEE Electron Device Letters. 2009, 30, 547-9.
[133] Y. M. Lin, C. Dimitrakopoulos, K. A. Jenkins, D. B. Farmer, H. Y. Chiu, A. Grill, et al., "100-GHz transistors from wafer-scale epitaxial graphene," Science 2010, 327, 662.
[134] R. Cheng, J. W. Bai, L. Liao, H. L. Zhou, Y. Chen, L. X. Liu, et al., "High-frequency self-aligned graphene transistors with transferred gate stacks," Proceedings of the National Academy of Sciences of the United States of America. 2012,109, 11588-92.
[135] Y. M. Lin, K. A. Jenkins, A. Valdes-Garcia, J. P. Small, D. B. Farmer, P. Avouris, "Operation of graphene transistors at gigahertz frequencies," Nano Lett. 2009, 9, 422-6.
[136] S. K. Ameri, P. K. Singh, S. R. Sonkusale, "Utilization of graphene electrode in transparent microwell arrays for high throughput cell trapping and lysis," Bio Sens. Bio Electron. 2014, 61, 625-630.
[137] L. H. Hess, M. Seifert, and J. A. Garrido, "Graphene transistors for bioelectronics," Proc. of the IEEE 2013, 101, 1780-1792.
[138] N. Singh, A. Agarwal, L. K. Bera, T. Y. Liow, R. Yang, S. C. Rustagi, et al., "High-performance fully depleted silicon-nanowire (diameter <= 5 nm) gate-all-around CMOS devices," IEEE Electron Device Letters. 2006, 27, 383-6.
[139] X. J. Duan, T. M. Fu, J. Liu, C. M. Lieber, "Nanoelectronics-biology frontier: From nanoscopic probes for action potential recording in live cells to three-dimensional cyborg tissues," Nano Today 2013, 8, 351-73.
[140] B. Z. Tian, T. Cohen-Karni, Q. Qing, X. J. Duan, P. Xie, C. M. Lieber, "Three-dimensional, flexible nanoscale field-effect transistors as localized bioprobes," Science 2010, 329, 830-4.
[141] M. J. Earle, J. M. S. S. Esperança, M. A. Gilea, J. N. C. Lopes, L. P. N. Rebelo, J. W. Magee et al., "The distillation and volatility of ionic liquids," Nature 2006,439, 831-834.
[142] T. Fujimoto, K. Awaga, "Electric-double-layer field-effect transistors with ionic liquids," Physical Chemistry Chemical Physics 2013, 15, 8983-9006.
[143] F. Chen, Q. Qing, J. L. Xia, J. H. Li, N. J. Tao, "Electrochemical gate-controlled charge transport in graphene in ionic liquid and aqueous solution," Journal of the American Chemical Society 2009, 131, 9908.
[144] H. Yuan, H. Shimotani, A. Tsukazaki, A. Ohtomo, M. Kawasaki, Y. Iwasa, "High-density carrier accumulation in zno field-effect transistors gated by electric double layers of ionic liquids," Adv. Funct. Mater. 2009, 19, 1046–1053.

[145] S. Islam, Z. Y. Li, V. E. Dorgan, M. H. Bae, E. Pop, "Role of Joule Heating on Current Saturation and Transient Behavior of Graphene Transistors," IEEE Electron Device Lett. 2013, 34, 166-8.
[146] H. Wang, Y. Wu, C. Cong, J. Shang, T. Yu, "Hysteresis of electronic transport in graphene transistors," ACS Nano 2010, 4, 7221–7228.
[147] X. Xiao, T. E. Beechem, M. T. Brumbach, T. N. Lambert, D. J. Davis, J. R. Michael, "Lithographically defined three-dimensional graphene structures," ASC nano 2012, 6, 3573–3579.
[148] K. Kirchner, et al., "Electrical double layer in ionic liquids: Structural transitions from multilayer to monolayer structure at the interface" ,Electrochimica Acta, 110, 2013, 762-771.
[149] A. F. Visentin, and M. J. Panzer, "Poly(Ethylene Glycol) Diacrylate-Supported Ionogels with Consistent Capacitive Behavior and Tunable Elastic Response," ACS Applied Materials & Interfaces, 2012. 4, 2836-2839.
[150] Z. L. Xie, et al., "A transparent, flexible, ion conductive, and luminescent PMMA ionogel based on a Pt/Eu bimetallic complex and the ionic liquid [Bmim][N(Tf)2] ," Journal of Materials Chemistry, 22, 2012. 8110-8116.
[151] J. Liu, Q. Qian, Y. Zou, G. Li, Y. Jin, K. Jiang, S. Fan, Q. Li, "Enhanced performance of graphene transistor with ion-gel top gate," Carbon, 68, 2014, 480 – 486.
[152] B. J. Kim, H. Jang, S. K. Lee, B. H. Hong, J. H. Ahn, and J. H. Cho, "High-performance flexible graphene field effect transistors with ion gel gate dielectrics," Nano Lett., 10, 2010, 3464–3466.
[153] A. Sasidharan, L. S. Panchakarla, A. R. Sadanandan, A. Ashokan, P. Chandran, et al., "Hemocompatibility and Macrophage Response of Pristine and Functionalized Graphene," small 2012, 8, 1251–1263.
[154] K. Yang, S. Zhang, G. Zhang, X. Sun, S.-T. Lee, et al., "Graphene in Mice: Ultrahigh In Vivo Tumor Uptake and Efficient Photothermal Therapy", Nano Lett. 2010, 10, 3318–3323.
[155] W. Yuan, G. Shi, "Graphene-based gas sensors", J. Mater. Chem. A, 2013, 1, 10078–10091.
[156] G. Ko, H. Y. Kim, J. Ahn, Y. M. Park, K. Y. Lee, J. Kim, "Graphene-based nitrogen dioxide gas sensors", Current Applied Physics, 2010, 10, 1002–1004.
[157] C.-H. Lu, H.-H. Yang, C.-L. Zhu, X. Chen, G.-N. Chen, "A graphene platform for sensing biomolecules", Angew. Chem. Int. Ed. 2009, 48, 4785 –4787.
[158] G. S. Kulkarni, Z. Zhong," Detection beyond the debye screening length in a high-frequency nanoelectronic biosensor", Nano Lett. 2012, 12, 719−723.
[159] B. M.- Giacchetti, A. Hsu, H. Wang, V. Vinciguerra, F. Pappalardo, et al., "pH sensing properties of graphene solution-gated field-effect transistors" J. Appl. Phys., 2013,114, 084505.
[160] X. Tan, H.-J. Chuang, M.-W. Lin, Z. Zhou, M. M.-C. Cheng, "Edge effects on the ph response of graphene nanoribbon field effect transistors", J. Phys. Chem. C, 2013, 117, 27155−27160.
[161] P. K. Ang, W. Chen, A. T. S. Wee, K. P. Loh, "Solution-gated epitaxial graphene as ph sensor", J. AM. CHEM. SOC. 2008, 130, 14392–14393.
[162] W. Fu, C. Nef, O. Knopfmacher, A. Tarasov, M. Weiss, "Graphene transistors are insensitive to ph changes in solution", Nano Lett., 2011, 11, 3597–3600.
[163] C. Waymouth, "Osmolality of mammalian blood and of media for culture of mammalian cells", In vitro, 1970, 6, 109-127.
[164] G. F. Zheng, F. Patolsky, Y. Cui, W. U. Wang, C. M. Lieber, "Multiplexed electrical detection of cancer markers with nanowire sensor arrays"' Nat. Biotechnol. 2005, 23, 1294−1301.
[165] P. B. Oliva, "Lactic Acidosis", The American journal of medicine, 1970, 48, 209-225.
[166] L. Hermaxsels, J.-B. Osnes, "Blood and muscle pH after maximal exercise in man", J. Applied Physiology, 972, 32, 304-308.
[167] S. Chen, J. G. Bomer, W. G. van der Wiel, E. T. Carlen, A. van den Berg, "Top-down fabrication of sub-30 nm monocrystalline silicon nanowires using conventional microfabrication", ACS Nano, 2009, 3, 3485–3492.
[168] B. Wang, K. L. Liddell, J. Wang, B. Koger, C. D. Keating, J. Zhu, "Oxide-on-graphene field effect bio-ready sensors", Nano Research, 2014, 7, 1263–1270.

[169] S. Zafar, C. D'Emic, A. Afzali, B. Fletcher, Y Zhu, T. Ning, "Optimization of pH sensing using silicon nanowire field effect transistors with HfO_2 as the sensing surface", Nanotechnology, 2011, 22, 405501.
[170] D. Yatess, A. Vine, T. W. Healy, "Site-binding model of the electrical double layer at the oxide/ water interface", J. Chem. Soc., Faraday Trans. 1, 1974, 70, 1807-1818.
[171] S. K. Ameri, P. K. Singh, S. R. Sonkusale, "Liquid gated three dimensional graphene network transistor", 2014, 79, 572–577.
[172] R. Dulbecco, M. Vogt, "Plaque formation and isolation of pure lines with poliomyelitis viruses", JEM 1954, 99, 167-182.
[173] G. Lupina, M. Lukosius, J. Kitzmann, J. Dabrowski, A. Wolff, et al. , "Nucleation and growth of HfO_2 layers on graphene by CVD", Appl. Phys. Lett., 2013,103, 183116.
[174] D. Barreca, A. Milanov, R. A. Fischer, A. Devi, E. Tondello, "Hafnium oxide thin film grown by ALD: An XPS study", Surface Science Spectra 2007, 14, 34-40.
[175] Z. Cheng, Q. Li, Z. Li, Q. Zhou, Y. Fang, "Suspended Graphene Sensors with Improved Signal and Reduced Noise", Nano Lett. 2010, 10, 1864–1868.
[176] M. Huang, T. A. Pascal, H. Kim, W. A. Goddard , J. R. Greer, "Electronic−mechanical coupling in graphene from in situ nanoindentation experiments and multiscale atomistic simulations," Nano Lett. 2011, 11, 1241–1246.
[177] B. Han, J. Ou, "Embedded piezoresistive cement-based stress/strain sensor," Sensors and Actuators A 2007, 138, 294–298.
[178] I. Kang, M. J. Schulz, J. H. Kim, V. Shanov, D. Shi, " A carbon nanotube strain sensor for structural health monitoring," Smart Mater. Struct. 2006, 15, 737–748.
[179] P.M. Talaia, A. Ramos, I. Abe, M.W. Schiller, P. Lopes, et al, "Plated and Intact Femur Strains in Fracture Fixation Using Fiber Bragg Gratings and Strain Gauges," Experimental mechanics 2007, 47, 355–363.
[180] S. Iwaia, T. Q. P. Uyeda, "Visualizing myosin–actin interaction with a genetically-encoded fluorescent strain sensor," PNAS 2008, 105, 16882–16887.
[181] S. Takamatsu, T. Takahata, M. Muraki, E. Iwase, K. Matsumoto, et al., "Transparent conductive-polymer strain sensors for touch input sheets of flexible displays," J. Micromech. Microeng. 2010, 20, 075017.
[182] D. J. Lipomi, M. Vosgueritchian, B. C-K. Tee, Sondra L. Hellstrom, J. A. Lee, et al., "Skin-like pressure and strain sensors based on transparent elastic films of carbon nanotubes," Nature nanotechnology 2011, 6, 788-792.
[183] X. Li, R. J. Zhang, W. J. Yu, K. L. Wang, J. Q. Wei, et al., "Stretchable and highly sensitive graphene-on-polymer strain sensors," Sci. Rep. 2012, 2, 870.
[184] X. Xiao, L. Yuan, J. Zhong, T. Ding, Y. Liu, et al., "High-strain sensors based on zno nanowire/polystyrene hybridized flexible films," Adv. Mater. 2011, 23, 5440–5444.
[185] J. Ming Wu, C-Y Chen, Y. Zhang, K-H Chen, Y. Yang, et al., "Ultrahigh sensitive piezotronic strain sensors based on a $znsno_3$ nanowire/microwire," ACS nano 2012, 5, 4369-4374.
[186] T. Yamada, Y. Hayamizu, Y. Yamamoto, Y. Yomogida, A. I-Najafabadi, et al., "A stretchable carbon nanotube strain sensor for human-motion detection," Nature nanotech. 2011, 6, 296-301.
[187] D. Ponnamma, Q. Guo, I. Krupa, M. A. S. A. Al-Maadeed, K. T. Varughese , et al., "Graphene and graphitic derivative filled polymer composites as potential sensors," Phys. Chem. Chem. Phys., 2015, 17, 3954-3981.
[188] M. Amjadi, A. Pichitpajongkit, S. Lee, S. Ryu, I. Park, et al., "Highly stretchable and sensitive strain sensor based on silver nanowire/elastomer nanocomposite," ACS nano 2014, 8, 5154–5163.
[189] J. Zhao, C. He, R. Yang, Z. Shi, M. Cheng, et al., "Ultra-sensitive strain sensors based on piezoresistive nanographene films," Appl. Phys. Lett. 2012, 101, 063112.
[190] A. L. Window, Strain Gauge Technology; Elsevier Applied Science: London, UK, 1992.
[191] Y. Wang, R. Yang, Z. Shi, L. Zhang, D. Shi, et al., "Super-Elastic Graphene Ripples for Flexible Strain Sensors," ACS nano 2011, 5, 3645–3650.

[192] H. Tian, Y. Shu, Y-L Cui, W-T Mi, Y. Yang, et al., “Scalable fabrication of high-performance and flexible graphene strain sensors,” Nanoscale 2014, 6, 699–705.
[193] S. Stassi, V. Cauda, G. Canavese, C. F. Pirri, “Flexible Tactile Sensing Based on Piezoresistive Composites: A Review,” Sensors 2014, *14*, 5296-5332.
[194] W. C. Claycomb, N. A. Lanson, JR., B. S. Stallworth, D. B. Egeland, J. B. Delcarpio, “HL-1 cells: A cardiac muscle cell line that contracts and retains phenotypic characteristics of the adult cardiomyocyte”, Proc. Natl. Acad. Sci. USA 1998, 95, 2979–2984.
[195] http://apbiomaedahs.weebly.com/2b-cell-homeostasis---cell-membrane-processes.html
[196] J. Pinnell, S. Turner, S. Howell, “Cardiac muscle physiology”, Continuing Education in Anaesthesia, Critical Care & Pain 2007, 7, 85-88.
[197] R. C. Addis, J. A. Epstein, “Induced regeneration—the progress and promise of direct reprogramming for heart repair,” nature medicine 2013,19, 829-836.
[198] C-B Chien, J. Pine, “Voltage-sensitive dye recording of action potentials and synaptic potentials from sympathetic microcultures,”Biophys. J. c Biophysical Society 1991, 60, 697-711.
[199] N. Osorio, P. Delmas, “Patch clamp recording from enteric neurons in situ,” nature protocols 2011, 6, 15-27.
[200] A. O. Verkerk, M. M. van Borren, R. J. Peters, E. Broekhuis, K. Y. Lam, et al., “ Single cells isolated from human sinoatrial node: action potentials and numerical reconstruction of pacemaker current,” Conf Proc IEEE Eng Med Biol Soc. 2007, 904-7.
[201] J. Pine, “Recording action potentials from cultured neurons with extracellular microcircuit electrodes,” J Neurosci Methods. 1980, 2, 19-31.
[202] M. S. Spach, R. C. Barr, G. A. Serwer, J. Mailen Kootsey, E. A. Johnson, “Extracellular potentials related to intracellular action potentials in the dog purkinje system,” Circulation Research 1972, NO. 5, 505-519.
[203] X. Duan, R. Gao, P. Xie, T. C-Karni, Q. Qing, et al., “Intracellular recordings of action potentials by an extracellular nanoscale field-effect transistor,” Nature nanotechnology 2012, 7, 174-179.
[204] C. Xie, Z. Lin, L. Hanson, Y. Cui, B. Cui, “Intracellular recording of action potentials by nanopillar electroporation,” Nature nanotechnology 2012, 7, 185-190.
[205] M. Meister, J. Pine, D. A. Baylor, “Multi-neuronal signals from the retina: acquisition and analysis,” Journal of Neuroscience Methods 1994, 51, 95-106.
[206] F. Franke, D. Jäckel, J. Dragas, J.Müller, M. Radivojevic, et al., “High density microelectrode array recordings and real-time spike sorting for closed-loop experiments: an emerging technology to study neural plasticity,” Frontiers in neural circuits 2012, 6, 105.
[207] T. C-Karni, Q. Qing, Q. Li, Ying Fang, C. M. Lieber, et al., “Graphene and nanowire transistors for cellular interfaces and electrical recording,” Nano Lett. 2010, 10, 1098–1102.
[208] L. H. Hess, M. Jansen, V. Maybeck, M. V. Hauf, M. Seifert, “Graphene transistor arrays for recording action potentials from electrogenic cells,” Adv. Mater. 2011, 23, 5045–5049.
[209] U. A. Aregueta-Robles, A. J. Woolley , L. A. Poole-Warren, N. H. Lovell, R. A. Green, “Organic electrode coatings for next-generation neural interfaces,” Frontiers in neuroengineering 2014, 7, 1-18.
[210] W. G. Regehr, J. Pine, C. S. Cohan, M. D. Mischke , D. W. Tank, “Sealing cultured invertebrate neurons to embedded dish electrodes facilitates long-term stimulation and recording”, Journal of Neurosctence methods 1989, 30, 91-106 91.
[211] M. E. Spira and A.Hai, “Multi-electrode array technologies for neuroscience and cardiology,” Nature nanotechnology 2013, 8, 83-94.
[212] D. Kuzum, H. Takano, E. Shim, J. C. Reed, H. Juul, et al., “Transparent and flexible low noise graphene electrodes for simultaneous electrophysiology and neuroimaging”, Nature communications 2014, 5, 5259.
[213] T. Kim, Y. H. Kahng, T. Lee, K. Lee, and D. H. Kim, “Graphene films show stable cell attachment and biocompatibility with electrogenic primary cardiac cells,” Mol. Cells 2013, 36, 577-582.
[214] S. K. Lee, H. Kim, and B. S. Shim, “Graphene: an emerging material for biological tissue engineering,” Carbon Letters 2013, 14, 63-75 .

[215] L. A. Greene, A. S. Tischler, “Establishment of a noradrenergic clonal line of rat adrenal pheochromocytoma cells which respond to nerve growth factor,” Proc. Natl. Acad. Sci. USA 1976, 73, 2424-2428.
[216] J. B. Davi, P. Stroobant, “Platelet-derived growth factors and fibroblast growth factors are mitogens for rat schwalm cells,” The Journal of Cell Biology 1990, I0, 1353-1360.
[217] W. M. Campana, “Schwann cells: Activated peripheral glia and their role in neuropathic pain,” Brain, Behavior and Immunity 2007, 21, 522–527.
[218] M. D. Baker, “Electrophysiology of mammalian Schwann cells,” Progress in Biophysics & Molecular Biology 2002, 78, 83–103.
[219] L. Meng, A. Jiang, R. Chen, C.-z. Li, L. Wang, et al., “Inhibitory effects of multiwall carbon nanotubes with high iron impurity on viability and neuronal differentiation in cultured PC12 cells”, Toxicology 2013, 313, 49– 58.
[220] T. Ren, S. Yu, Z. Mao, C. Gao, “A complementary density gradient of zwitterionic polymer brushes and NCAM peptides for selectively controlling directional migration of Schwann cells”, Biomaterials 2015, 56, 58-67.
[221] S. Choi, Y. Hong, I. Lee, D. Huch, T.-J. Jeon, S. M. Kim, “Effect of various extracellular matrix proteins on the growth of HL-1 cardiomyocytes”, Cells tissue organs, 2013, 198, 349-356.
[222] E. Y. Andrei, G. Li, X. Du, “Electronic properties of graphene: a perspective from scanning tunneling microscopy and magnetotransport,” Rep. Prog. Phys. 2012, 75, 056501.
[223] http://www.analog.com/media/en/technical-documentation/data-sheets/OP177.pdf.